CAVITATION INDUCED INSTABILITIES ASSOCIATED WITH TURBOMACHINES

Thesis by

David Miner Braisted

In Partial Fulfillment of the Requirements
For the Degree of
Doctor of Philosophy

California Institute of Technology
Pasadena, California
1980

(Submitted August 29, 1979)

ACKNOWLEDGMENTS

I would like to express my deepest appreciation to my advisor, Dr. C. Brennen, for making my thesis research a truly rewarding experience. His assistance, guidance and encouragement were indispensable.

I also wish to thank Dr. A. J. Acosta for his valuable advice and assistance.

The technical assistance provided by E. Daly, J. Fontana, L. Johnson, N. Keidel and G. Lundgren is gratefully acknowledged.

Special thanks go to J. Del Valle, G. Hendrickson, P. Engelauf, S. Cheung, E. Lo, D. Rovner and G. Hoffman for their help in the various phases of the experimental investigations.

I also wish to thank R. Dudek for her efforts in preparing this manuscript. Thanks also to C. Lin for preparing the figures. In addition, I also wish to express my thanks to B. Hawk and S. Berkley who helped with the administrative details and in other ways made my stay here a little easier.

I am very grateful for the NSF Graduate Fellowship, Guggenheim Fellowship, ARCS Scholarship and Research Assistantship awarded by the Institute which made this work possible. The National Aeronautics and Space Administration is also acknowledged for its financial support and backing of this investigation.

Finally, I wish to express my deepest and most sincere thanks to my wife, Nina, for her unceasing patience, understanding and constant encouragement.

ABSTRACT

Cavitation induced instabilities of hydraulic systems were investigated both experimentally and analytically. The instability, known as auto-oscillation, was found to occur in a well defined region of cavitation numbers just above head breakdown of the inducer. Auto-oscillation is characterized by large amplitude fluctuations in the pressures and mass flow rates throughout the system. The frequency of the oscillations was observed to decrease with a reduction in both the flow coefficient and cavitation number. The amplitudes of the fluctuation increased with a reduction in the flow coefficient. These detailed measurements reflect changes in the dynamic performance of the inducer due to cavitation and the interaction between the dynamics of the inducer and those of the inlet flow field. Some detailed analytical studies were performed to try to understand the nature of this interaction.

A linear stability analysis was developed which was based upon the understanding that auto-oscillation is a function of the entire hydraulic system including the cavitating inducer. Using the experimentally obtained transfer functions of two impellers, the analysis successfully predicted both the onset and frequency of auto-oscillation. The stability of the Dynamic Pump Test Facility is significantly reduced by the increased dynamically active character of the inducers at the lower cavitation number. In addition, the stability of the Dynamic Pump Test Facility was found to be particularly sensitive to the mass flow gain factor and pump impedance.

TABLE OF CONTENTS

LIST OF FIGURES

LIST OF SYMBOLS

$\tilde{a}$	acceleration amplitude
a	element of network theory transfer function
b	element of network theory transfer function
c	element of network theory transfer function
d	element of network theory transfer function
e	voltage
f	function of radial coordinate
g	gravitational acceleration
h	total head
i	current
j	$\sqrt{-1}$
k	exponent in mean axial velocity profile
l	height of water column
ℓ_c	length of pressure tranducer connections
m	mass flow rate
n	exponent in mean swirl velocity profile
p	pressure
p_{ATM}	atmospheric pressure
p_v	vapor pressure
q	series coefficients in transfer function fit
r	radial coordinate
s	sonic velocity
t	time
u	radial velocity
u_r	velocity relative to transducer connections
v	azimuthal or swirl velocity

v_r fluid velocity relative to tube

w axial velocity

x input vector

y output vector

z axial coordinate

A area

A_c cross-sectional area of pressure transducer connections

A_I inlet area of inducer

A_T cross-sectional area of water column

C compliance

C_D compliance of downstream smoothing section

E energy flux

G function of the flow angle, γ (r)

H mean total head

I impedance

K strength of axial velocity non-uniformity

L length

M mean mass flow rate

N intensity of swirl velocity

N_{CR} critical value of swirl intensity

P mean pressure

Q volumetric flow rate

R radius of pipe

S system transfer function

U mean radial velocity

U_T inducer tip speed

V mean swirl velocity

$|V|$ magnitude of velocity vector

W mean axial velocity

X reduced transfer function

Y transfer function

Z $= Y - \mathcal{J}$

ZP pump transfer function

$\mathcal{A}$ $= \bar{Y}_{11} Y_{21} + Y_{11} \bar{Y}_{21}$

$\mathcal{B}$ $= \bar{Y}_{12} Y_{22} + Y_{12} \bar{Y}_{22}$

$\mathcal{C}$ $= \bar{Y}_{11} Y_{22} + Y_{12} \bar{Y}_{21}$

$\mathcal{D}$ = determinant of $[Y] = Y_{11} Y_{22} - Y_{12} Y_{21}$

$\mathcal{E}$ non-dimensional energy flux

$\Delta \mathcal{E}$ energy flux difference

$\Delta \mathcal{E}_{osc}$ net energy flux

$\mathcal{F}$ function of system transfer function, $[S]$

$\mathcal{G}$ function of system transfer function, $[S]$

$\mathcal{H}$ blade tip spacing

$\mathcal{J}$ identity matrix

$\mathcal{K}$ wave number

$\mathcal{L}$ inertance

$\mathcal{M}$ non-dimensional mean mass flow rate

$\mathcal{N}$ $= \frac{s}{W_o}$ = inverse Mach number

$\mathcal{P}$ non-dimensional mean pressure

$\mathcal{R}$ resistance

$\mathcal{R}_p$ = Real $\{ - Y_{12} \}$ = pump resistance

$\mathcal{R}_{sys}$ total steady state system resistance

S wave speed

$\mathcal{U}$ non-dimensional mean radial velocity

$\mathcal{V}$ non-dimensional mean swirl velocity

$\mathcal{W}$ non-dimensional mean axial velocity

α eigenvalue

β coefficient in power series expansion of radial velocity

γ flow angle

δ vapor layer thickness

η first zero of $J_1 = 3.832$

θ azimuthal coordinate

$\varkappa$ modified compliance

λ wave length

μ azimuthal wave number

ρ liquid density

σ cavitation number $= \dfrac{p_1 - p_v}{\frac{1}{2}\rho U_T^2}$

τ dummy variable

υ volume

φ flow coefficient $= \dfrac{\rho Q}{\rho A_I U_T}$

χ constant

ω frequency

Γ $= j\Omega + j\mu \dfrac{\mathcal{V}(r)}{r} + \alpha \mathcal{W}(r)$

$\hat{\Gamma}$ $= \alpha + j\Omega$

Θ $= \dfrac{\Omega \eta}{\eta^2 - 1}$

Λ $= \frac{1}{\sqrt{2\kappa}}$

Υ = constant

Φ phase angle of pressure fluctuations

Ψ head coefficient $= \frac{p_2 - p_1}{\rho U_T^2}$

Ω non-dimensional frequency

Subscripts

o	average value
1	inlet
2	discharge
U	upstream
D	downstream
∞	far upstream
i,j,k	dummy subscripts

Superscripts

—	complex conjugate
~	fluctuating quantity
*	dimensional quantity

I. INTRODUCTION

1.1 Background

Designers of hydraulic systems have long recognized the susceptibility of these systems to instabilities. Instabilities can occur during transient or steady state operation of the system. In either case, the amplitude of the resulting oscillations can become exceedingly large. The damage caused by an instability can be considerable. In the case of the Lac Blanc-Lac Noir pump storage system, "a great power station was completely destroyed" and several engineers were killed [32][1].

According to Stepanoff [51] the following three conditions are necessary for a hydraulic system to become unstable.

> "1) The mass of water must be free to oscillate.
> 2) There must be a member in the system which can store and give back the pressure energy or act as a spring in a water system.
> 3) There must be some member that will provide impulses at regular intervals to start the swings."[2]

Depending upon the hydraulic system, trapped gas or vapor volumes, the compressibility of the working fluid and/or the elasticity of the piping can act as the spring like member of the second criterion. The necessary excitation can be provided in many ways. Guide vane vibration, vibration of valves, and seal leakage have been known to generate an instability [1, 32]. In pumping systems, pumps or compressors can excite an instability if operated at flow rates for which their head-capacity

---

[1] Numbers in brackets designate References at end of thesis.

[2] A. J. Stepanoff [51].

characteristics have a positive slope [18,26,44,51].

1.2 Design Methods for Hydraulic Systems

Several philosophically different design methods have been developed in order to minimize the unstable behavior of hydraulic systems. One technique is to simply suppress the resulting oscillations and vibrations. Pressure oscillations have been suppressed by the inclusion of surge tanks in hydropower systems [32] and feedline accumulators in liquid propelled rockets [20,39]. Usually, increasing the stiffness of the structure reduces the vibration level of the piping. These precautions do not, however, guarantee a stable system. The accident of the Kandergrund Tunnel is a case in point. The surge tank of this tunnel was located at a pressure node of the 11^{th} harmonic of the system. Needless to say, the surge tank was ineffective in suppressing the pressure oscillations at this frequency.

Besides the passive suppression schemes described above, active suppression systems have also been designed. Farrel and Fenwick [23] have designed an electronic-hydraulic servo feedback system to control the feedline pressure to the Space Shuttle Main Engine.

The third design method is based upon avoidance of the instability rather than minimizing the effects of the instability by either of the above suppression methods. This technique requires a basic understanding of the actual or potential causes of an instability. In the past, the steady state characteristics of pumps, compressors or turbines and a quasi-static assumption were used in the stability analysis [18,26,36,49]. This information is sufficient in many cases. However, the trend towards higher speed and higher performance devices has caused a reassessment of these approximations. Recently, it has been discovered

that cavitating inducer pumps, in particular, are dynamically active. The dynamic performance of such inducers is significantly different than that obtained via the quasi-static approximation [41,42,43]. Active devices, by definition, have the capability to supply energy to fluctuations within the flow. The results of the stability analysis may indicate a particular sensitivity to the suction line resistance and inertance, for example [8,49]. A consideration of these factors during the design process will hopefully lead to enhanced stability of the system.

The choice of design technique does depend upon the design criteria and the type or mode of instability encountered. A brief digression to discuss the dynamic performance of pumps will follow in the next section.

1.3 Dynamic Performance of Pumps

The small amplitude linear dynamic behavior of a pump at constant rotational speed can be represented in terms of a transfer function [3,15,41,42,43]. The transfer function relates the non-dimensional discharge fluctuating pressure and mass flow rate to those quantities at inlet. The transfer function of a pump is then defined by

$$\begin{Bmatrix} \tilde{p}_2 \\ \tilde{m}_2 \end{Bmatrix} = \begin{bmatrix} Y_{11} & Y_{12} \\ Y_{21} & Y_{22} \end{bmatrix} \begin{Bmatrix} \tilde{p}_1 \\ \tilde{m}_1 \end{Bmatrix} \qquad (1.3.1)$$

The pressures and mass flow rates have been non-dimensionalized by $\frac{1}{2}\rho U_T^2$ and $\rho A_I U_T$, respectively. The elements of the transfer function are complex in order to represent the phase relationship between the fluctuating quantities.

The Y_{11} term represents a dynamic pressure gain. Values of this parameter differing from unity indicate that the pump is acting as a pressure amplifier. The Y_{21} element is the pump compliance term. It indicates the variation of the cavitation volume with fluctuations of the inlet pressure. The Y_{22} term, known as the mass flow gain factor, is related to the fluctuating rates of vapor production caused by fluctuations in the angle of attack. Finally, the Y_{12} term represents the pump impedance.

The problem of evaluating the dynamics of pumps is reduced to determining, in some manner, the elements of the transfer function. Except for Brennen's "Bubbly Flow Model" [12], analytical efforts to predict the Y_{ij}'s have been largely unsuccessful [14, 15, 25, 28]. This is a result of the very complex nature of the flow field and of the various types of cavitation that occur in pumps, neither of which are quantitatively well understood. An experimental program was undertaken at the California Institute of Technology to measure transfer functions of several inducer pumps at various mean flow conditions [16, 41, 42, 43]. The results of these experiments indicate that quasi-static assumptions are valid only at very low frequencies.

1.4 Classification of Hydraulic System Instabilities

The type of instability that occurs depends upon the size and dynamic characteristics of the hydraulic system and the exciting element. In systems whose dimensions are larger than the acoustic wave length, an "organ pipe" mode of resonance in the pipelines can occur. Many examples of pipeline resonances in connection with hydropower systems have been documented [1, 32]. In most instances, the resonance did

not occur in the fundamental mode but at an odd harmonic. Systems whose dimensions are smaller than the acoustic wavelength do not exhibit such behavior.

Excluding the above acoustic phenomena, the instabilities associated specifically with cavitating inducers belong to two general catagories. One possible mode of instability is connected predominantly with characteristics of the inducer and the inlet flow field. This instability, referred to as rotating cavitation, manifests itself as an unsteady cavitation pattern at inlet that rotates with respect to the inducer blades. Both Kamijyo, et al [34] and Taylor, et al [53] have indicated that the propagation of the cavities requires a circumferential non-uniformity in the inlet flow. In addition, according to Kamijyo, et al [34], the occurrence of rotating cavitation is accompanied by "large" inlet pressure fluctuations and no measurable pressure fluctuations at discharge. There is no indication that this instability involves fluctuations in the global mass flow rates at inlet or discharge.

The other type of instability is associated with the entire hydraulic system. Structural vibrations can, under the right circumstances, excite a flow instability. The POGO instability of liquid propellant rockets is an example of a coupled structural-hydraulic instability. The POGO instability is characterized by large amplitude longitudinal vibrations of the rocket mainframe [20, 39, 48]. The acceleration amplitude of these oscillations has been measured at tens of g's. The vibrations feed back into the propulsion system causing fluctuations in the oxidizer and fuel pressure and mass flow rates. These perturbations in turn result in an unsteady thrust generation which couples back into the structural vibrations.

It is not necessary, however, for the structure to actively participate in an instability. In passive or stiff systems, an active device, such as cavitating inducer, can excite an instability characterized by large amplitude fluctuations in both the inlet and discharge pressures and mass flow rates [2,6,8,21,33,34,38,40,49,56]. This self induced instability is known as auto-oscillation. The phenomenon of auto-oscillation will be more fully discussed in the next section.

1.5 Auto-Oscillation

Auto-oscillation is a function of the entire hydraulic circuit. It has been recognized [21,49,53,56] that the hydraulic system does not cause the instability; but rather, it influences the frequency and amplitude of the oscillations. The cavitating inducer (i.e. the active element of the hydraulic system) has been identified as the cause of the auto-oscillation. A list of possible mechanisms would include a hydro-elastic instability such as leading edge flutter of the inducer blades, rotating cavitation, cavitation occurring within the inducer, backflow induced prerotation of the inlet flow, dynamic pressure gain, etc. Barr [6] and Etter [21] using a momentum analysis by Yeh [55] have concluded that rotating cavitation does not excite a condition of auto-oscillation. In that analysis, no allowance was made for the cavitation that would be present in the inducer. Neither Barr nor Etter considered this a serious deficiency to their arguments. Instead, they along with other investigators [31,34,40,46] have concluded that auto-oscillation is a cavitation induced phenomenon. However, there is no universally accepted means by which cavitation induces or excites

auto-oscillation. Both Barr [6] and Etter [21] suggest that an inherent instability associated with cavity length causes auto-oscillation. Tests on cascades of hydrofoils [4,37] do indicate that for cavity length to chord ratios between ~0.5 and ~1.2 the cavitation pattern is highly unsteady and the unsteadiness is periodic. In inducers, an unsteadiness has been observed in the cavitation when either the length of the cavity approaches the chord of the inducer blades [6] or when the cavity length is such that the trailing edge of the cavity just enters the passage formed by the adjacent blade [21]. Young, et al [56] on the other hand, indicates that the mechanism is more subtle. They propose that it is the dynamic behavior or compliance of the cavitation that is the important factor. This conviction has been arrived at by Young, et al [56] mainly through stability models. The predicted stability margins are sensitive to or directly related to the compliance contributions due to the cavitation within the inducer. Alternatively, Badowski [5] has proposed that the coupling between the cavitation, the head production and the backflow induced prerotation as the ultimate cause of auto-oscillation.

With regard to the possibility of a dynamic pressure gain causing auto-oscillation, Young, et al [56], in their stability analysis, found the pressure gain to be a stabilizing feature of the pump dynamics. Finally, leading edge flutter cannot be completely ruled out in all cases. However, estimates of the flutter frequency based on the results of Barton [7] and Lindholm, et al [35] can, in some instances, be several orders of magnitude larger than the auto-oscillation frequency. Similarly, the frequency of other internal hydrodynamic disturbances is much larger than the auto-oscillation frequency.

Clearly, the actual mechanism behind auto-oscillation is not well understood. Indeed, it may be necessary for several of the above mechanisms to occur simultaneously.

1.6 Goals of this Research

The object of the current study was to investigate the phenomenon of auto-oscillation in detail. This study had a dual purpose. The first was to define and identify the characteristics of auto-oscillation. This was accomplished by means of a set of experiments in which measurements of the fluctuating pressures and mass flow rates throughout the system during auto-oscillation were made. The second goal was to predict the onset of auto-oscillation. Towards this end, a linear stability analysis incorporating a more accurate description of the pump dynamics was developed.

The experiments were performed on the Dynamic Pump Test Facility (DPTF) located at the California Institute of Technology. In addition, the dynamic characteristics of cavitating inducers used in the stability analysis were obtained on this pump loop.

II. EXPERIMENTAL FACILITY AND TECHNIQUES

2.1 Test Facility

As mentioned in the introduction, the current investigations were performed in the DPTF. This compact, closed loop system was originally designed to obtain transfer functions of several inducers. The size of the pump loop was selected so as to limit the amplitude of the pressure fluctuations.

A schematic of the original configuration of the DPTF appears in Fig. 2.1. Each component of this pump loop has been described in detail in Ref. [41]. Several modifications were made on the pump loop during the course of the present study. The working section (the pump housing and volute) was redesigned for the purpose of observing and comparing the dynamics of 10.16 cm (4 inch) diameter impellers to the original 7.62 cm (3 inch) diameter impellers. The downstream smoothing section provided a significant compliance which had to be removed from the earlier transfer functions. The diameter of the downstream smoothing section was reduced and its wall thickness increased in order to reduce its structural compliance by a factor of 2. The volume reduction also decreased the overall compliance provided by the compressibility of the water within this section. The magnitude of this correction to the transfer function was substantially reduced by this redesign. In addition, the length of both the upstream and downstream smoothing sections was reduced to allow insertion of two modified Foxboro electromagnetic flow meters. The resulting configuration of the DPTF is presented in Fig. 2.2.

For future reference, the experimentally obtained transfer functions, [Z], describe or define the dynamics of the entire portion

of the pump loop between the two laser doppler velocimeters. Corrections for the dynamics of the system external to the inducer-volute combination are then applied to obtain the transfer function of the pump, [ZP]. This procedure is described in complete detail in Ref. [41].

2.2 Instrumentation

The location of the standard transfer function instrumentation is indicated in Figs. 2.1 and 2.2. This basic instrumentation and its associated electronics is fully described in Ref. [41]. The instrument package consists of two laser doppler velocimeters, two Statham model PA822 strain gauge pressure transducers, a turbine flow meter and a magnetic pickup which sensed the pump rotational speed. Supplementing the above measurement capability, three Validyne model DP15 variable reluctance pressure transducers were mounted axially in the neighborhood of the inlet of the inducer. The location of these transducers is indicated in Fig. 2.3.

All pressure transducers were calibrated against a precise Heise pressure gauge. Prior to this study, the slope of these calibration curves was used to reduce the dynamic data. The high estimates of the natural frequency of the pressure transducers supplied by the vendors indicated the validity of this procedure. To corroborate this information, a dynamic pressure transducer calibration scheme was devised similar to that reported in Ref. [29]. This calibration scheme uses inertially generated sinusoidal pressure fluctuations. The details of the procedure are discussed in Appendix A. The amplitude and phase of the transducer outputs are presented in Figs. A.2-A.5. It is evident that the mounting connections cause a large reduction in the

natural frequency of the pressure transducers. This frequency is particularly sensitive to any source of compliance—air bubbles, cavitation, etc. Care was taken to purge each of the transducers of any trapped air bubbles before every experiment. The appropriate corrections in both amplitude and phase were made during reduction of the data. Corrections associated with the amplifiers and filters were also applied.

Furthermore, electronic calibrations were applied to the upstream and downstream velocity measurements. As mentioned in Ref. [41], the laser doppler velocimeters possess certain inherent limitations. The magnitude of the velocity transient or fluctuations that could be accurately measured was limited by the ability of the phase locked loop located within the processing electronics to track or follow large amplitude velocity excursions. This limitation did not appreciably affect the quality of the data obtained in this study. Secondly, the laser beams could be entirely scattered by free stream nucleii, either particles or bubbles, within the flow preventing any velocity measurement. Particle scattering has never presented any problem in this regard. The scattering of the laser beams by the traveling or gaseous cavitation bubbles was minimized by deaerating the water. The dissolved air content of the water was approximately 3–6 ppm for each test. Deaeration effectively eliminated the scattering problem.

2.3 Impellers

Experiments were performed with five different inducers during the course of this investigation. The initial preliminary

observations on auto-oscillation were made on IMP4 and IMP5. IMP4 is a 7.62 cm (3.0 inch) diameter, $\frac{1}{4}$ scale model of the Low Pressure Oxidizer Turbopump (LPOTP) of the Space Shuttle Main Engine (SSME). A schematic of this impeller appears in figure 2.4. IMP5, which is also shown in that figure, is a 7.62 cm (3.0 inch) diameter, three bladed helical inducer. The blade angle at the tip was 9^{o}. After the initial cursory observations were completed, the DPTF was modified to accommodate the 10.26 cm(4.0 inch) diameter inducers IMP6, IMP7 and IMP8. IMP6 and IMP7 are both just scaled up versions of IMP4 and IMP5, respectively. IMP8, however, is a four bladed helical inducer with a blade angle at the tip of $7\frac{1}{2}^{o}$. Both IMP7 and IMP8 had a solidity of 2.0. IMP4 and IMP6 were operated with a stator blade row behind the impeller; the other inducers were not followed by a stator.

2.4 Experimental Techniques

The experiment from which the auto-oscillation data were obtained was based upon the traditional steady state cavitation performance test. First, a mean flow rate or flow coefficient was selected. Then, the cavitation number was reduced from an initially high value while maintaining the chosen flow coefficient. The steady flow data was extracted from the transducer outputs by means of an integrating voltmeter. If auto-oscillation occurred, the transducer outputs were recorded on a 14 channel Ampex FM instrumentation tape recorder; while the D. C. or mean values were simultaneously obtained via the integrating voltmeter. Data were also recorded for operating states just outside the auto-oscillation region. After the recording, the

cavitation number was altered by a small amount and the above procedure repeated.

A Spectral Dynamics Model SD360 Signal Analyzer was used to obtain the amplitude and phase relationships of the recorded data. The Signal Analyzer used a Fast Fourier Transform to calculate the spectra of the input wave forms. The phase of each transducer output relative to the downstream pressure fluctuations was determined by cross-correlation of the two wave forms.

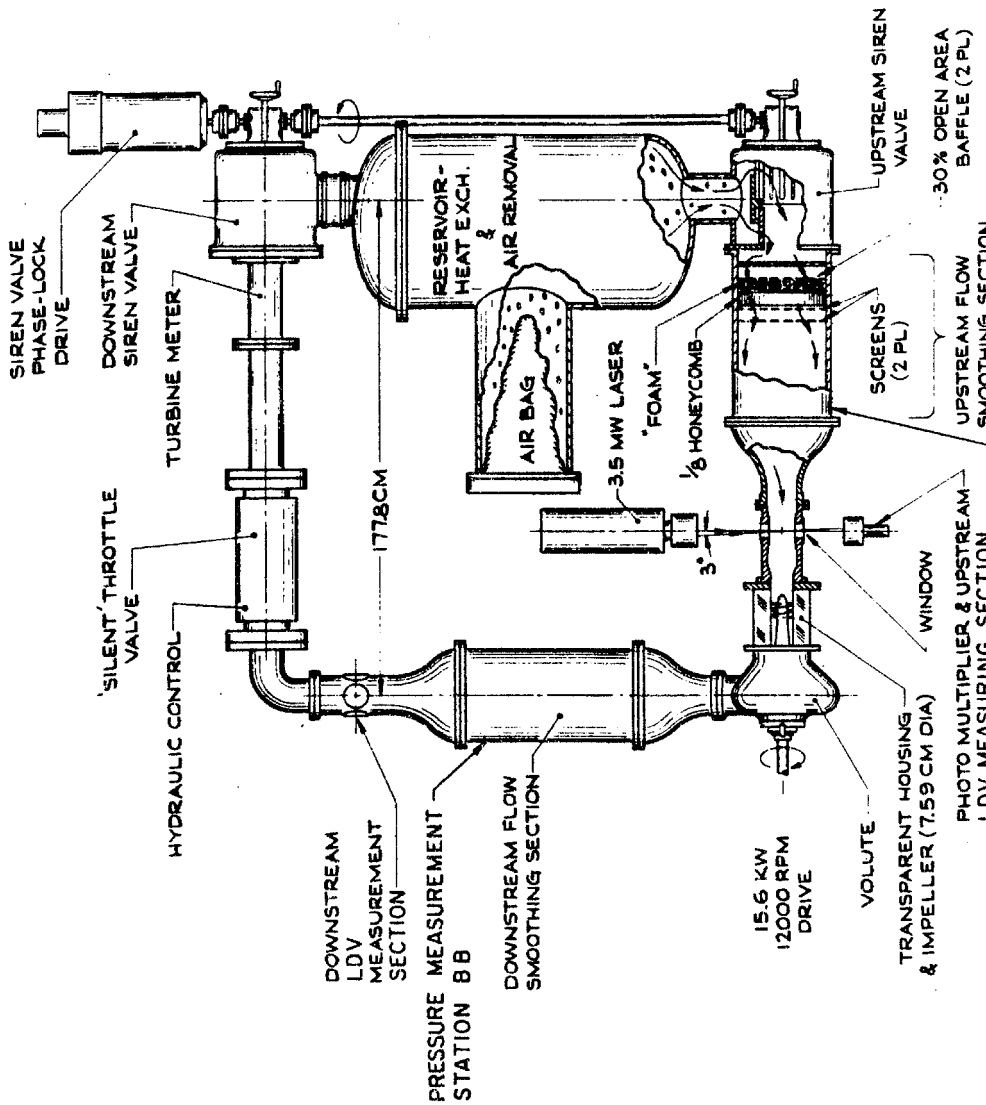

PLAN VIEW

Fig. 2.1 Schematic plan view of the Dynamic Pump Test Facility.

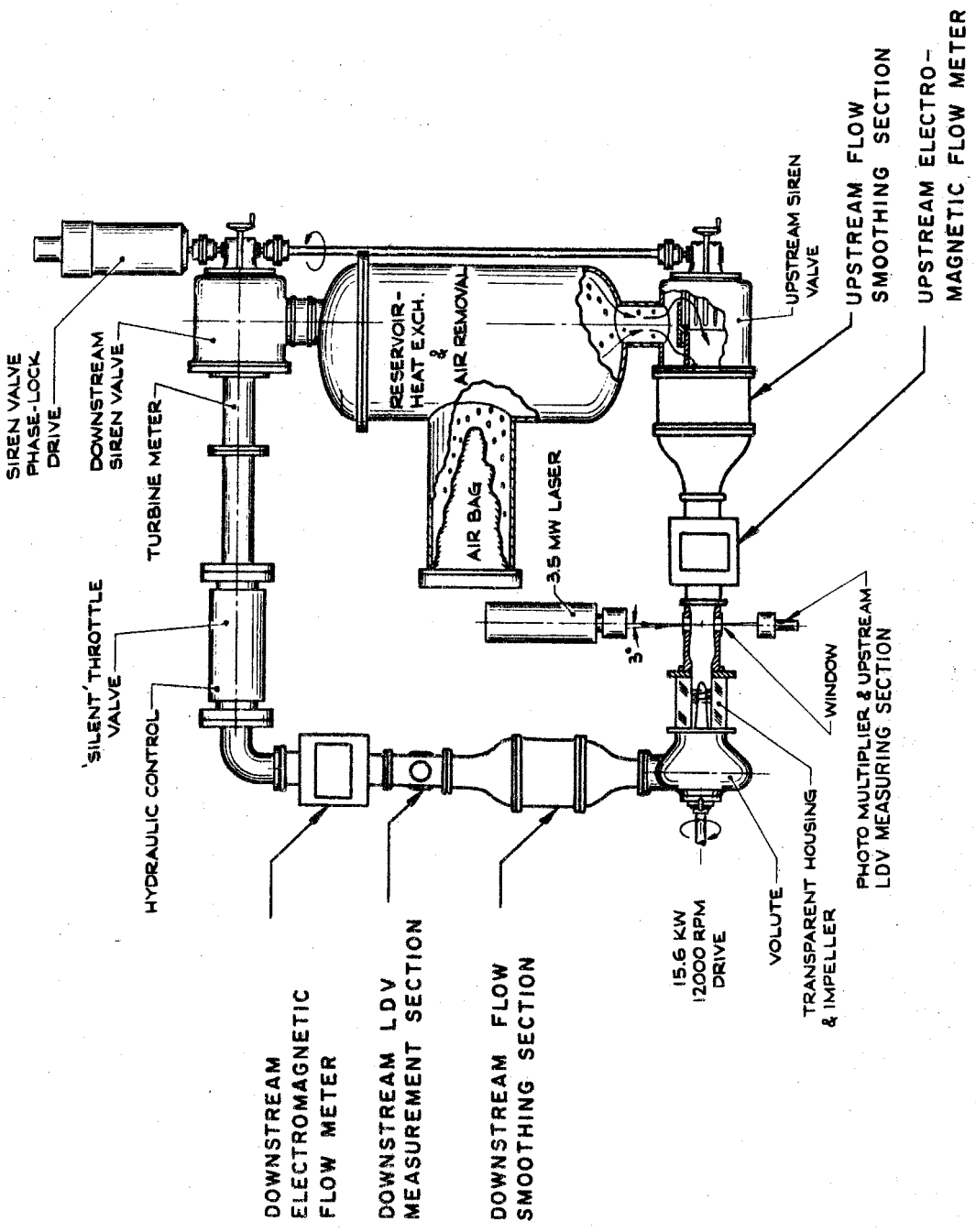

Fig. 2.2 Schematic plan view of the Dynamic Pump Test Facility after modifications.

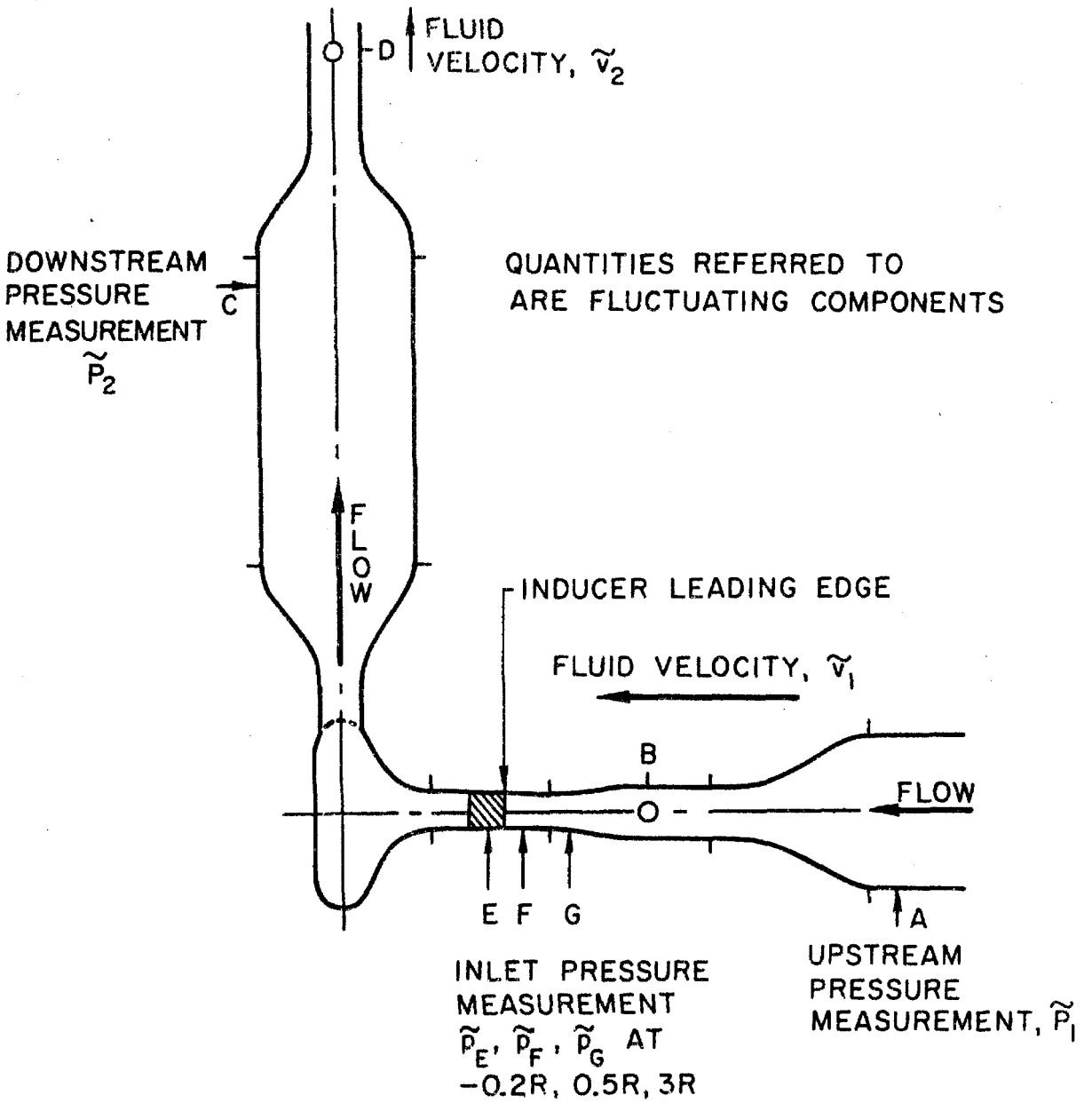

Fig. 2.3 Schematic of transducer locations on the Dynamic Pump Test Facility.

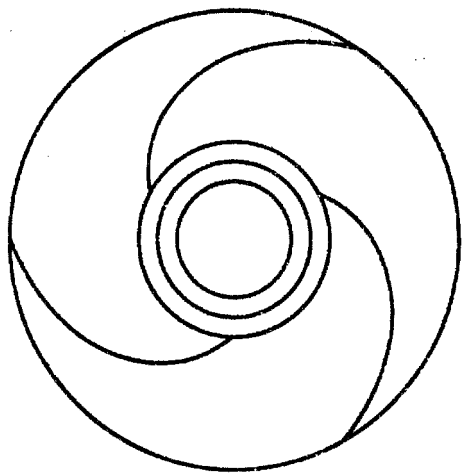

IMP 5

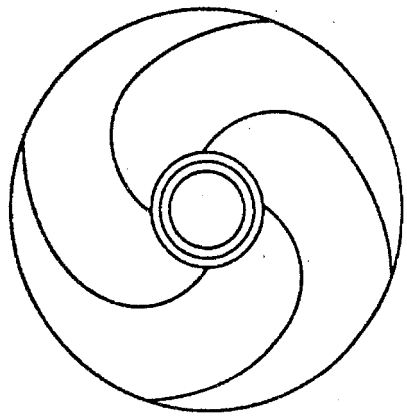

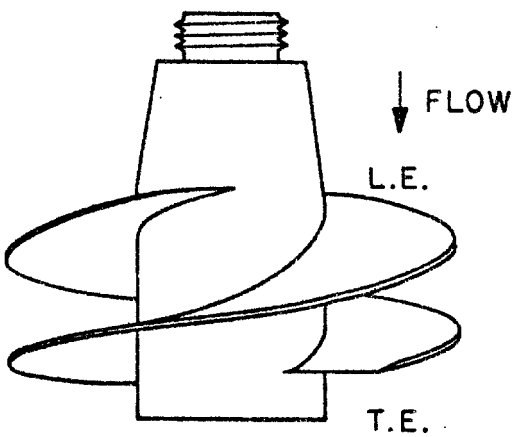

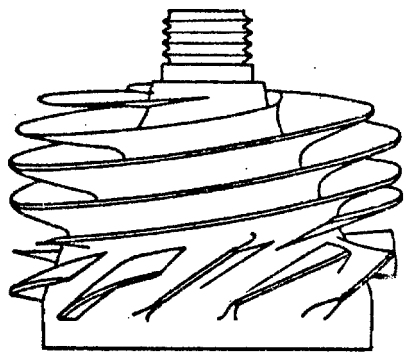

IMP 4

Fig. 2.4 Sketch of Impeller 5 and Impeller 4. Both impellers are 7.62 cm in diameter.

III. STEADY STATE PUMP PERFORMANCE

3.1 Introduction

The performance of pumps has traditionally been characterized by three distinct quantities. Although these quantities appear in many forms in the literature, they are based upon the head rise across the pump, the suction or inlet pressure and the mean flow rate through the pump. For the purposes of this study, these quantities will be non-dimensionalized as follows:

$$\Psi = \frac{p_2 - p_1}{\rho U_T^2} = \text{head coefficient},$$

$$\varphi = \frac{\rho Q}{\rho A_I U_T} = \text{flow coefficient} \qquad (3.1)$$

and

$$\sigma = \frac{p_1 - p_v}{\frac{1}{2}\rho U_T^2} = \text{cavitation number}$$

where

p_2 = discharge pressure

p_1 = inlet pressure

p_v = vapor pressure of liquid

Q = volumetric flow rate

U_T = tip speed of pump

A_I = inlet area of the pump

ρ = liquid density.

Under fully wetted or non-cavitating conditions, the function $\Psi(\varphi)$ is sufficient to describe the performance of a pump. However,

under cavitating conditions, the head coefficient, Ψ, becomes a function of cavitation number, σ, as well.

3.2 Non-Cavitating Pump Performance

The non-cavitating dependence of the head coefficient upon the flow coefficient for both the $\frac{1}{4}$ and $\frac{1}{3}$ scale models of the LPOTP of the SSME, IMP4 and IMP6, is presented in Fig. 3.1. The general form of these characteristics is typical of all inducer pumps. The differences between the performance of IMP4 and IMP6 are due to differences in the efficiency of pressure recovery in the volute. The solid line on this figure is an analytical prediction of the performance of IMP4 and IMP6 [9]. The agreement is quite good, especially near the design flow coefficient of 0.070.

A brief digression will be made at this point to describe the inlet velocity profiles. Knowledge of the inlet velocity profiles is important in that the performance of the inducer is determined by the blade geometry and the local angle of attack.

3.3 Inlet Velocity Field

3.3.1 Introduction

The inlet axial and swirl velocity profiles were obtained by means of a wedge probe and a total head probe connected to a manometer. A radial traverse with the wedge probe determined the angle of the flow. This measurement was followed by a radial traverse with the total head probe to determine the stagnation pressure at the flow angle. The large inertia of the manometer connections effectively averaged out any three dimensional structure in the flow. Under the assumption

of radial equilibrium, the axi-symmetric mean axial and swirl velocities could be calculated as described in Appendix C.

3.3.2 Axial Velocity Profiles

The radial distribution of the axial velocity 0.5 radii upstream of IMP6 is presented in Fig. 3.2. At the higher flow coefficients, the initially (i.e. far upstream) uniform and irrotational inlet flow is slightly retarded at the outer radii. As the flow coefficient is decreased, the amount of retardation increases until a reversed flow region is observed. The extent of the reversed flow region increases with a further decrease in flow coefficient. From Fig. 3.1. the above trend is directly related to a corresponding increase in the head coefficient. The reversed flow region results from a jet that forms in the tip clearance region of the pump. In addition, the presence of the backflow jet causes an acceleration of the fluid at the inner radii due to the reduction in through flow area and the source-like character of the tip clearance flow. The above axial velocity profiles were obtained with IMP6 operating at 4000 RPM. The axial velocity profiles at 6000 RPM are identical to those at 4000 RPM.

In Fig. 3.3, the radial distribution of the axial velocity 1.0 radii upstream of IMP6 is presented. It is apparent from the comparison between Figs. 3.2 and 3.3 that upstream penetration of the backflow jet depends strongly upon the head coefficient. The strength of the backflow or tip clearance jet is therefore determined by the head rise across the impeller as indicated in these figures.

3.3.3 Swirl Velocity Profiles

The swirl velocity profiles 0.5 and 1.0 radii upstream of IMP6

are given in Figs. 3.4 and 3.5. Non-zero swirl velocities only occur for those head coefficients associated with reversed flow in the axial velocity profile. It follows that the prerotation of the inlet flow is induced by the highly rotational fluid of the tip clearance jet. It is interesting to note that the swirl velocities are not, however, confined to the region of reversed flow. As with the axial velocity profiles, the swirl velocity profiles obtained at 6000 RPM are identical to those obtained at 4000 RPM.

The strength or intensity of the swirl velocity distribution is also directly associated with the head coefficient. In addition, the intensity of the swirl velocity is a function of axial position. The intensity of the swirl distribution as well as the extent of the reversed flow region decays axially upstream. A series of flow angle measurements at a cavitation number of 0.10 indicates that the swirl velocity profiles do not vary greatly with the cavitation number. This set of measurements also suggests that the axial velocity profiles are not affected by the increased amounts of cavitation in the backflow jet.

3.3.4 Discussion of Inlet Velocity Profiles

Similar inlet axial and swirl velocity profiles have been found for the Mark 10 liquid oxygen inducer [46,47]. Clearly, the inlet axial and swirl velocity profiles are a complicated function of the head coefficient. Hence, it is not surprising that the analytical performance prediction in Fig. 3.1 [9], which did not account for prerotation of the inlet flow, is more accurate at the higher flow coefficients.

The actual mechanism by which the inlet velocity distributions are developed is not yet fully understood. A large three dimensional structure (i.e. shed vortices) or time dependence (i.e. turbulent mixing) in the flow may contribute significantly to the generation of this flow pattern. However, these effects have been suppressed by the smoothing

of the measurement process. Therefore, a certain amount of caution must be exercised when interpreting or formulating a model based upon these inlet velocity profiles.

3.4 Cavitating Pump Performance

The head coefficient variation with cavitation number for specific flow coefficients is given in Figs. 3.6 and 3.7 for IMP4 and IMP6, respectively. The letters on these figures indicate the mean operating conditions at which transfer functions of these inducers were obtained. These steady state cavitation performance curves are reasonably typical of all inducers. The large fall off in the head coefficient at low cavitation numbers indicates that the impeller is approaching a choked condition due to the presence of cavitation.

In order to describe the various forms and amounts of cavitation that occur within IMP6, photographs of IMP6 at several cavitation numbers are presented in Figs. 3.8-3.10. These photographs were taken at a flow coefficient of 0.070. At high cavitation numbers, cavitation occurs only at the center of the trailing vortex shed from the leading edge of the inducer at the blade tip. As the cavitation number is reduced, cavitation becomes more extensive within the core of the shed vortex and also begins to occur in the remainder of the backflow. Continued reduction of the cavitation number causes the length of the now cavitating backflow to increase along the blade tip. At some cavitation number, an attached blade cavity develops at the leading edge of the inducer. Initially, the attached blade cavity forms near the blade tip. This cavity expands both radially and axially with a further decrease in the cavitation number. When choking occurs,

the cavitating tip clearance flow essentially disappears because of the reduced head production. It is important to notice that,for the most part, the cavitation occurs in the immediate neighborhood of the entrance to the inducer.

In a range of cavitation numbers just above head breakdown, the cavitation pattern becomes unsteady. This unsteadiness is accompanied by large amplitude oscillations in both the pressure and velocity fields. This is the phenomenon of auto-oscillation.

3.5 Initial Observations of Auto-Oscillation

Auto-oscillation is characterized by large amplitude fluctuations in both the inlet and discharge pressures and mass flow rates. These oscillations occurred in a range of cavitation numbers just above head breakdown as indicated by the stars in Fig. 3.6 for IMP4. This agrees with the observations reported in Refs. [2,6,8,21,34,40,56]. At 9000 RPM, the auto-oscillation frequencies ranged between 28 and 35 Hz. Assuming the frequencies scale with the tip speed of the impeller, U_T, the corresponding non-dimensional frequencies are 0.293 and 0.367 respectively (see Eq. 5.2.1).

As the region of auto-oscillation is approached, the cavity length to chord ratio approaches unity. It was observed that under these conditions the length of the cavitating backflow began to fluctuate randomly. The amplitude of these excursions from the mean cavity length increased as the cavity length to chord ratio neared unity. A similar behavior has been reported in Ref. [6] for attached blade

cavities. Since the backflow cavitation obscured the attached blade cavities, such observations were not possible in this study. However, Etter [21] has observed that the "tip cavities tended to collapse at the same point as the base cavities". Once auto-oscillation occurs, the variations in the length of the backflow cavitation are no longer random but periodic at the auto-oscillation frequency. During auto-oscillation, the cavitation on all blades oscillates in unison. The unsteadiness in the cavitation pattern leads to perturbations in the pressure and velocity fields. The low amplitude perturbations in the velocity and pressure fields have a very broad spectrum. It is these fluctuations that eventually receive or accept energy from the inducer and grow to manifest the phenomenon of auto-oscillation.

As the cavitating backflow is increasing in length and just before the onset of auto-oscillation, the cavitating backflow collapses back towards the inlet plane of the pump. This reduced penetration into the inlet flow field suggests that a redistribution of the velocity field occurs at these operating conditions.

Measurements made on the 9^{o}-helical inducer, IMP5, presented in Fig. 3.1 indicate that the frequency of the auto-oscillation is a function of both cavitation number and flow coefficient. The amplitude of the oscillations is also a function of the mean flow rate. Both Sack and Nottage [49] and Miller and Gross [38] have also observed an amplitude dependence on flow coefficient. They found that the amplitude increased with a decrease in flow coefficient.

3.6 Implications of Initial Auto-Oscillation Observations

The fact that large amplitude pressure and mass flow rate

fluctuations were observed throughout the pump loop implies that the system participates in the instability. It is thought [4] that the system determines the frequency of the resulting instability and has a direct influence on the amplitudes as well. If this is so, then combining the dynamics of the system with that of the cavitating inducer should yield predictions of the onset and frequency of auto-oscillation. The modeling procedure suggested above is carried out in the next chapter.

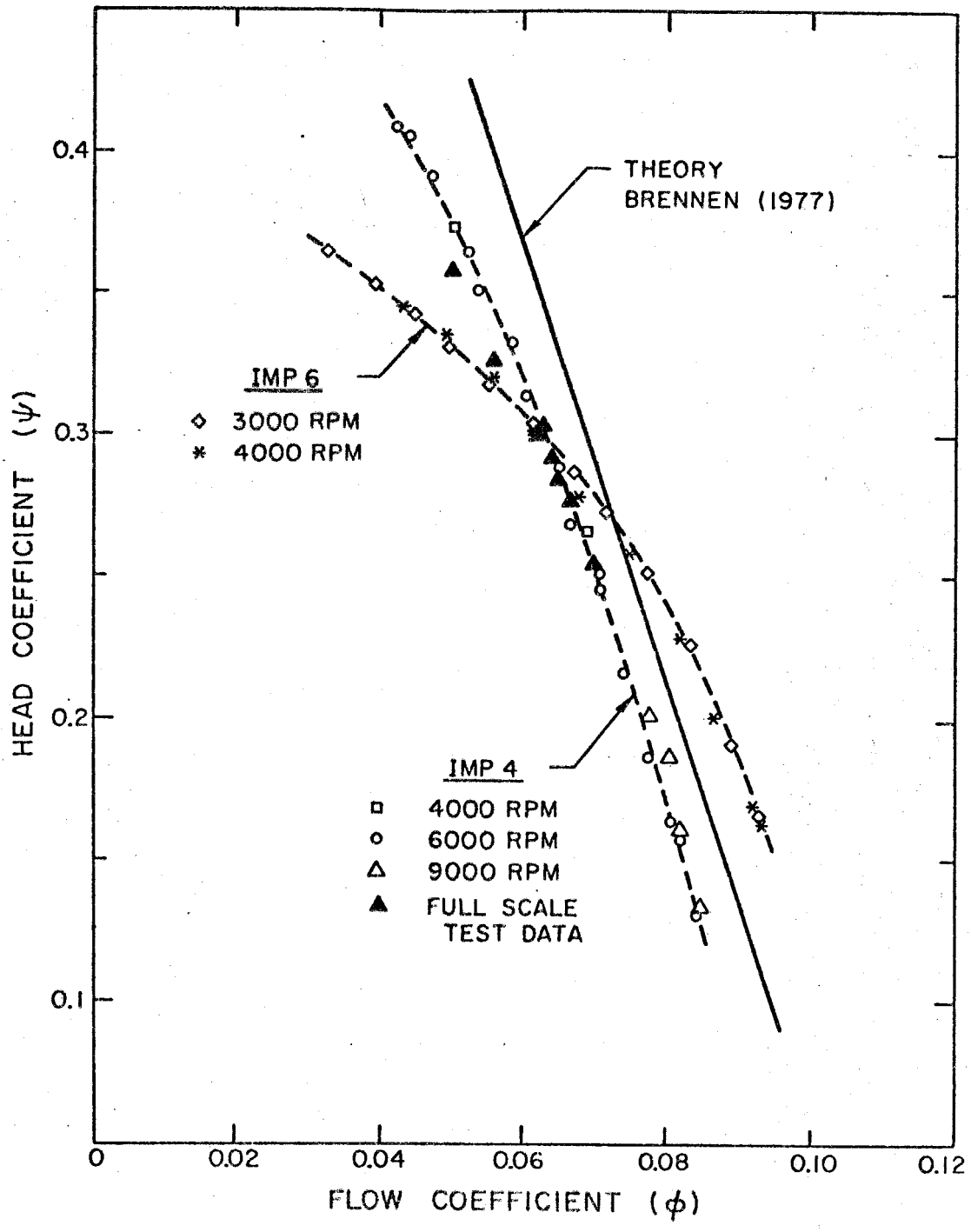

Fig. 3.1 Non-cavitating performance of Impeller 4 and Impeller 6. Also shown are full scale test data for these impellers and a theoretical prediction of their performance (Brennen [9]).

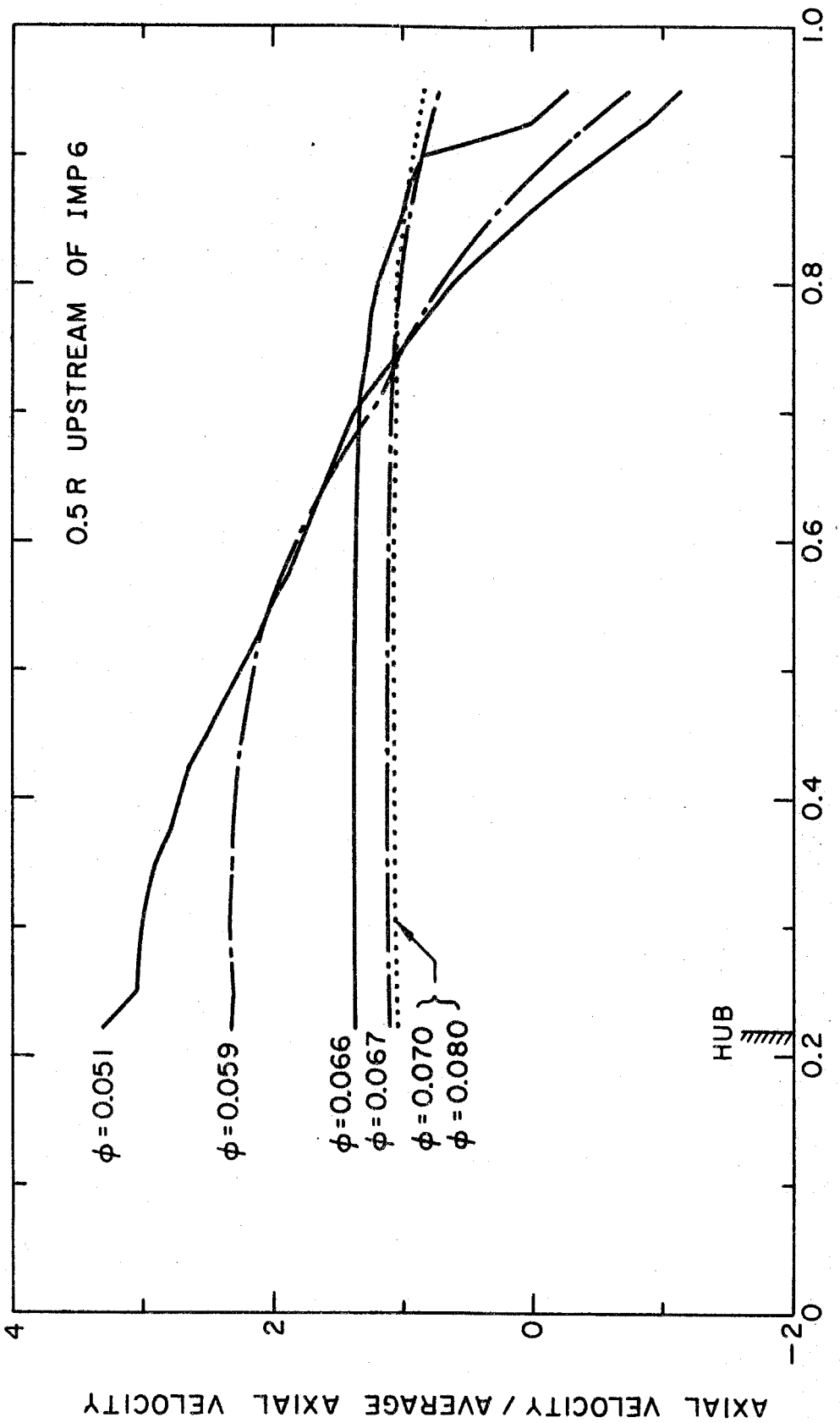

Fig. 3.2 Radial distribution of the axial velocity measured 0.5 radii upstream of Impeller 6 for several flow coefficients, φ.

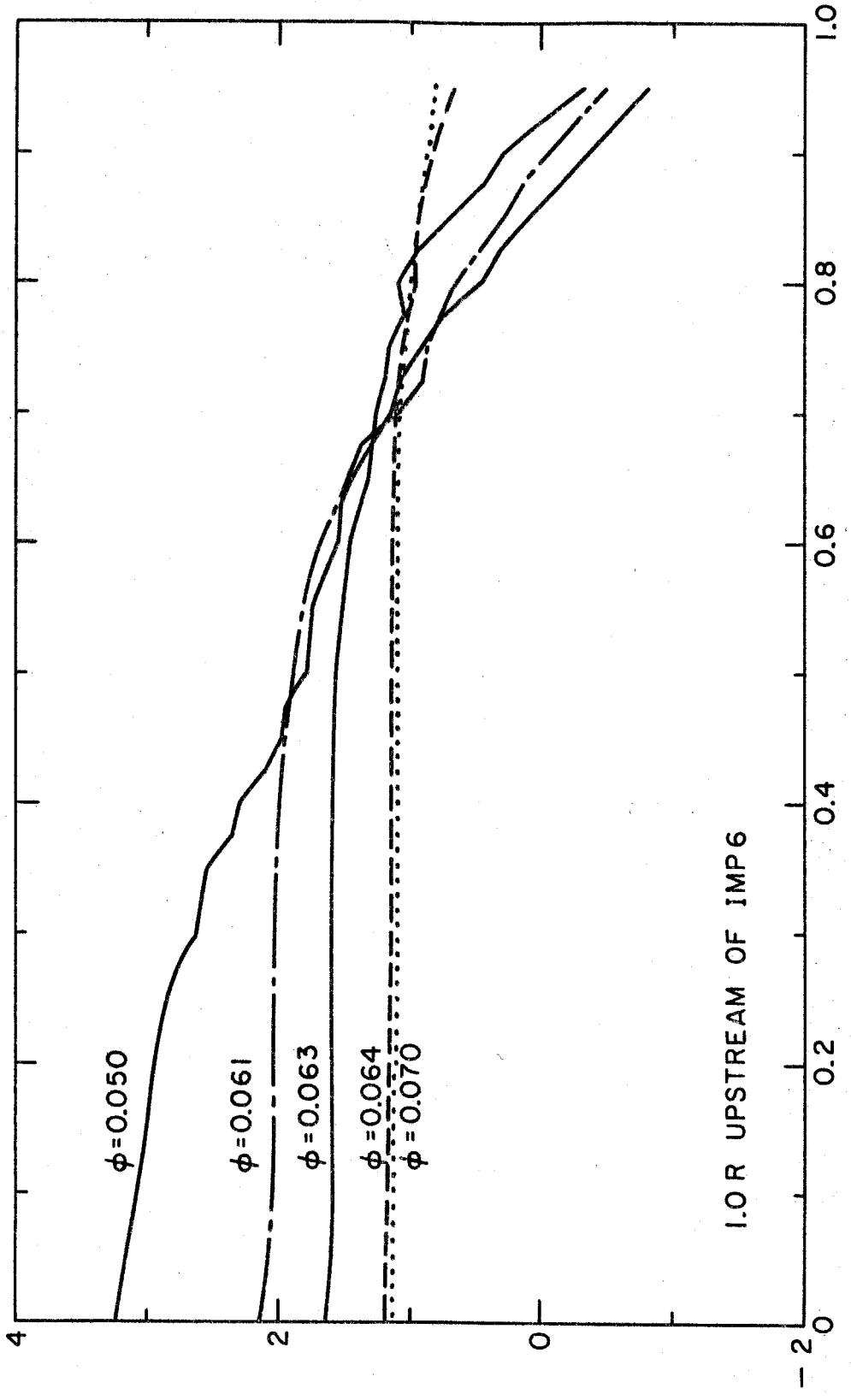

Fig. 3.3 Radial distribution of the axial velocity measured 1.0 radii upstream of Impeller 6 for several flow coefficients, φ.

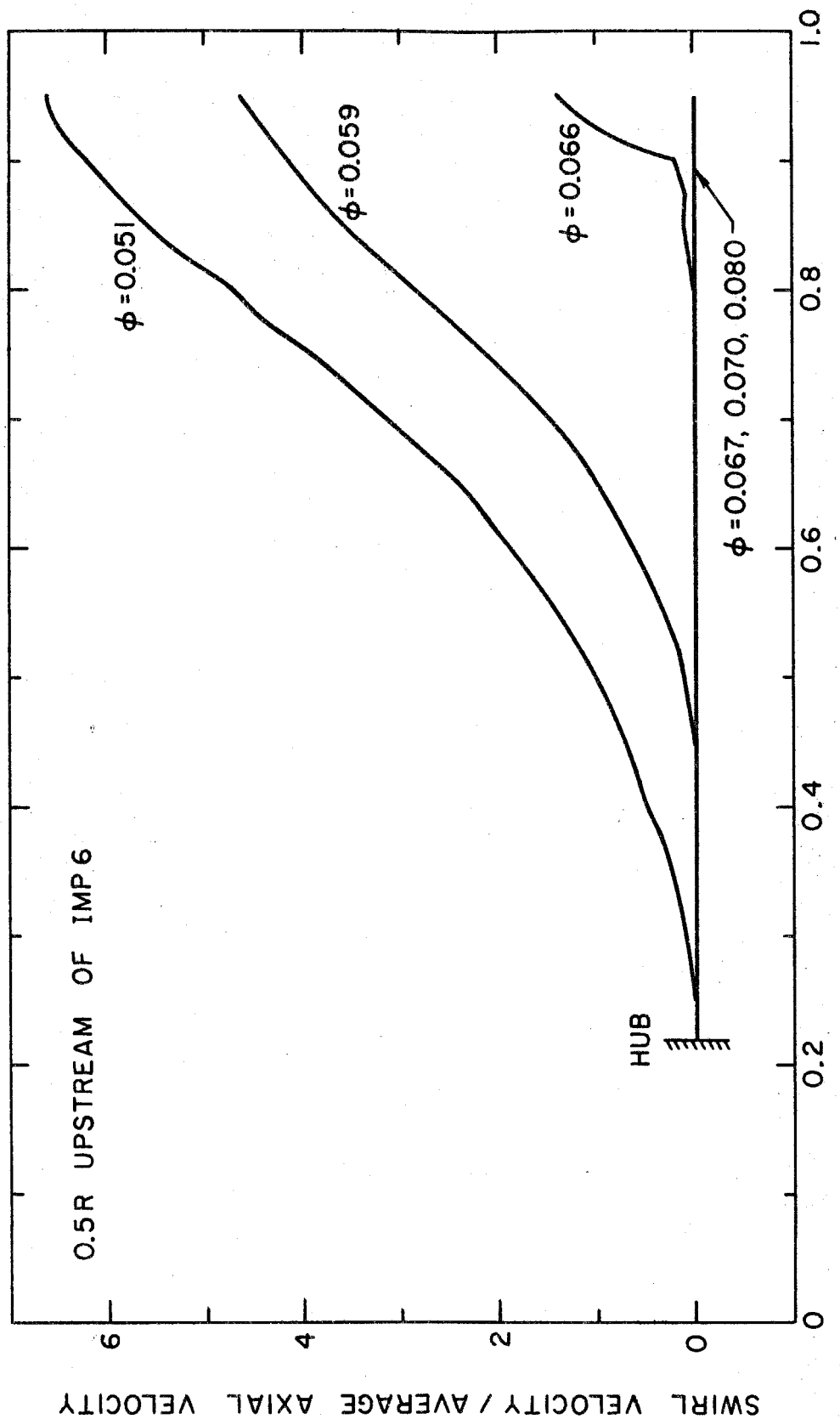

Fig. 3.4 Radial distribution of the swirl velocity measured 0.5 radii upstream of Impeller 6 for several flow coefficients, φ.

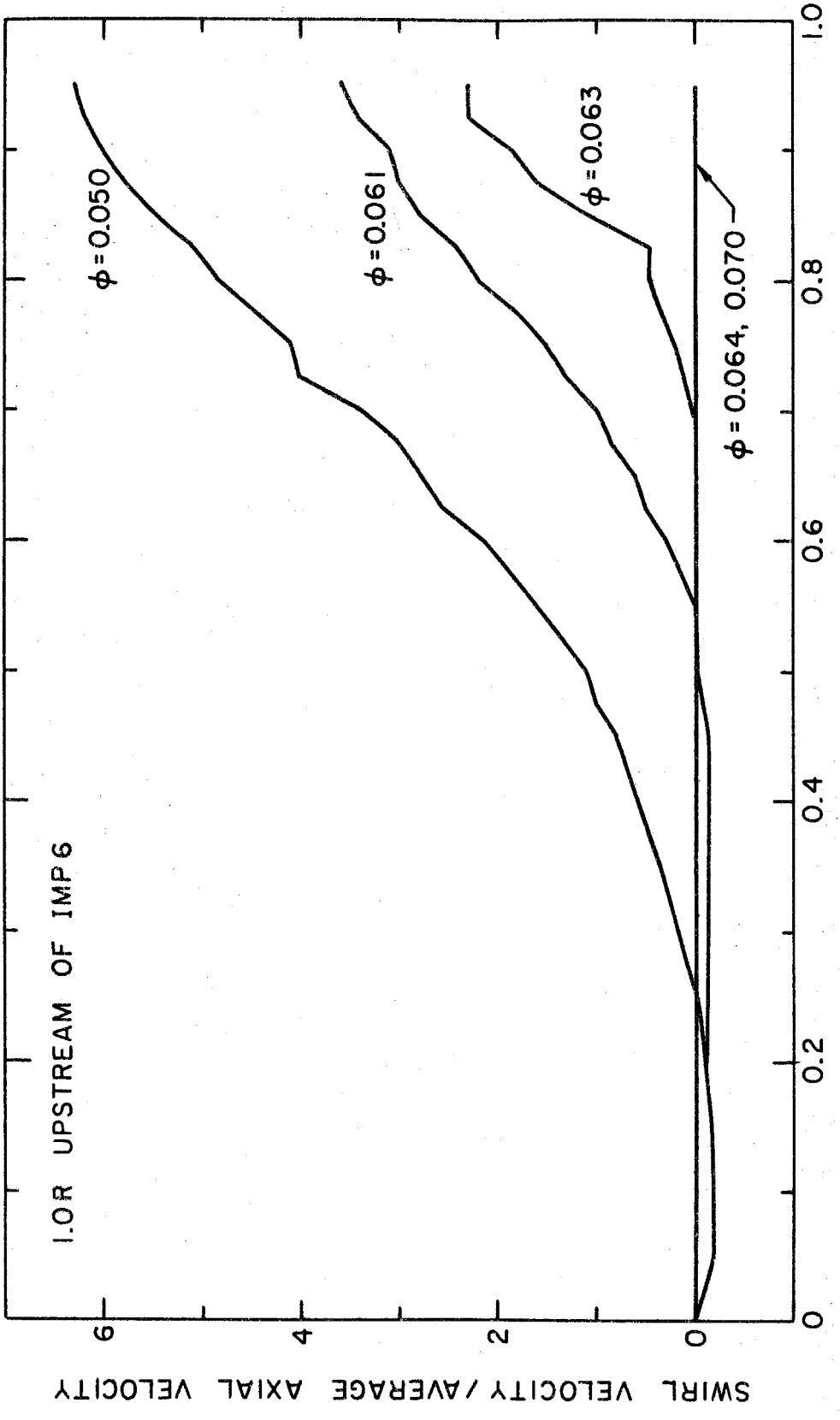

Fig. 3.5 Radial distribution of the swirl velocity measured 1.0 radii upstream of Impeller 6 for several flow coefficients, φ.

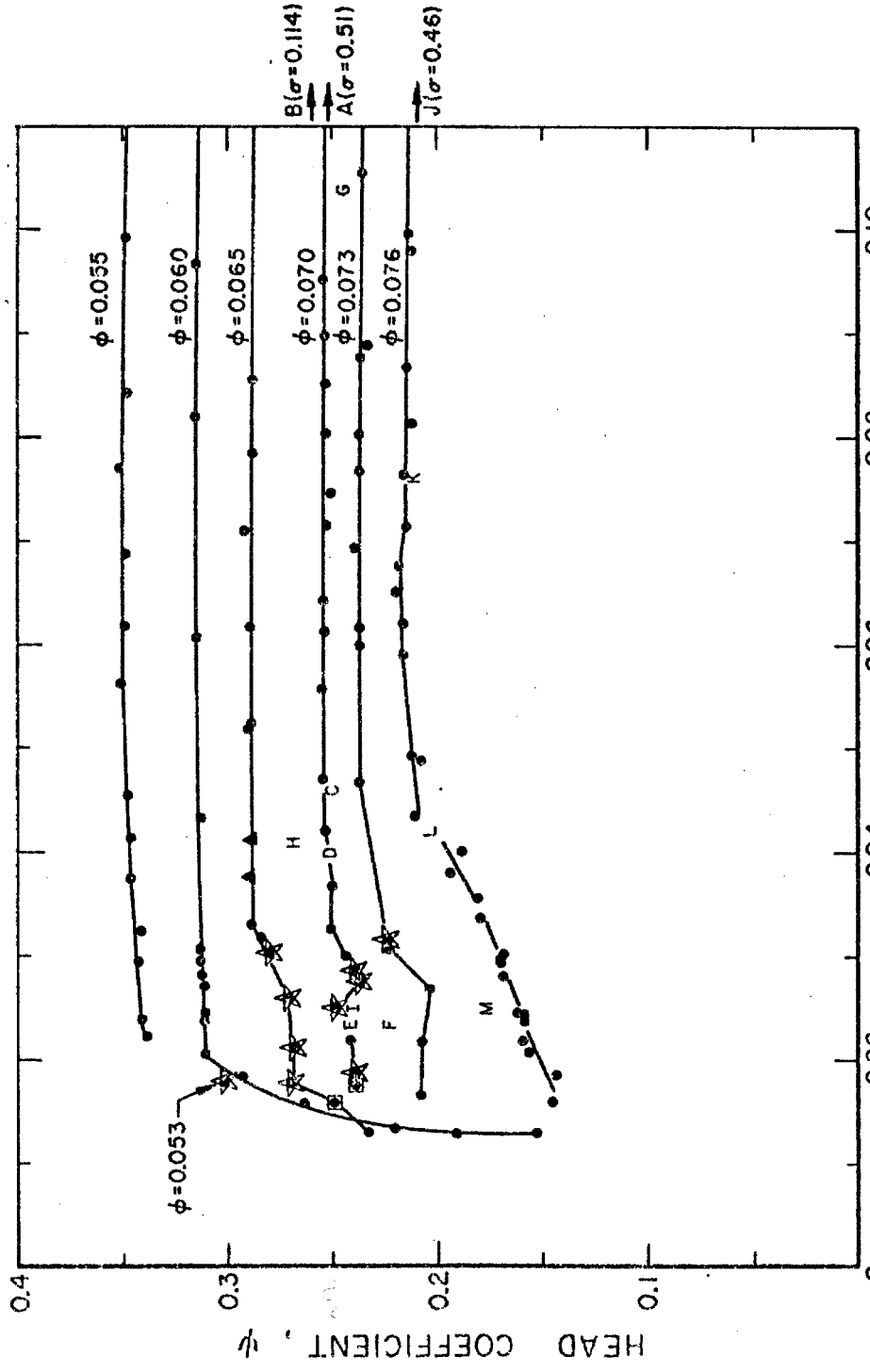

Fig. 3.6 Cavitation performance of Impeller 4 for various flow coefficients. The lettered points indicate the operating conditions at which transfer functions were obtained. The stars indicatepoints at which auto-oscillation occurred.

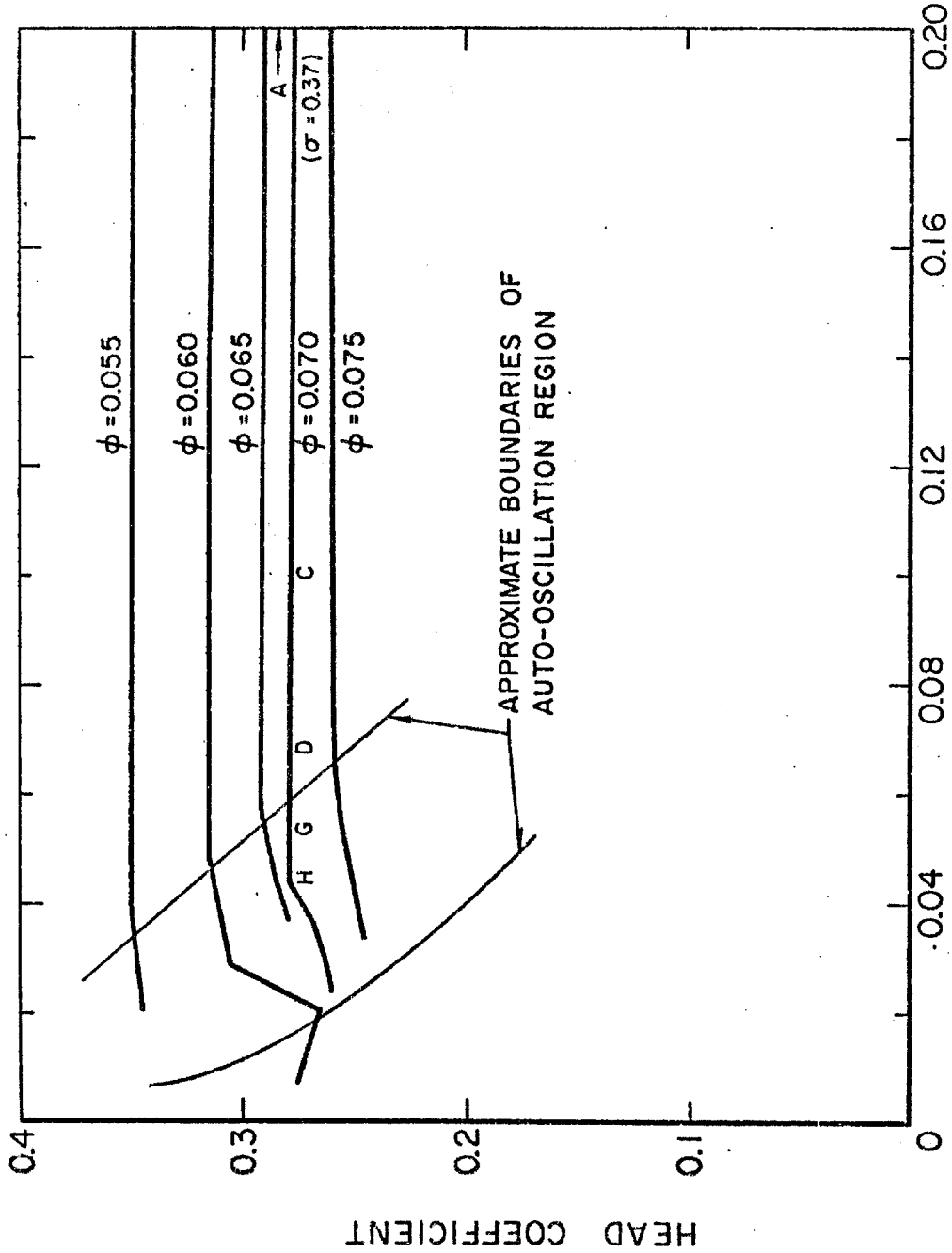

Fig. 3.7 Cavitation performance of Impeller 6 for various flow coefficients. The lettered points indicate the operating conditions at which transfer functions were obtained. Also indicated are the approximate boundaries of the region of auto-oscillation.

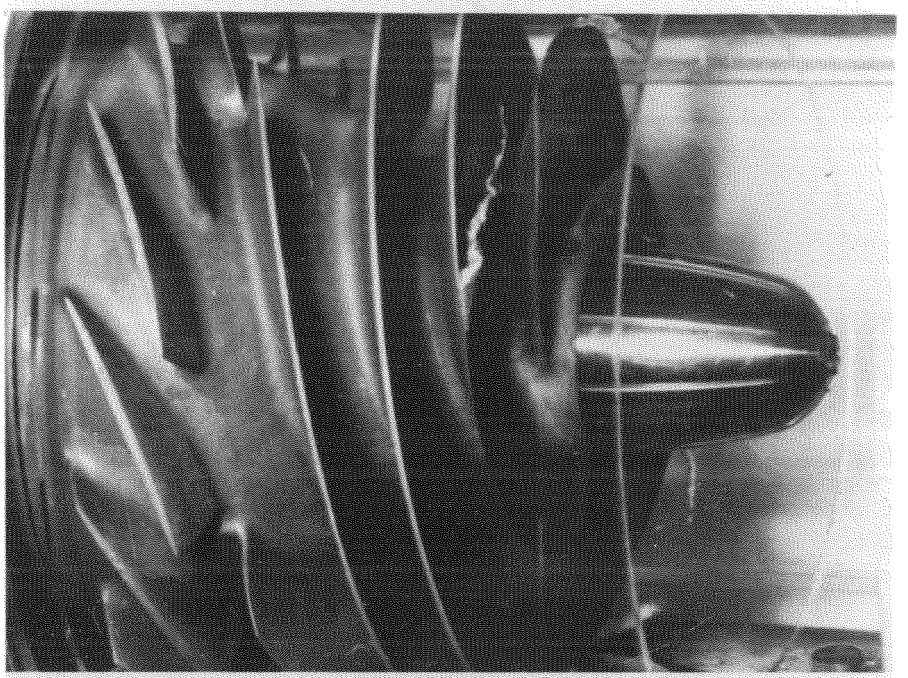

$\sigma = 0.419$

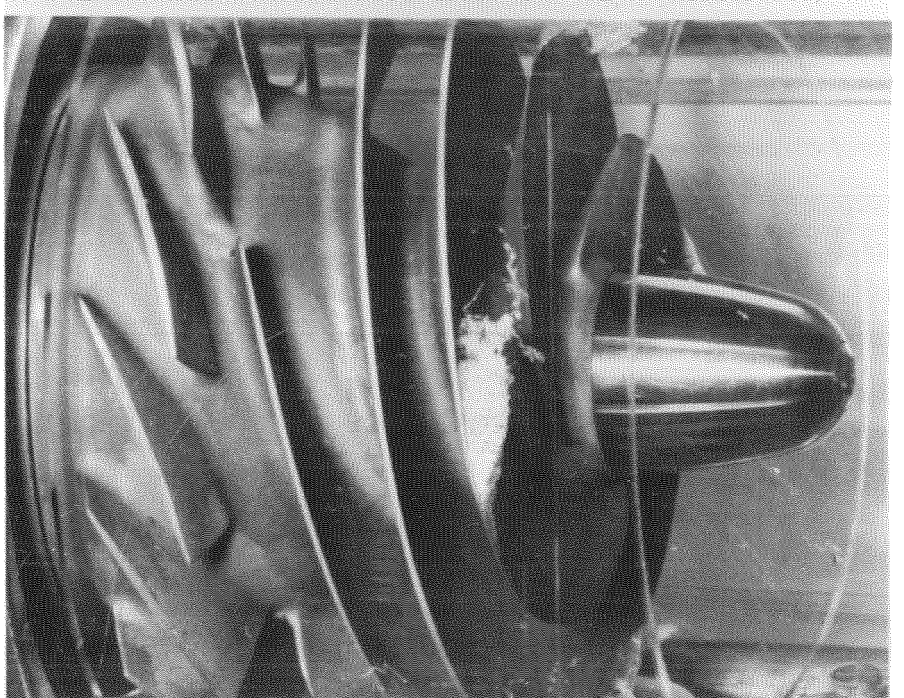

$\sigma = 0.152$

Fig. 3.8 Photographs of Impeller 6 operating at a flow coefficient of 0.070 and at cavitation numbers of 0.419 and 0.152.

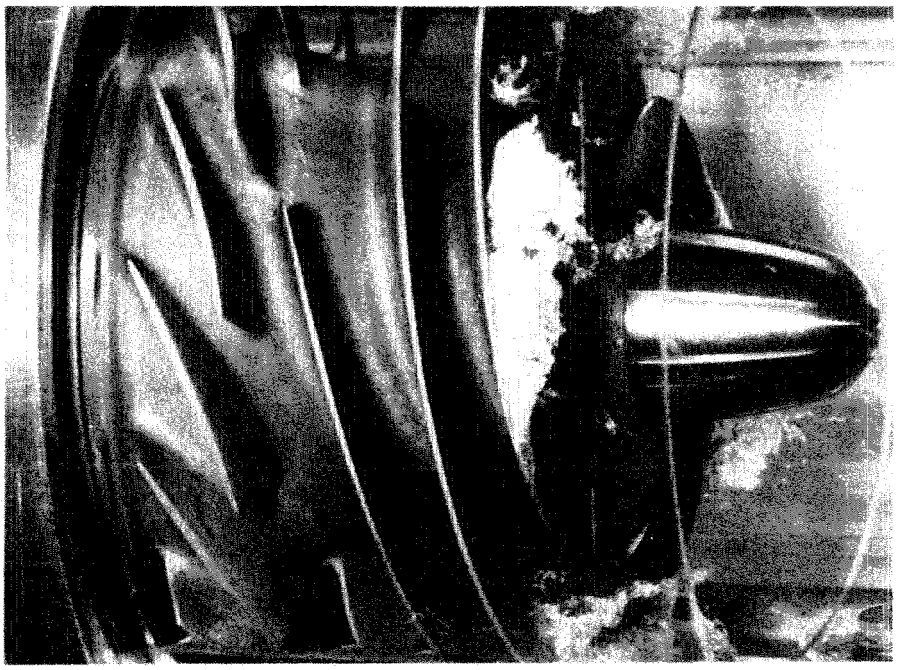

$\sigma = 0.087$

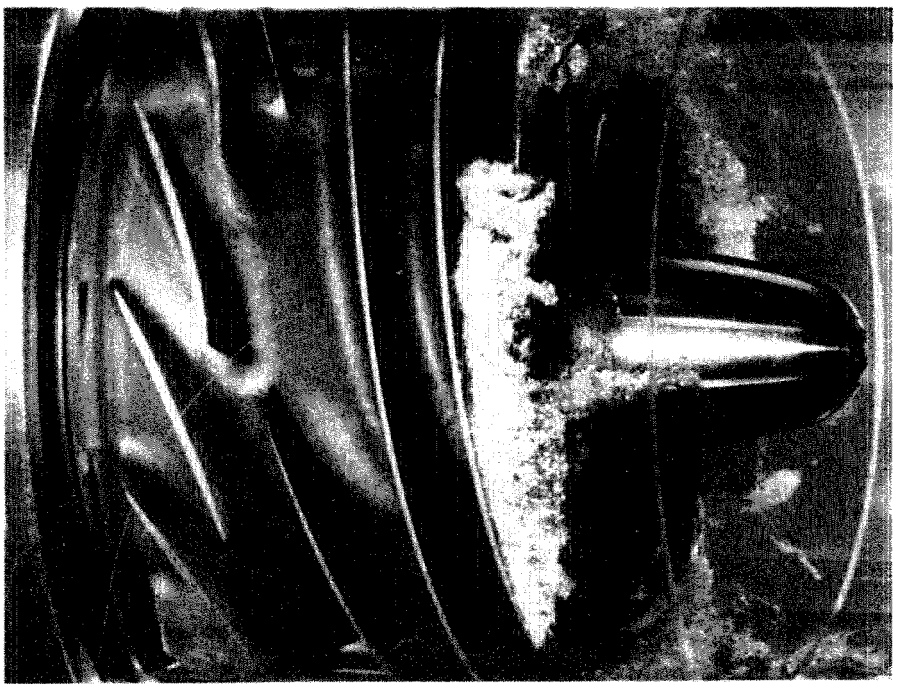

$\sigma = 0.061$

Fig. 3.9 Photographs of Impeller 6 operating at a flow coefficient of 0.070 and at cavitation numbers of 0.087 and 0.061.

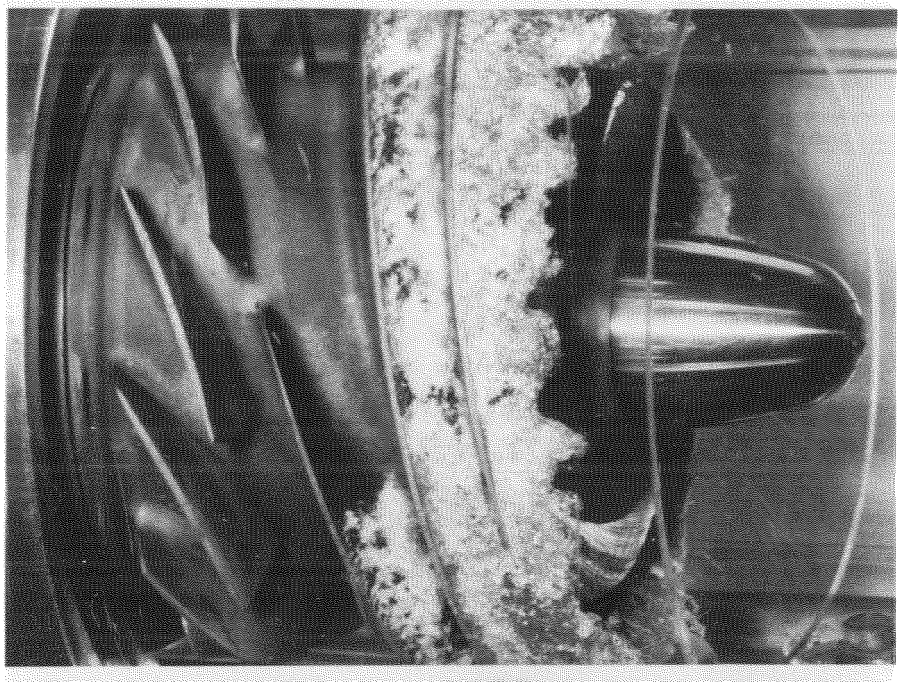

$\sigma = 0.033$

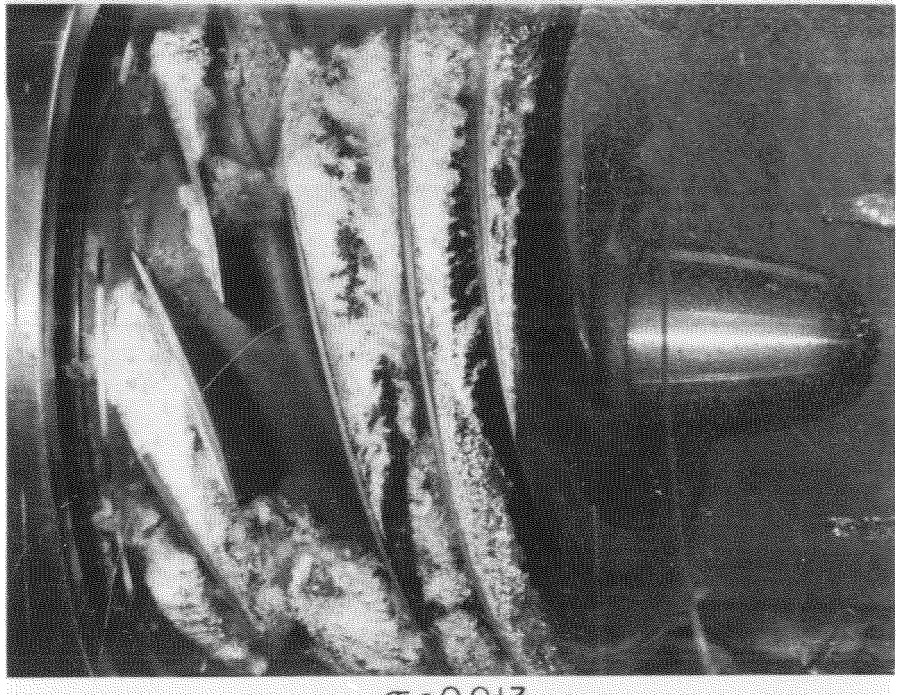

$\sigma = 0.013$

Fig. 3.10 Photographs of Impeller 6 operating at a flow coefficient of 0.070 and at cavitation numbers of 0.033 and 0.013. Auto-oscillation occurred at $\sigma = 0.033$.

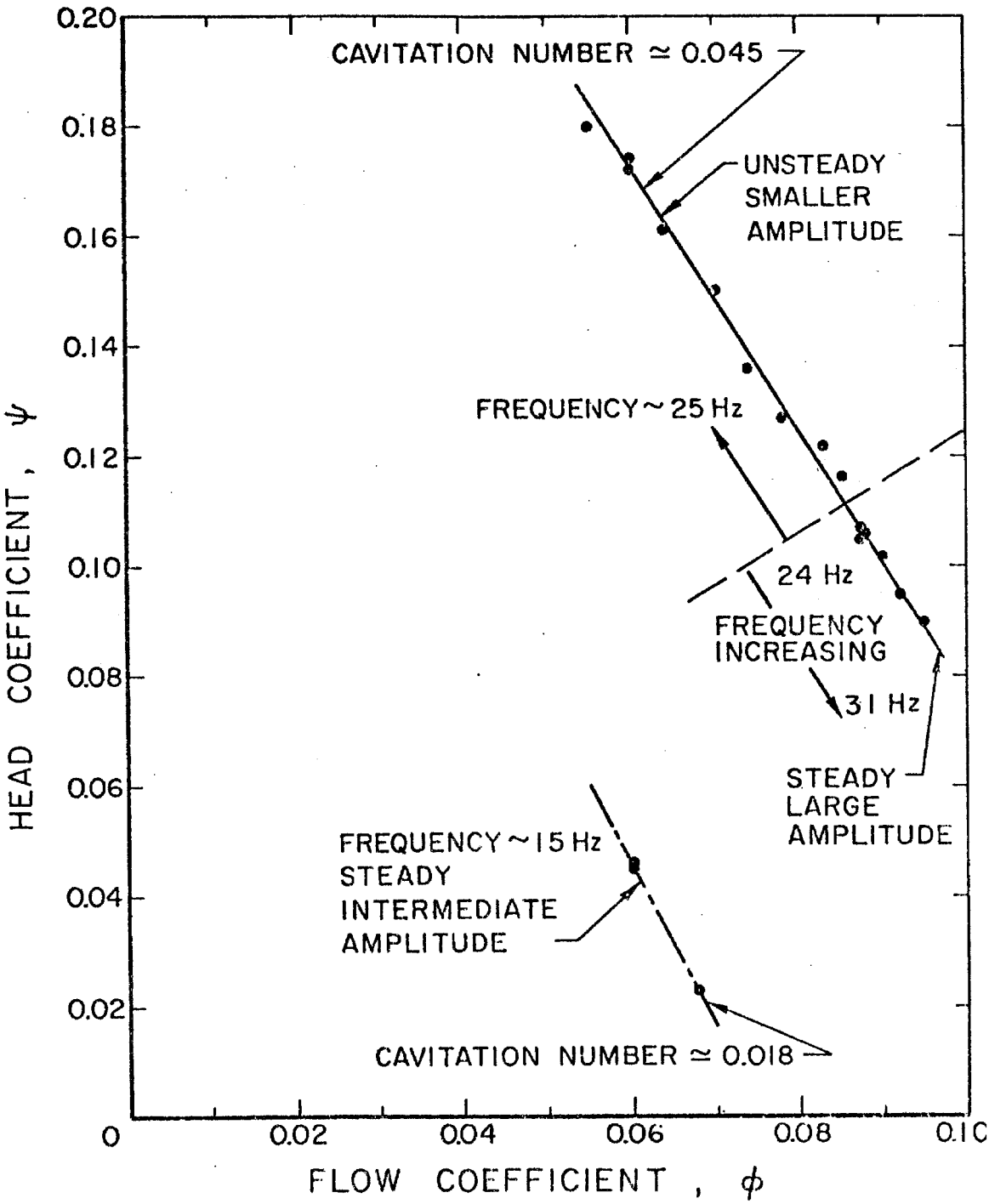

Fig. 3.11 Auto-oscillation measurements associated with Impeller 5.

IV. THE STABILITY OF HYDRAULIC SYSTEMS

4.1 Introduction

In this chapter, a linear stability analysis is developed for the purpose of predicting the onset of auto-oscillation. The analysis is based upon the observation that auto-oscillation is a function of the entire hydraulic system. As a result, the dynamic characteristics of each component of the system have been integrated into the stability analysis. The model of the DPTF used in the analysis consists of four elements. Referring to Fig. 4.1, these four elements are the inlet line, the discharge line, the inducer-volute combination and the air bladder. The linear dynamic behavior of each of these circuit elements is discussed in the following sections. It must be noted, however, that the DPTF does exhibit some nonlinear behavior during auto-oscillation. This is discussed further in Chapter 5.

4.2 Pump Dynamics

4.2.1 Introduction

The dynamic behavior of a cavitating inducer can be represented in terms of a transfer function. The transfer function representation is only valid for linear perturbations. Ng [41] demonstrated that IMP4 acts dynamically as a linear device up to at least a 3% oscillation in the fluctuating upstream mass flow rate. The assumption of linearity is therefore not a serious limitation.

4.2.2 Transfer Function

A transfer function relates a vector of fluctuating quantities that describe the discharge flow field to a vector which describes the

fluctuating quantities that characterize the inlet flow field. The inlet vector also contains information concerning fluctuations in other system parameters, such as the pump rotational speed. The exact form or dimensions that the pump transfer function assumes depends upon the physical situation being modeled. The general representation of the transfer function of a cavitating inducer is

$$\{y\} = [Y]\{x\} \tag{4.2.1}$$

where

$\{y\}$ is the n-dimensional output vector

$\{x\}$ is the m-dimensional input vector

$[Y]$ is the $n \times m$ transfer matrix .

As a result of the large inertia of the drive system, the fluctuations in the rotational speed of the pump were less than 1% at all operating conditions during this investigation and that of Ref.[41]. Brennen and Acosta [15] have shown that if the fractional speed variation is small compared to the percentage fluctuation in the cavitation number (i.e. $\tilde{p}_1^*/\rho U_T^2 \sigma$) then the fractional speed variation has a negligible effect on the transfer function. As a result of the deaeration of the water, the effects or complications of two phase or two component flow can be eliminated from the transfer function. In addition, as long as the flow remains isentropic, thermal effects represented by a fluctuating entropy field are not required for a complete definition of the dynamic behavior of the inducer.

The transfer function of a cavitating inducer satisfying the above assumptions relates the non-dimensional pressure and mass flow rate fluctuations at discharge, $\tilde{p}_2$ and $\tilde{m}_2$, to those quantities at inlet,

$\tilde{p}_1$ and $\tilde{m}_1$. Such a transfer function is expressed by

$$\begin{Bmatrix} \tilde{p}_2 \\ \tilde{m}_2 \end{Bmatrix} = \begin{bmatrix} Y_{11} & Y_{12} \\ Y_{21} & Y_{22} \end{bmatrix} \begin{Bmatrix} \tilde{p}_1 \\ \tilde{m}_1 \end{Bmatrix} \tag{4.2.2}$$

or equivalently

$$\begin{Bmatrix} \tilde{p}_2 - \tilde{p}_1 \\ \tilde{m}_2 - \tilde{m}_1 \end{Bmatrix} = \begin{bmatrix} Z_{11} & Z_{12} \\ Z_{21} & Z_{22} \end{bmatrix} \begin{Bmatrix} \tilde{p}_1 \\ \tilde{m}_1 \end{Bmatrix}$$

where

$$p = \bar{p} + \text{Real}\left\{\tilde{p}e^{j\Omega t}\right\}$$

$$m = \bar{m} + \text{Real}\left\{\tilde{m}e^{j\Omega t}\right\}$$

The pressures and mass flow rates have been non-dimensionalized by $\frac{1}{2}\rho U_T^2$ and $\rho A_I U_T$, respectively.

The experimental techniques and data reduction procedures required to obtain the transfer functions are described in detail in Ref. [41] and will not be repeated here.

At high cavitation numbers, the fluctuating pressure difference would not be expected to depend upon the inlet pressure. Hence, it is expected that $Z_{11} = 0$ at high cavitation numbers. This is confirmed by a quasi-static assumption in which the pump is assumed to traverse its steady state performance curves. The slope of the head coefficient – cavitation number curves, Figs. 3.6 and 3.7, at high cavitation numbers

is zero. Also, if the compliance of the structure and the compressibility of the water is neglected, the two compliance terms, Z_{21} and Z_{22}, should vanish at high cavitation numbers. The quasi-static approximation applied to the head coefficient-flow coefficient curve provides an estimate of the pump resistance or real part of Z_{12}. The value for IMP4 at a flow coefficient of 0.070 is 16 according to Fig. 3.1.

The transfer function of IMP4 operating at a cavitation number of 0.51 and flow coefficient of 0.070 is presented in Fig. 4.2. As expected, Z_{11}, Z_{21} and Z_{22} all vanish; and the real part of Z_{12} does appear to approach the steady state value of 16. However, it is apparent that the quasi-static argument is valid only for very small frequencies. Just how the dynamics of IMP4 are modified as the cavitation number is reduced is answered in Fig. 4.3. In creating this figure, the individual transfer functions were fitted to a power series in $j\Omega$, i.e.

$$Z_{ij} = \sum_{k=1}^{NT} q_{ijk}(j\Omega)^k \quad . \tag{4.2.3}$$

It is the fitted transfer functions with $NT = 3$ that are plotted in this figure. These transfer functions were obtained at the flow coefficient of 0.070 and at various cavitation numbers. Several trends in the data due to a reduction in cavitation number or equivalently an increase in the volume of cavitation present are immediately apparent. The dynamic pressure gain increases more or less monotonically from zero. It is not, however, purely real. A phase shift is definitely indicated by the data. The compliance terms also tend to increase from zero reflecting the increased amounts of cavitation present within the inducer. The

pump impedance, Z_{12}, is a particularly complicated function of frequency and cavitation number. A decrease in the resistive or real part at the higher frequencies with a decrease in cavitation number is the predominant effect. Similar trends occur for IMP6 as indicated in Fig. 4.4. The transfer functions in this figure have also been fitted according to Eq. (4.2.3).

To assess the resulting impact on the overall dynamics of the distinct changes with cavitation number is not trivial, several approaches might be taken. One approach consists of inverse transforming the transfer functions into the time domain and computing the time history of the discharge pressure and mass flow rate for various input wave forms. There are difficulties with such a procedure. This method would also be quite time consuming and the resulting time histories would be difficult to assess. An alternate approach consists of borrowing ideas from electrical network theory. Network theory provides a means of classifying the overall dynamic characteristics of the system according to the relationships between the elements of its transfer function. This second approach is the one undertaken in this investigation. The results of this analysis are presented in the next two sections.

4.2.3 Classification of Linear Systems

Electrical networks, like pumps, are characterized by transfer functions. The transfer function of any four-terminal network is represented by

$$\begin{Bmatrix} e_2 \\ i_2 \end{Bmatrix} = \begin{bmatrix} a & b \\ c & d \end{bmatrix} \begin{Bmatrix} e_1 \\ -i_1 \end{Bmatrix} \tag{4.2.4}$$

where

e_1 and e_2 are the input and output voltages

and

i_1 and i_2 the corresponding currents.

The networks are then classified according to the relationships between the four elements of the transfer function.

Symmetric networks are characterized by only two parameters [17,24,28,54]. All symmetric networks satisfy the following two conditions.

$$a = d \tag{4.2.5}$$

$$\text{determinant} = ad - bc = 1 \tag{4.2.6}$$

By relaxing the first condition, the definition of a reciprocal network is obtained. Four terminal networks containing only resistance, inductance and capacitance elements are reciprocal [24,54]. Those networks which do not satisfy Eq. (4.2.6) are considered non-reciprocal.

The above conditions are valid for discrete, lumped parameter networks. Such systems have an infinite wave propagation speed. However, if a system contains distributed parameters (i.e. finite wave propagation speed), the reciprocity condition is modified. The modulus of the determinant of a distributed parameter reciprocal system is

unity [11]. All fluid systems contain distributed properties and hence must satisfy Eq. (4.2.7) in order to be reciprocal, i.e.

$$|\text{determinant}| = |ad - bc| = 1 \quad . \tag{4.2.7}$$

The flow of a compressible fluid in a rigid, constant area duct with or without frictional resistance illustrates the above statements. This particular flow is known to be reciprocal. The transfer function appropriate to this flow, without going into details, is given in the following set of relations.

$$\begin{aligned}
Y_{11} &= e^{-j\Theta\eta}\left(\cos\Theta + \frac{j}{\eta}\sin\Theta\right) \\
Y_{12} &= \frac{-js}{\eta^2}e^{-j\Theta\eta}\sin\Theta \\
Y_{21} &= -j\left(\frac{\eta^2-1}{s}\right)e^{-j\Theta\eta}\sin\Theta \\
Y_{22} &= e^{-j\Theta\eta}\left(\cos\Theta - \frac{j}{\eta}\sin\Theta\right)
\end{aligned} \tag{4.2.8}$$

where

ω = frequency

s = sonic velocity

L = length of duct

W_0 = average axial velocity

$$\eta = \frac{s}{W_0}$$

$$\Omega = \frac{\omega L}{W_0}$$

$$\Theta = \frac{\Omega\eta}{\eta^2 - 1} \quad .$$

The determinant of this transfer function is

$$\Delta = \det\{Y\} = e^{-2j\theta\eta} \quad . \tag{4.2.9}$$

Clearly, the modulus of the determinant is unity.

The determinants of the fitted transfer functions of IMP4 and IMP6 found in Figs. 4.3 and 4.4 are presented in Figs. 4.5 and 4.6. At high cavitation numbers, the modulus of these determinants is essentially unity. The discrepancy for the IMP4 transfer functions is due to experimental error. However, as the cavitation number is reduced, the modulus of the determinant differs increasingly from unity. This indicates that a cavitating inducer is not a reciprocal device. In addition, it demonstrates that models of the dynamic behavior of a cavitating inducer based upon combinations of resistance, inertance and compliance elements will be in error.

Electrical networks are further classified as to whether they are passive or active. A network is considered active if there is a possible state in which a net amount of energy is delivered by the network [19,28]. The network is passive if it is not active. Unfortunately, a direct connection between the concepts of reciprocal and active does not exist. Generally, reciprocal systems are passive and non-reciprocal systems are active. In order to examine the situation more closely, an energy balance must be performed in order to determine whether a system is passive or not. In the context of a hydraulic system element (such as a cavitating inducer), the physical interpretation or meaning of the above network definition is unclear. Therefore, instead of listing the criteria developed for electrical networks, the appropriate criteria for a hydraulic system element will be derived in the next section.

4.2.4 Energy Considerations

The difference in the flux of energy into and out of the hydraulic system element indicates whether or not it can provide the energy needed to sustain an instability. The flux of energy of an incompressible fluid is defined by

$$E = \text{energy flux} = Aw^*\left(p^* + \frac{1}{2}\rho w^{*2}\right) = \frac{m^* h^*}{\rho} \qquad (4.2.10)$$

$$m^* = \rho A w^* = \text{mass flow rate}$$

$$h^* = p^* + \frac{1}{2}\rho w^{*2} = \text{total head} \quad .$$

Converting to the non-dimensional variables, the energy flux is now defined by

$$\mathcal{E} = \frac{E}{\frac{1}{2}\rho A U_T^3} = mh \qquad (4.2.11)$$

where

$$m = \frac{m^*}{\rho A U_T}$$

$$p = \frac{p^*}{\frac{1}{2}\rho U_T^2} \quad .$$

The total head and mass flow rates can be separated into a mean or steady components, H and $\mathfrak{m}$, and fluctuating components, $\tilde{h}$ and $\tilde{m}$, according to

$$h = H + \text{Real}\left\{\tilde{h}e^{j\Omega t}\right\}$$
$$m = \mathbb{m} + \text{Real}\left\{\tilde{m}e^{j\Omega}\right\} \qquad (4.2.12)$$

Equations (4.2.11) and (4.2.12) yield an energy flux difference as follows:

$$\begin{aligned}\Delta\mathcal{E} &= m_2h_2 - m_1h_1 \\ &= \mathbb{m}_2H_2 - \mathbb{m}_1H_1 + \mathbb{m}_2\text{Real}\left\{\tilde{h}_2e^{j\Omega t}\right\} \\ &\quad + H_2\text{Real}\left\{\tilde{m}_2e^{j\Omega t}\right\} - \mathbb{m}_1\text{Real}\left\{\tilde{h}_1e^{j\Omega t}\right\} \\ &\quad - H_1\text{Real}\left\{\tilde{m}_1e^{j\Omega t}\right\} + \tfrac{1}{2}\text{Real}\left\{\tilde{m}_2\tilde{h}_2e^{2j\Omega t}\right\} \\ &\quad - \tfrac{1}{2}\text{Re}\left\{\tilde{m}_1\tilde{h}_1e^{2j\Omega t}\right\} + \tfrac{1}{4}\left[\bar{\tilde{m}}_2\tilde{h}_2 + \tilde{m}_2\bar{\tilde{h}}_2 - \bar{\tilde{m}}_1h_1 - \tilde{m}_1\bar{\tilde{h}}_1\right] .\end{aligned} \qquad (4.2.13)$$

It is important to realize that only those terms in Eq. (4.2.13) which contribute to a net change in energy over one cycle of the oscillation can provide the energy needed to sustain the auto-oscillation. Hence, a hydraulic system element will be defined as active if the following quantity, $\Delta\mathcal{E}_{osc}$, is positive for some combination of the fluctuating total heads and mass flow rates.

$$\Delta\mathcal{E}_{osc} = \tfrac{1}{4}\left[\bar{\tilde{m}}_2\tilde{h}_2 + \tilde{m}_2\bar{\tilde{h}}_2 - \bar{\tilde{m}}_1\tilde{h}_1 - \tilde{m}_1\bar{\tilde{h}}_1\right] . \qquad (4.2.14)$$

The total head and mass flow rate fluctuations at discharge are related to those quantities at inlet by the pump transfer function. Substituting from Eq. (4.2.2) yields the following result

$$\Delta\mathcal{E}_{osc} = \tfrac{1}{4}\left[\mathcal{A}|\tilde{h}_1|^2 + \mathcal{B}|\tilde{m}_1|^2 + 2\,\text{Real}\left\{(\mathcal{C}-1)\bar{\tilde{h}}_1\tilde{m}_1\right\}\right] \qquad (4.2.15)$$

where

$$\mathcal{A} = \overline{Y}_{11} Y_{21} + Y_{11} \overline{Y}_{21}$$

$$\mathcal{B} = \overline{Y}_{12} Y_{22} + Y_{12} \overline{Y}_{22}$$

$$\mathcal{C} = \overline{Y}_{11} Y_{22} + Y_{12} \overline{Y}_{21} \quad .$$

The form of $\mathcal{C}$ in Eq. (4.2.15) is suggestive of the determinant, $\mathcal{D}$, of the transfer function. After some algebraic manipulations, the following identity is obtained.

$$|\mathcal{C}|^2 = |\mathcal{D}|^2 + \mathcal{A}\mathcal{B} \tag{4.2.16}$$

where

$$\mathcal{D} = \det\{Y\} \quad .$$

An alternate form of Eq. (4.2.15) is

$$\Delta \mathcal{E}_{osc} = \frac{1}{4}\left[\left| \tilde{h}_1 + \tilde{m}_1 \frac{(\mathcal{C} - 1)}{\mathcal{A}} \right|^2 \mathcal{A} + |\tilde{m}_1|^2 \frac{\mathcal{A}\mathcal{B} - |\mathcal{C} - 1|^2}{\mathcal{A}} \right] \quad . \tag{4.2.17}$$

According to the definition given above, a hydraulic system element and in particular a cavitating inducer is an active device if the net energy flux, $\Delta \mathcal{E}_{osc}$, is a positive quantity for at least one possible combination of $\tilde{h}_1$ and $\tilde{m}_1$. The necessary conditions for an inducer to be an absolutely or completely passive device are, from Eq. (4.2.17),

$$\mathcal{A} \leq 0 \tag{4.2.18}$$

and

$$|\mathcal{C} - 1|^2 - \mathcal{A}\mathcal{B} \leq 0 \quad . \tag{4.2.19}$$

The second condition, Eq. (4.2.19), upon substitution of Eq. (4.2.16) becomes

$$\text{Real}\{\mathcal{C}\} \geq \frac{1+|\mathcal{D}|^2}{2} \quad . \tag{4.2.20}$$

Equation (4.2.19) also indicates that $\mathcal{B}$ must be less than zero for this condition to be satisified. If either of the above conditions is not satisfied, then the inducer is an active device.

A set of sufficient conditions which determine whether the inducer is active at a particular operating condition can also be derived. If the dynamics of the cavitating inducer cause any or all of the following relations to be satisfied or Eqs. (4.2.18)-(4.2.20) fail to be satisfied, then the inducer is active.

$$\mathcal{B} > 0$$

and

$$|\mathcal{D}| \geq \frac{|\mathcal{G}|}{2} \frac{|\tilde{h}_1|}{|\tilde{m}_1|} + \frac{|\mathcal{B}|}{2} \frac{|\tilde{m}_1|}{|\tilde{h}_1|} \tag{4.2.21}$$

It is interesting to determine under what conditions an inducer is dynamically active during non-cavitating operation. At high cavitation numbers, $Y_{11} = Y_{22} = 1$ and $Y_{21} = 0$. Substituting, it is found that

$$\begin{aligned} \mathcal{G} &= 0 \\ \mathcal{C} &= 1 \\ \mathcal{D} &= 1 \\ \mathcal{B} &= 2\,\text{Real}\{Y_{12}\} = -2\mathcal{R}_p \end{aligned} \tag{4.2.22}$$

where

$$\mathcal{R}_p = \text{pump resistance} \quad .$$

Clearly, as long as the pump resistance is positive, the inducer remains a passive device. However, should the pump resistance become negative, the inducer is then an active device. A negative pump resistance can occur if the head coefficient – flow coefficient characteristic has a positive slope. A negative pump resistance may also be achieved dynamically. For IMP4, this occurs only at low cavitation numbers (see Fig. 4.3).

The parameters $\mathfrak{A}$, $\mathfrak{B}$, $\mathfrak{N}$ and $|\mathfrak{C}-1|^2-\mathfrak{A}\mathfrak{B}$ have been calculated for all of the IMP4 and IMP6 transfer functions. It turned out that $\mathfrak{A}$ was invariably negative. $\mathfrak{B}$ was negative for all IMP6 transfer functions. In the lower cavitation number IMP4 transfer functions(i.e. σ=0.040, 0.024), $\mathfrak{B}$ did become positive at the higher frequencies. However, the parameter $|\mathfrak{C}-1|^2-\mathfrak{A}\mathfrak{B}$ appeared to be the most sensitive criterion for the active-passive distinction. This parameter has been plotted in Figs. 4.7 and 4.8 for IMP4 and IMP6 respectively. According to Eq. (4.2.19), IMP4 is an active device. IMP6 is similarly an active device, particularly at low cavitation numbers and high frequencies. A comparison between Figs. 4.7 and 4.8 indicates that IMP6 is not as active a device as is IMP4.

4.3 Linear Stability Analysis

4.3.1 Introduction

The existence of instabilities within a hydraulic system containing a dynamically active cavitating inducer is not surprising. The dynamic characteristics of the remaining components of the system need to be specified before beginning the stability analysis.

4.3.2 Dynamic Model of Inlet and Discharge Lines

The inlet and discharge sections of the DPTF defined in Fig. 4.1 will be modeled dynamically by transfer functions. The assumptions outlined in Section 4.2.2 concerning the inducer apply for these components as well. In addition, it shall be assumed that compliance effects are negligible. This condition is perhaps too restrictive; but it is forced upon the analysis by experimental difficulties in measuring more than one mass flow rate. Even so, the compliance terms, Y_{21} and Y_{22}, are not expected to contribute significantly to the dynamics. The above restrictions concerning the dynamic behavior of the inlet and discharge lines reduce the model of these components to impedances, I_U and I_D respectively. The transfer function under the above assumptions takes the following form

$$[Y] = \begin{bmatrix} 1 & -I \\ 0 & 1 \end{bmatrix} \qquad (4.3.1)$$

where

I = Impedance of line element .

The impedances, I_U and I_D, have also been assumed independent of the mean pressure level occurring within the corresponding line element. The impedances are, however, both complex and functions of frequency.

These system impedances have been experimentally measured. The details of the experimental techniques are provided in Appendix B. The resulting system impedances are presented in Figs. B.1–B.4. It should be noted that the determinant of the transfer functions of these system components is identically unity. In addition, according to the criteria expressed in Eq. (4.2.15), these components dissipate

energy. Hence, the inlet and discharge lines are passive systems.

4.3.3 Dynamic Model of Air Bladder

The air bladder will be modeled solely as a compliant element. The transfer function of a simple compliant element has the following form

$$[Y] = \begin{bmatrix} 1 & 0 \\ -j\Omega C & 1 \end{bmatrix} \quad ; \qquad (4.3.2)$$

where

C = compliance of air bladder.

Again, the determinant of the transfer function of a simple compliant element is identically unity. In addition, according to Eq. (4.2.15), a simple compliant element does not supply or extract energy from the oscillations (i.e. $\Delta \mathcal{E}_{osc} = 0$). Hence, the air bladder is also a passive element.

This completes the characterization of the dynamic behavior of each component comprising the DPTF.

4.3.4 Derivation of Stability Criteria

The final model of the DPTF dynamics is illustrated in Fig. 4.9. One way to evaluate the overall stability of the system is to "open" the system at some point. Since the final conclusions do not depend upon the actual location of this break-point, the circuit will be "opened" at the point labeled by the X in Fig. 4.9. By combining the transfer matrices of each system component appropriately, the transfer function of the entire open system, [S], is obtained. The elements of [S] are:

$$S_{11} = 1 + Z_{11} - j\Omega C\left(Z_{12} - I_U(1 + Z_{11})\right)$$

$$S_{12} = \frac{U_T}{2A}\left(Z_{12} - (I_U + I_D)(1 + Z_{11}) + j\Omega C(I_D Z_{12} - I_U I_D(1 + Z_{11}))\right)$$

$$S_{21} = \frac{2A}{U_T}\left(Z_{21} - j\Omega C\,(1 + Z_{22} - I_U Z_{21})\right) \qquad (4.3.3)$$

$$S_{22} = 1 + Z_{22} - (I_U + I_D)\,Z_{21} + j\Omega C\left(I_D(1 + Z_{22}) - I_U I_D Z_{21}\right) .$$

The difference between the flux of energy leaving and entering the system provides a measure of the stability of the entire system. When averaged over one cycle of the oscillations, an excess of energy in the flow leaving the system would help to sustain an auto-oscillation. If a deficit in the discharge flow energy occurs, the system would be unquestionably stable. The ideal neutral stability point is given by a perfect balance in the net energy flux.

Proceeding as before, the net differences between the non-dimensional energy flux into and out of the system is given in Eq. (4.3.4)

$$\Delta \mathcal{E}_{osc} = \frac{1}{4}\left\{\bar{\tilde{m}}_1 \tilde{h}_1 + \tilde{m}_1 \bar{\tilde{h}}_1 - \bar{\tilde{m}}_2 \tilde{h}_2 - \tilde{m}_2 \bar{\tilde{h}}_2\right\} \qquad (4.3.4)$$

where subscripts 1 and 2 refer to the input and output variables at the break point, respectively. The discharge total head and mass flow rate fluctuations, $\tilde{h}_2$ and $\tilde{m}_2$, are related to the same quantities at inlet, $\tilde{h}_1$ and $\tilde{m}_1$, by the system transfer function, [S]. Substituting for $\tilde{h}_2$ and $\tilde{m}_2$ and equating the inlet and discharge mass flow rates ($\tilde{m}_2 = \tilde{m}_1$), results in the following expression for the net difference in energy fluxes.

$$\Delta \mathcal{E}_{osc} = \frac{|\tilde{h}_1|^2}{2} \text{ Real } \{\overline{\mathcal{F}(S)}\, \mathcal{G}(S)\} \tag{4.3.5}$$

where

$$\mathcal{F}(S) = \frac{S_{21}}{1-S_{22}}$$

and

$$\mathcal{G}(S) = \frac{1 - S_{22} - S_{11} + S_{11}S_{22} - S_{12}S_{21}}{1 - S_{22}} \quad .$$

Using the relations in Eq. (4.3.3), $\mathcal{F}(S)$ and $\mathcal{G}(S)$ become

$$\mathcal{F}(S) = \frac{\frac{2A}{U_T}\left(Z_{21} + j\Omega C(I_U Z_{21} - 1 - Z_{22})\right)}{(I_U + I_D)Z_{21} - Z_{22} + j\Omega C(I_U Z_{21} - 1 - Z_{22})} \tag{4.3.6}$$

and

$$\mathcal{G}(S) = Z_{11}Z_{22} - Z_{12}Z_{21} + (I_U + I_D)Z_{21} + j\Omega C\left(Z_{12} + I_U I_D Z_{21} - I_U(1+Z_{11}) - I_D(1+Z_{22})\right) \Big/ (I_U + I_D)Z_{21} - Z_{22} + j\Omega C(I_U Z_{21} - 1 - Z_{22})$$

It is known and shall be assumed that the compliance of the air bladder, C, is large. More specifically, it shall be assumed that

$$C >> |Z_{ij}| \quad ; \quad i,j = 1,2$$

and (4.3.7)

$$C >> |I_U| + |I_D| \quad .$$

The validity of this assumption is discussed in Appendix G. For large C, $\mathcal{F}(S)$ and $\mathcal{G}(S)$ reduce to

$$\mathcal{F}(S) \approx \frac{2A}{U_T} \tag{4.3.8}$$

and

$$\mathcal{G}(S) \approx \frac{-Z_{12} - I_U I_D Z_{21} + I_U(1+Z_{11}) + I_D(1+Z_{22})}{1 + Z_{22} - I_U Z_{21}}$$

The stability criterion is then given by

$$\Delta \mathcal{E}_{osc} = \frac{|\tilde{h}_1|^2}{2} \text{ Real} \left\{ \frac{I_U(1+Z_{11}) + I_D(1+Z_{22}) - Z_{12} - I_U I_D Z_{21}}{1 + Z_{22} - I_U Z_{21}} \right\} \tag{4.3.9}$$

If $\Delta \mathcal{E}_{osc} > 0$, energy is extracted from or dissipated in the system; and the system is stable. If $\Delta \mathcal{E}_{osc} < 0$, then an energy source (i.e. the inducer) exists within the system. The system must be considered unstable for this condition.

A look at the detailed structure of the stability criterion provides valuable insight. At high cavitation numbers, Z_{11}, Z_{21} and Z_{22} vanish. Stability is then determined by the sign of the quantity

$$\text{Real}\left\{I_U + I_D - Z_{12}\right\} \tag{4.3.10}$$

The quantity Real $\{-Z_{12}\}$ is the pump resistance. The quantity given in Eq. (4.3.10) therefore represents the total resistance of the system. If this is positive, the system will be stable. This is simply a requirement that the damping be non-negative for stability. This mechanism has been known to cause or identified as the cause of surging associated with axial flow compressors [18,26,27,44]. In addition, Stepanoff [51] indicates that unstable behavior of a pump can be associated with negative steady state pump resistances.

As the cavitation number is reduced, the compliance and dynamic pressure gain terms begin to influence the stability of the system.

The criterion expressed in Eq. (4.3.10) has wide application. It turns out [30] that in boiling two phase flows a hydrodynamic instability is generated due to buoyancy effects. The instability is characterized by oscillations within the flow. The condition for instability is that the slope of the hydrostatic head-flow rate curve becomes negative. This is equivalent to Eq. (4.3.10).

From the form of Eq. (4.3.9) it is evident that the stability of a hydraulic system depends upon the entire system and not just one component. It should be possible to suppress a system instability by an appropriate redesign or redistribution of the system impedances and/or compliances. This is in fact the method by which Rocketdyne [20,39] has attempted to suppress the oscillations within the feedlines to the Space Shuttle Main Engine. It is also clear that, given a hydraulic system whose resistance is positive, only the inducer itself has the capability of driving or exciting a system instability.

4.3.5 Stability Criterion Applied to the DPTF

The net difference in the energy flux into and out of the DPTF has been calculated using Eq. (4.3.9) for each experimentally obtained transfer function and all combinations of the inlet and discharge system impedances. These results cannot be used directly. During each transfer function test, the inducer operates into a system whose total steady state resistance is given by

$$\mathcal{R}_{SYS} = \frac{2\Psi}{\varphi} \quad . \tag{4.3.11}$$

An interpolation procedure is necessary to match the system impedance combinations to the transfer function of the inducer. Otherwise, an

energy source or sink is arbitrarily being inserted into the system.

The variation in the stability of the system resulting from a redistribution of the system impedances, I_U and I_D, is demonstrated in Fig. 4.10. The transfer function of IMP4 operating at $\varphi = 0.070$ and $\sigma = 0.040$ was used to create Fig. 4.10. Each curve in this figure represents a different combination of the inlet and discharge system impedances. The fact that each of these curves is different reconfirms that auto-oscillation is a function of the entire hydraulic system. The trends indicated in this figure are typical of both IMP4 and IMP6 operating at all cavitation numbers. It can also be concluded that the system is least stable at the higher frequencies for this particular cavitation number.

Selecting one combination of matched system impedances, the effects of the increased active character of the inducer with a reduction in cavitation number are illustrated in Fig. 4.11 for IMP4 operating at 9000 RPM. Several conclusions can be drawn from this figure. The hydraulic system, or more accurately the model of the DPTF, becomes more and more unstable as the cavitation number is decreased. This feature is entirely consistent with the discussion concerning the increased activity of the inducer. It should also be noted that the predicted frequency of minimum stability agrees with the observed range of auto-oscillation frequencies of 28-35 Hz. The frequency of minimum instability is predicted to decrease monotonically with cavitation number. Although data have not yet been presented to substantiate this result, auto-oscillation frequency data will be presented in the next chapter which will confirm this prediction. Finally, there appears to be a trend towards increased stability at low frequencies. In addition,

the cavitation numbers for which auto-oscillation is predicted to occur agree with the experimental observations presented in Fig. 3.6.

Several transfer functions of IMP4 were obtained at 12000 RPM. The stability plot for these transfer functions appears in Fig. 4.12. These curves are not unlike those of the 9000 RPM transfer functions (Fig. 4.11). The non-dimensional frequency of minimum stability remains unchanged. Again, frequency shift with cavitation number is observed. Similar results for IMP6 have been obtained and are presented in Fig. 4.13. The enhanced stability of IMP6 compared to IMP4 corresponds to the less active character of IMP6.

The decreased stability of the DPTF is a direct result of the increased activity or changes in the dynamic characteristics of the inducer caused by cavitation. It has not yet been determined which of the elements of the transfer function have the greatest effect on the stability of the system. This question is addressed in Section 4.3.6.

4.3.6 Sensitivity of the Stability Criterion to the Elements of the [Z] Matrix

Other than the results of [10,11,16,22,41,43], little is quantitatively known about the actual dynamics (i.e. transfer functions) of the turbomachines. Hence, knowledge of the sensitivity of the DPTF to the various dynamic parameters of the transfer function of the inducer is of interest. This sensitivity check was accomplished by creating a hypothetical transfer function by combining elements from a non-cavitating ($\sigma = 0.508$) and a cavitating ($\sigma = 0.024$) transfer function of IMP4. The stability of the system to all possible permutations of the elements of these two transfer functions was determined by use of equation (4.3.9) for one combination of system impedances. The results of these

calculations are presented in Figs. 4.14. Also included in that figure are the results of a similar set of calculations in which the sensitivity to the phase of each element of the transfer function was investigated. In this second set of calculations, the transfer function was assumed to take the following form:

$$\begin{bmatrix} |Z_{11}| & Z_{12} \\ -j|Z_{21}| & -j|Z_{22}| \end{bmatrix} \quad . \tag{4.3.12}$$

In each of the four graphs in Fig. 4.14, the net difference in the energy flux into and out of the system for both the non-cavitating and the cavitating transfer function alone are plotted. The other two curves correspond to the effects on the stability of the DPTF caused by cavitation induced dynamics of that particular element of the transfer function. Consider the two graphs on the left hand side of Fig. 4.14. Neither the dynamic pressure gain nor the compliance terms appreciably affect the stability of the DPTF. The impedance of the inducer, however, does measureably affect the stability of the system. The reduction in the pump resistance and changes in the inertance of the pump at low cavitation numbers adversely affect the stability of the system. The stability of the DPTF is most sensitive, however, to the mass flow gain factor, Z_{22}, as indicated in the lower right hand graph in Fig. 4.14. In all of these four graphs, the phase shifts found in the experimental transfer functions are a destabilizing feature of the pump dynamics.

It is apparent from the above results that an accurate estimate not only of the amplitude but of the phase of the pump impedance and

mass flow gain factor is necessary to adequately model the dynamics of a cavitating inducer.

4.3.7 Discussion of Linear Stability Analysis

The above linear stability analysis is seen to be remarkably successful. The analysis correctly predicts both the cavitation numbers for which the system is unstable and the correct frequency range of auto-oscillation. In addition, the stability analysis suggests a decrease in the auto-oscillation frequency with cavitation number. This feature, as well, will be confirmed in the next chapter. Unfortunately, the variations with flow coefficient could not be investigated because of difficulty in obtaining transfer functions at other flow coefficients.

Of greater importance, however, is the idea that auto-oscillation is a function of the entire hydraulic system. As a consequence, the stability of the system can be altered by appropriately redesigning the system. Alternately, the stability of the system can be improved by changing the mean operating state of the inducer. In order to reduce the capability of the inducer to supply energy to the flow, it is necessary to increase the cavitation number. The fact that the activity can be attributed to the presence of cavitation within the inducer strongly suggests that other phase change processes must be similarly active. Brennen [11] has demonstrated that phase change interfaces such as those found in the pressure suppression systems of Boiling Water Reactors (BWR) are active. The dynamics of these interfaces can excite a system resonance [13]. Consequently, hydraulic systems containing a phase change may exhibit similar instabilities.

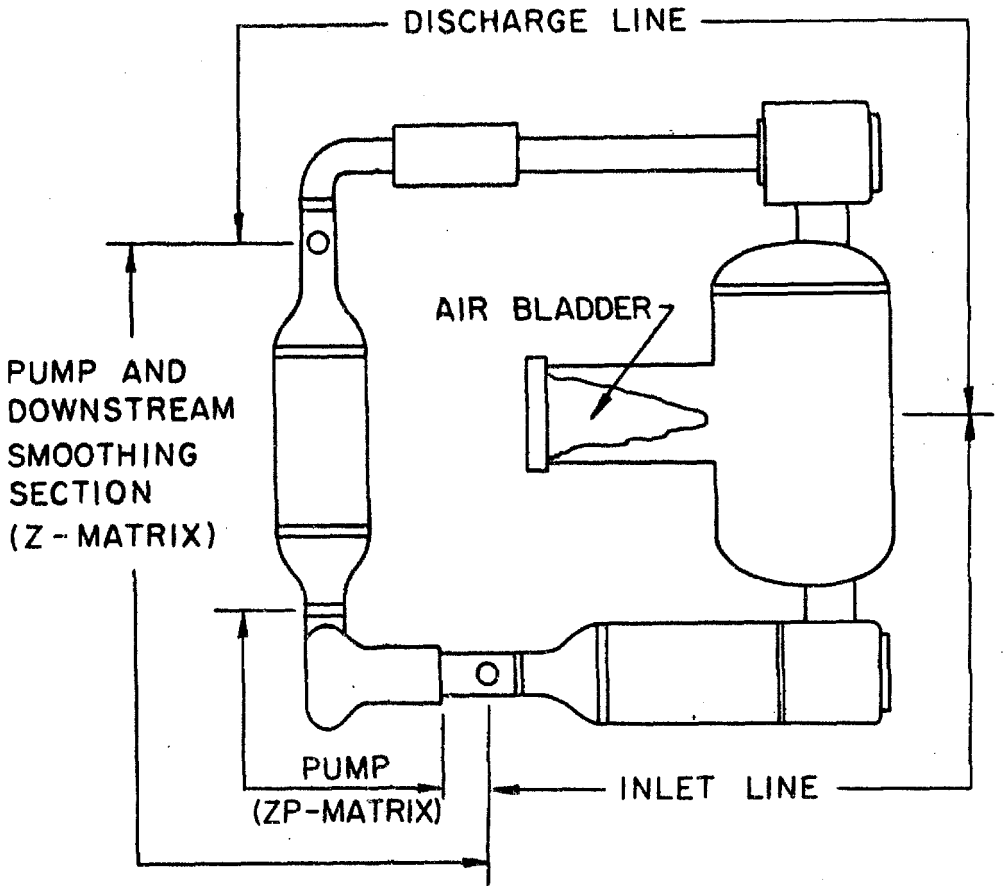

Fig. 4.1 Schematic of the Dynamic Pump Test Facility indicating the system components to be modeled for the linear stability analysis.

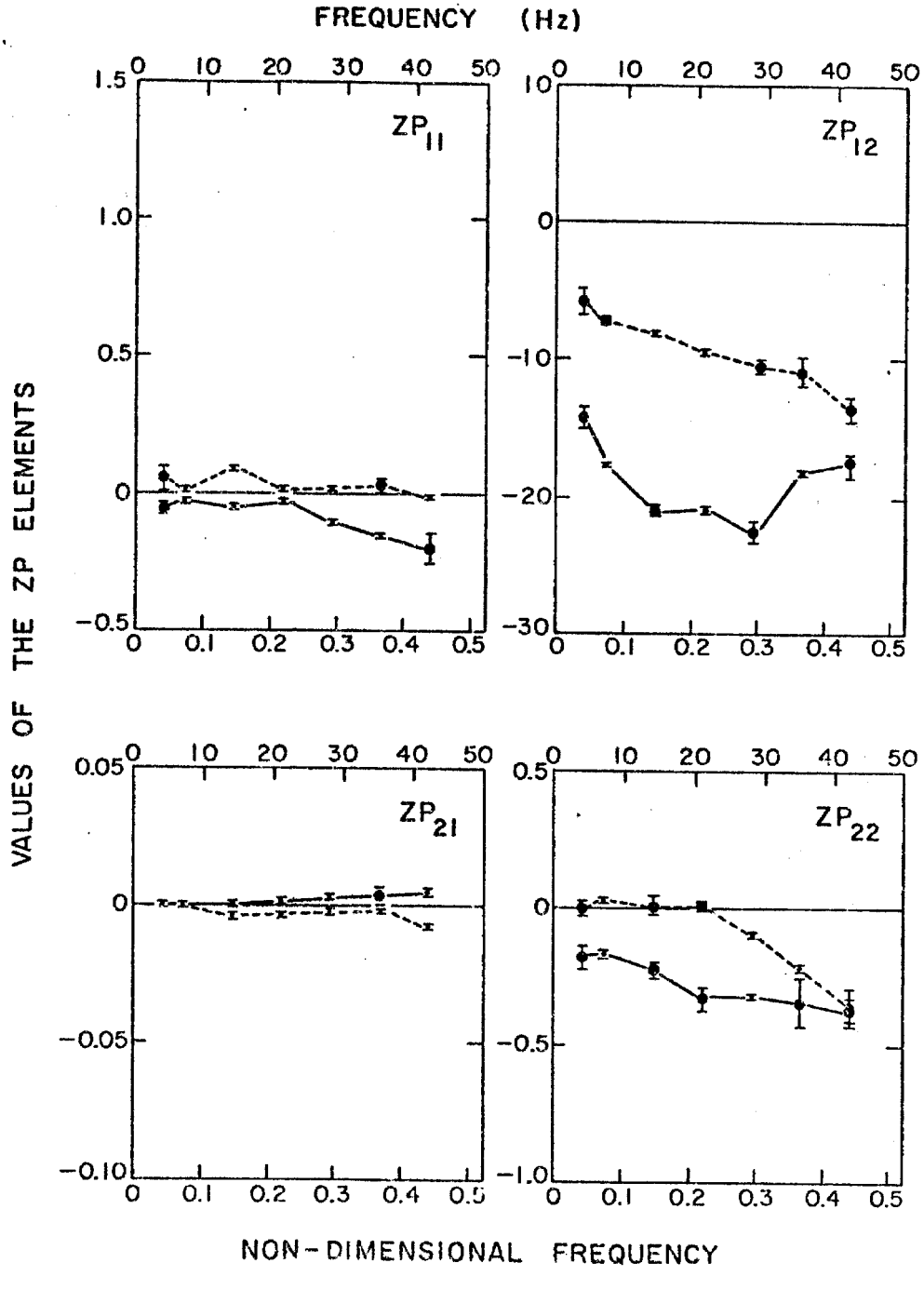

Fig. 4.2 [ZP] transfer function of Impeller 4 operating at $\varphi = 0.070$, $\sigma = 0.51$ and 9000 RPM (point A in Fig. 3.6). The real and imaginary parts of the elements (solid and dashed lines respectively) are plotted against both the actual and non-dimensional frequencies.

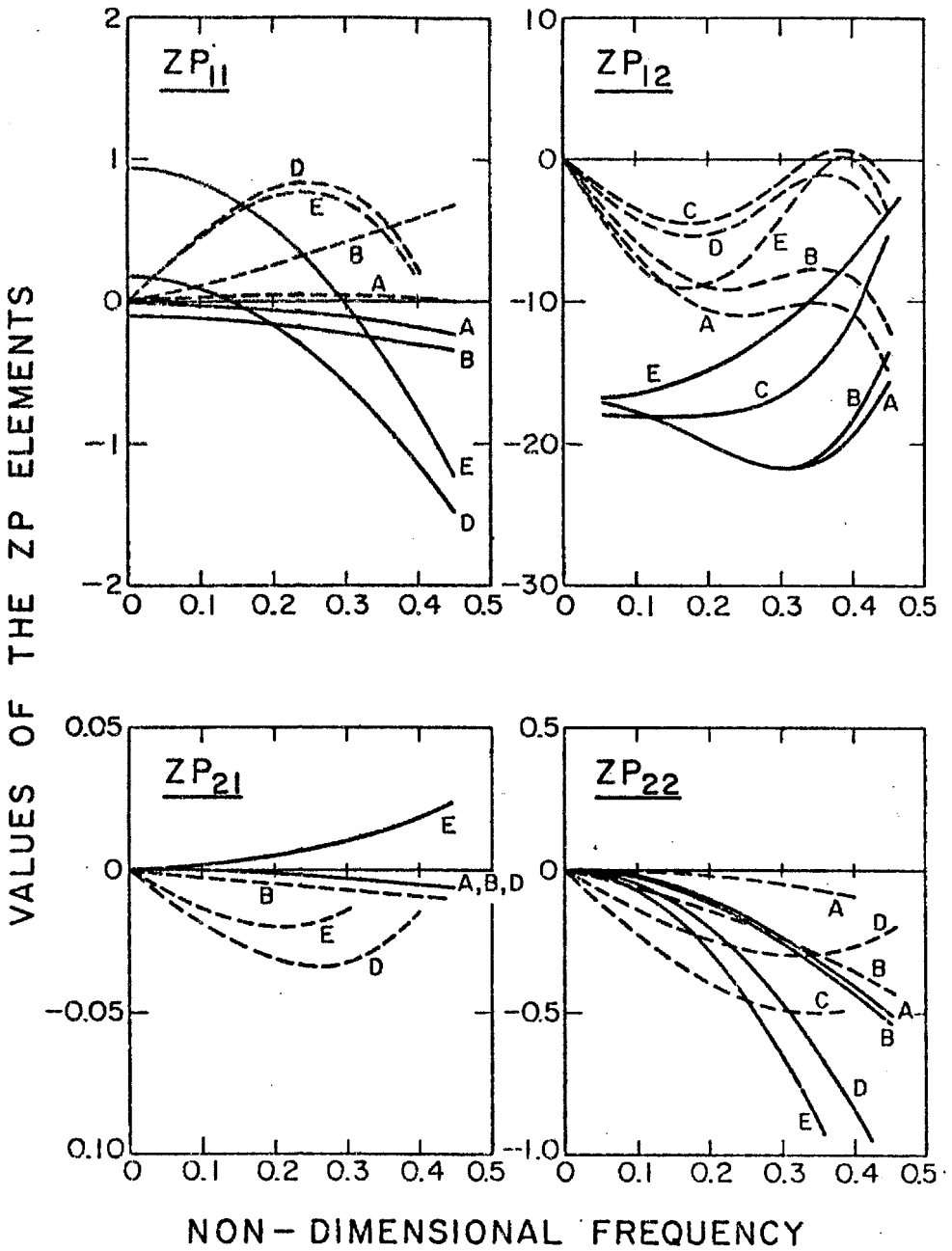

Fig. 4.3 Polynomial curve fit [ZP] transfer functions of Impeller 4 operating at $\varphi = 0.070$ and 9000 RPM. The real and imaginary parts (solid and dashed lines respectively) are plotted as funct ons of non-dimensional frequency. The letters correspond to those in Fig. 3.6 and indicate cavitation numbers of (A) 0.508, (B) 0.114, (C) 0.046, (D) 0.040, (E) 0.024.

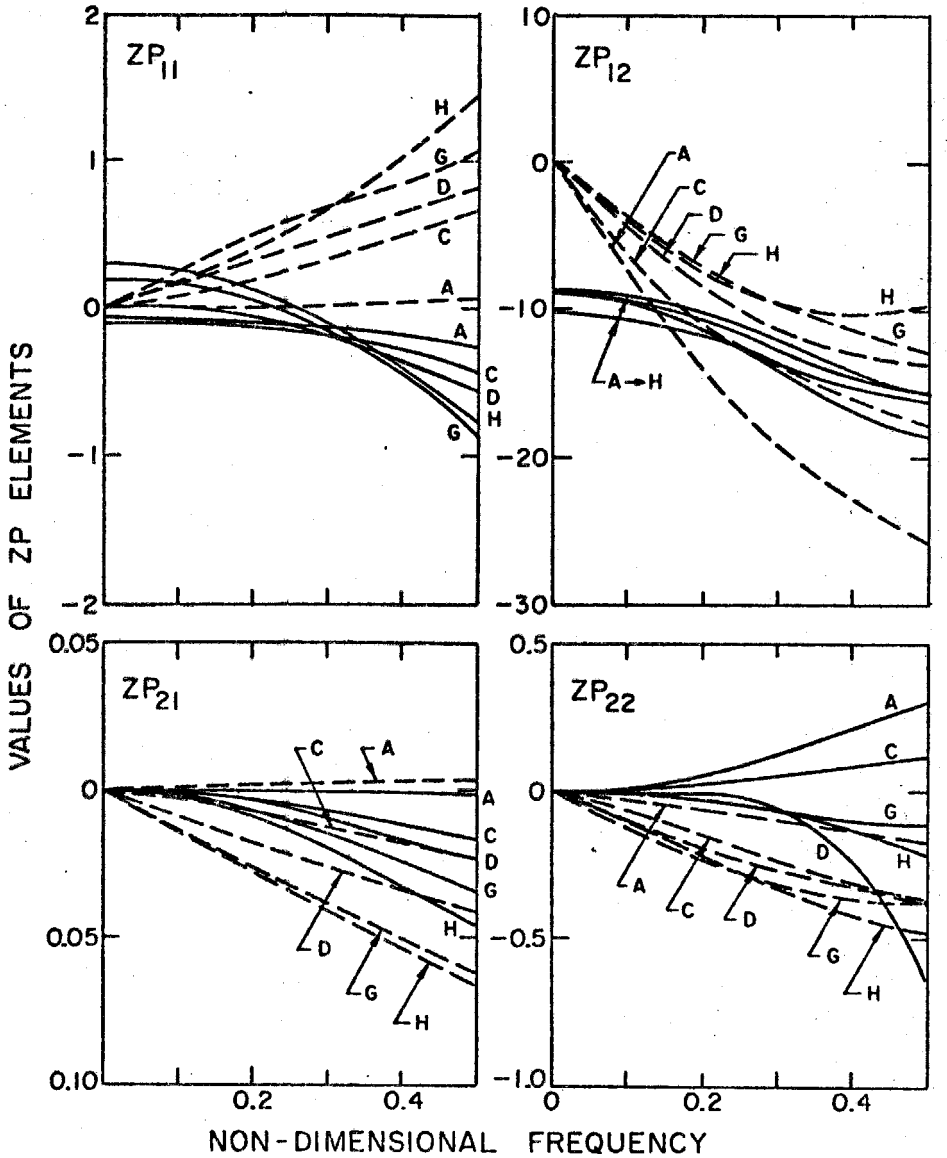

Fig. 4.4 Polynomial curve fit [ZP] transfer functions of Impeller 6 operating with an inlet flow straightener at $\varphi = 0.070$ and 6000 RPM. The real and imaginary parts (solid and dashed lines respectively) are plotted as functions of non-dimensional frequency. The letters correspond to those in Fig. 3.7 and indicate cavitation numbers of (A) 0.366, (C) 0.100, (D) 0.068, (G) 0.052, (H) 0.044.

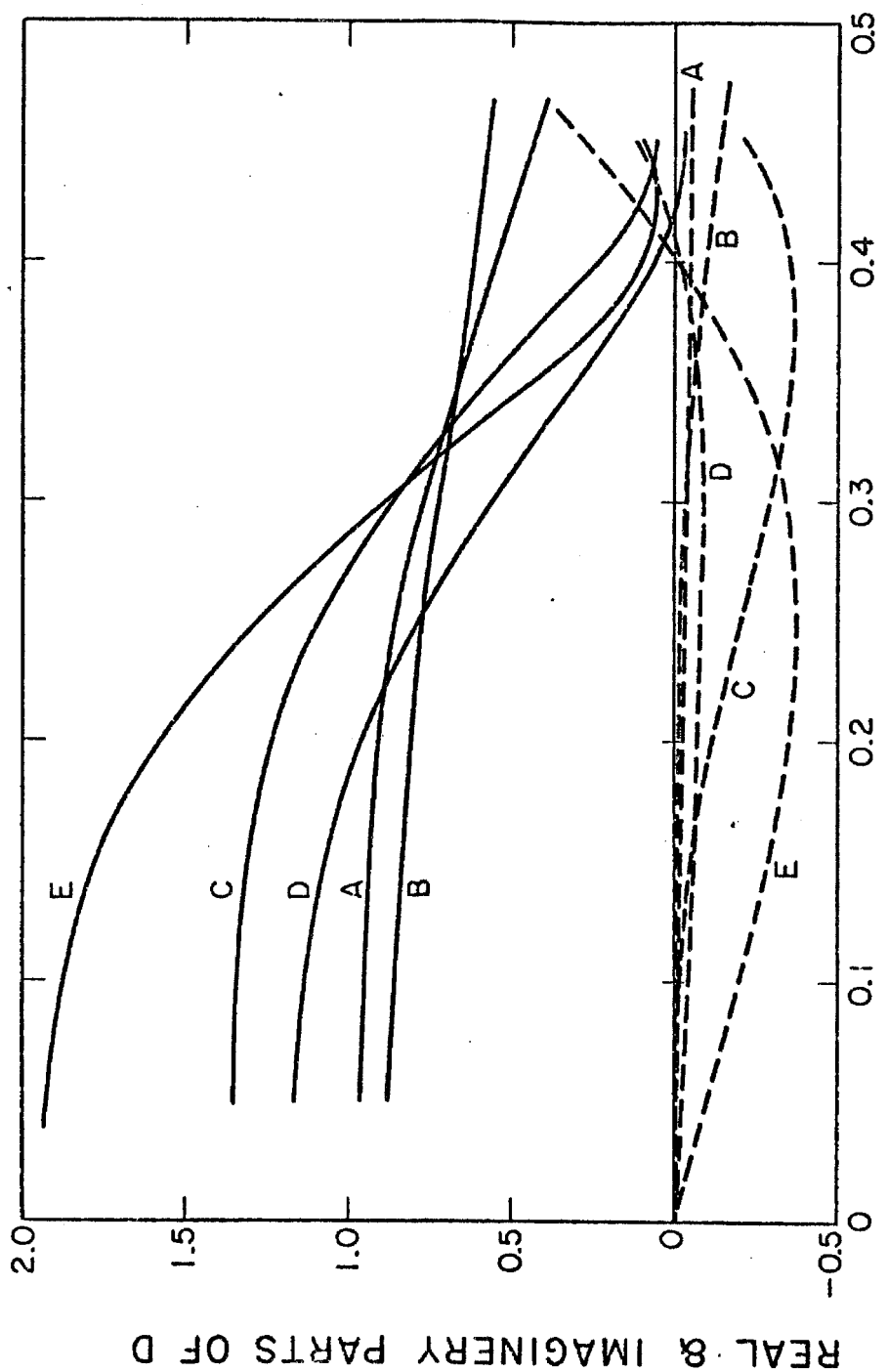

Fig. 4.5 Determinant of curve fit [ZP] matrices presented in Fig. 4.3 of Impeller 4 operating at $\varphi = 0.070$ and 9000 RPM. The real and imaginary parts (solid and dashed lines) are plotted as functions of non-dimensional frequency.

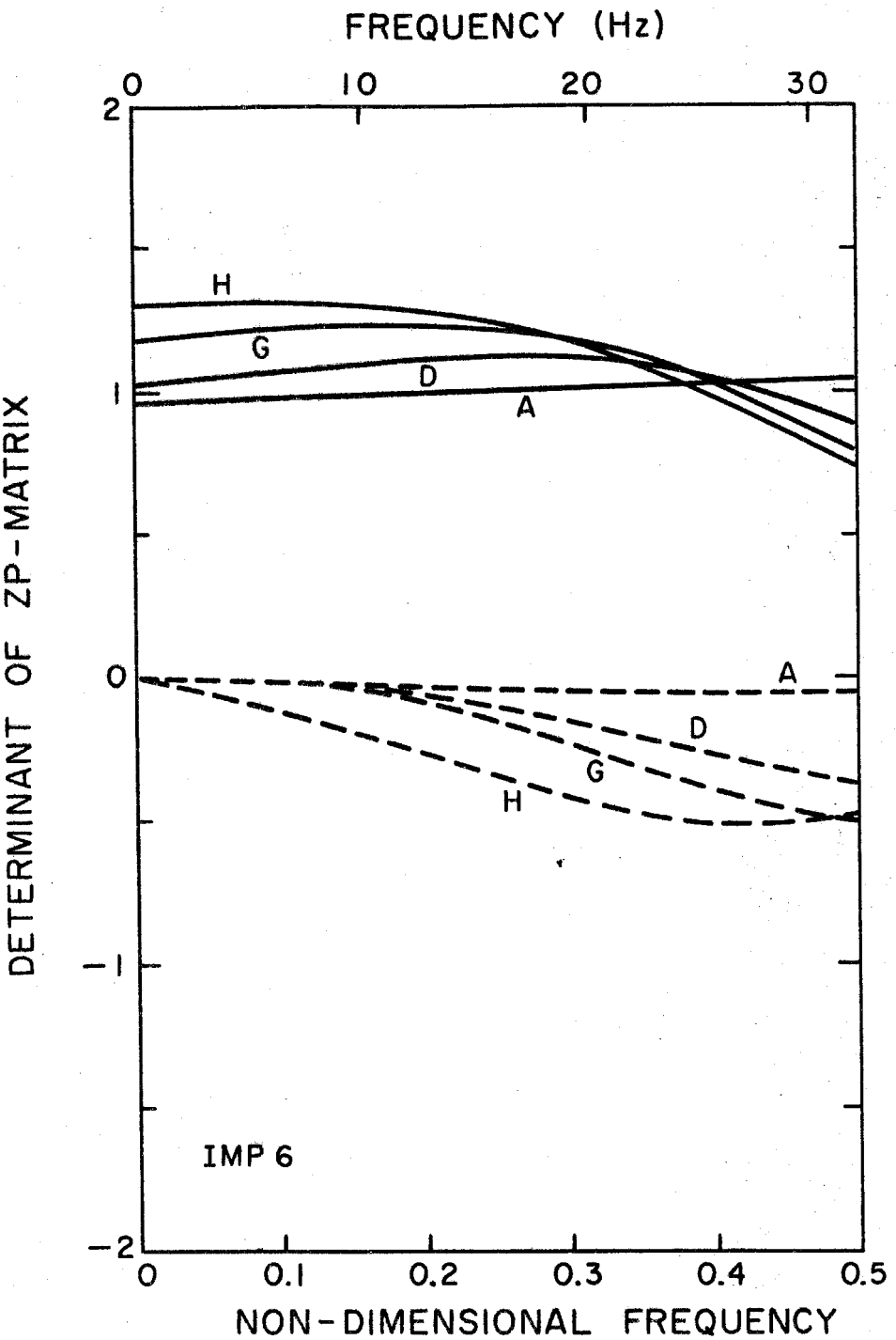

Fig. 4.6 Determinant of curve fit [ZP] matrices presented in Fig. 4.4 for Impeller 6 operating at $\varphi = 0.070$ and 6000 RPM. The real and imaginary parts (solid and dashed lines) are plotted against the non-dimensional frequency.

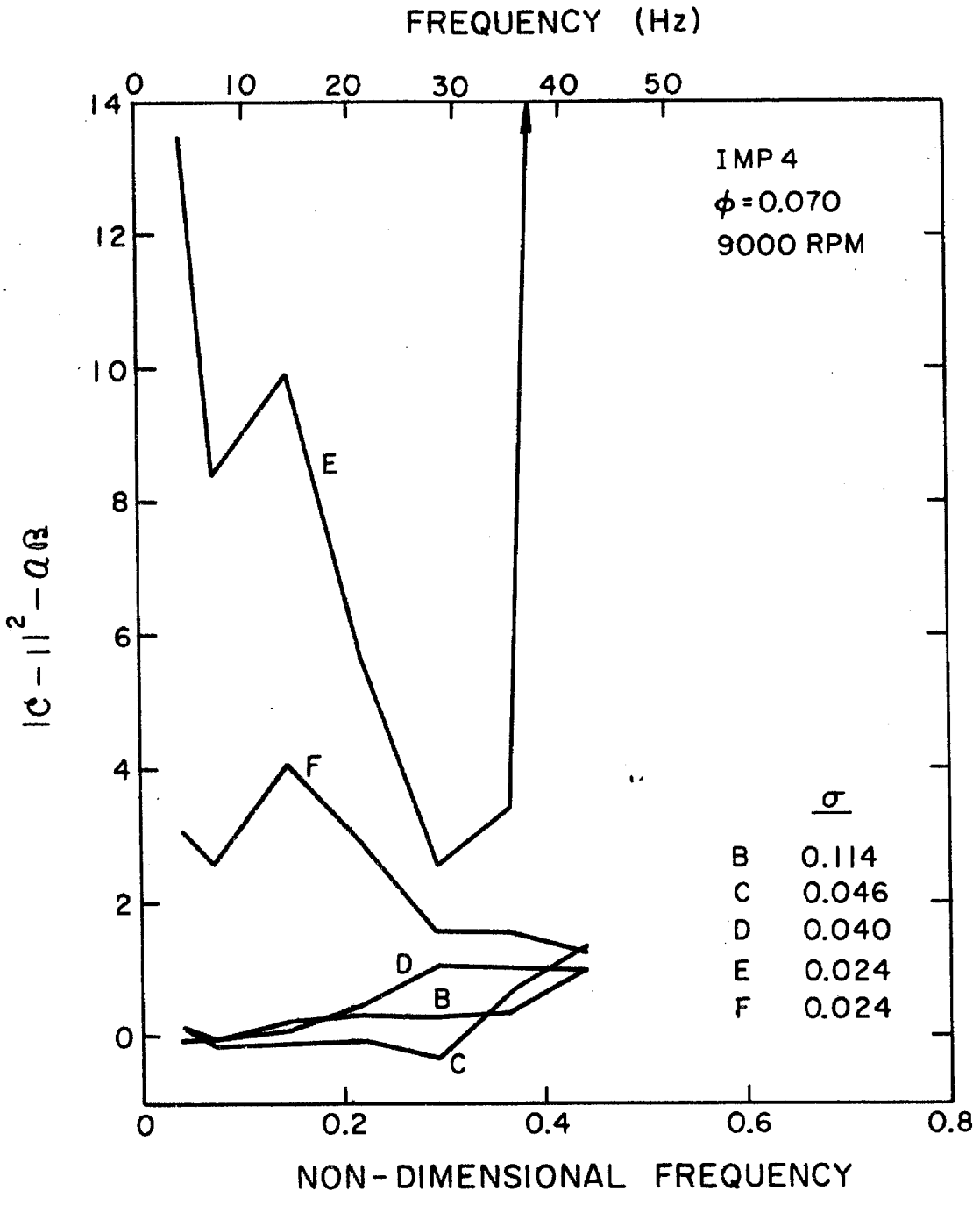

Fig. 4.7 The activity parameters for Impeller 4 transfer functions. Positive values of this parameter indicate that Impeller 4 is an active device.

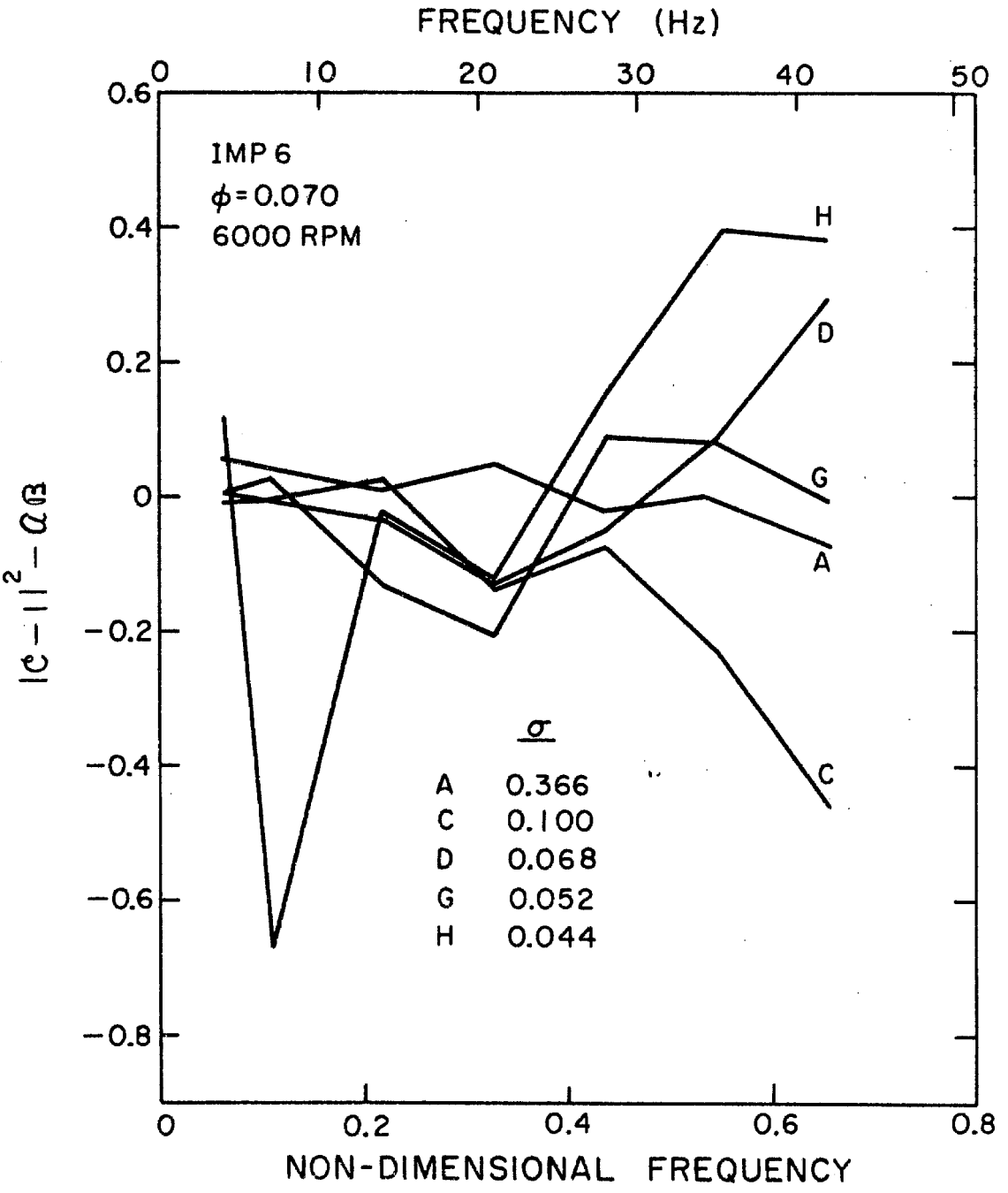

Fig. 4.8 The activity parameter for Impeller 6 transfer functions. Positive values of this parameter indicate that Impeller 6 is an active device.

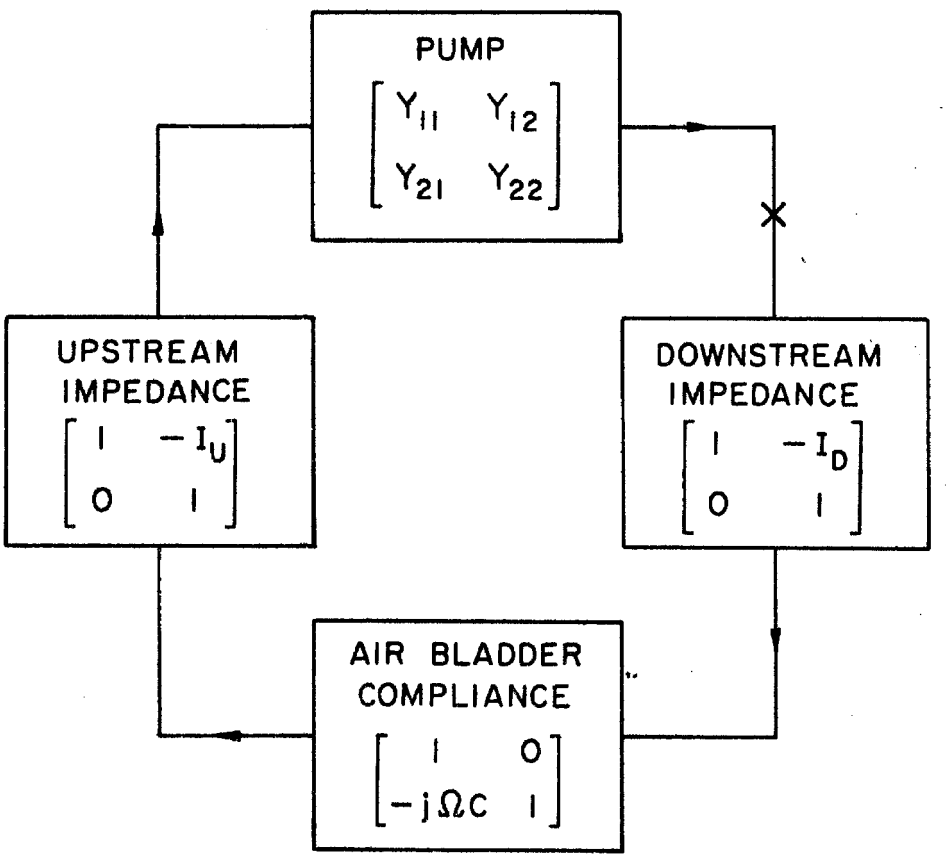

Fig. 4.9 Model of the dynamic properties of the Dynamic Pump Test Facility.

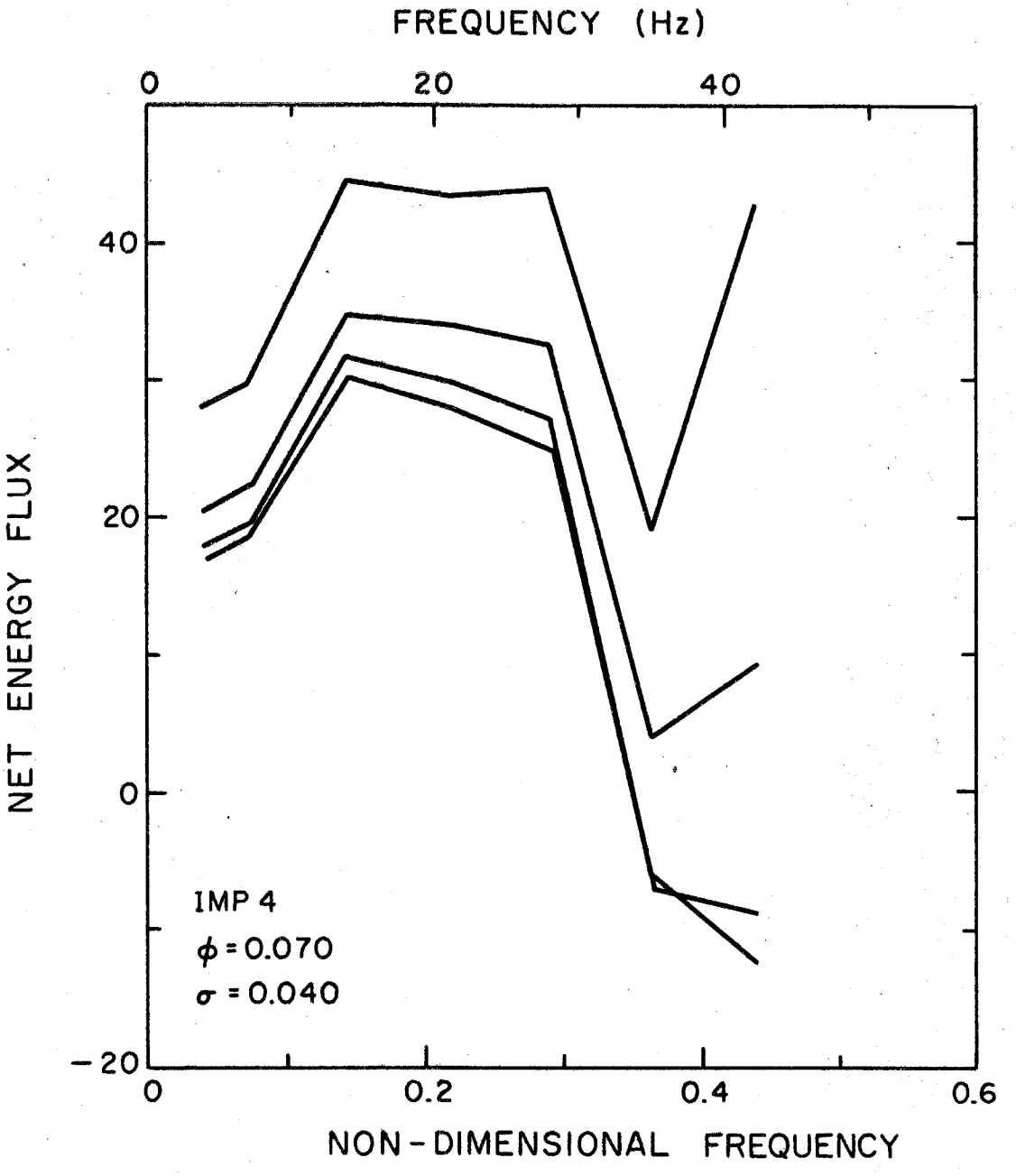

Fig. 4.10 Net flux of energy delivered to DPTF during operation of Impeller 4 at $\varphi = 0.070$ and $\sigma = 0.040$. Positive values indicate stable operation of the system. Each curve corresponds to a different combination of system impedances.

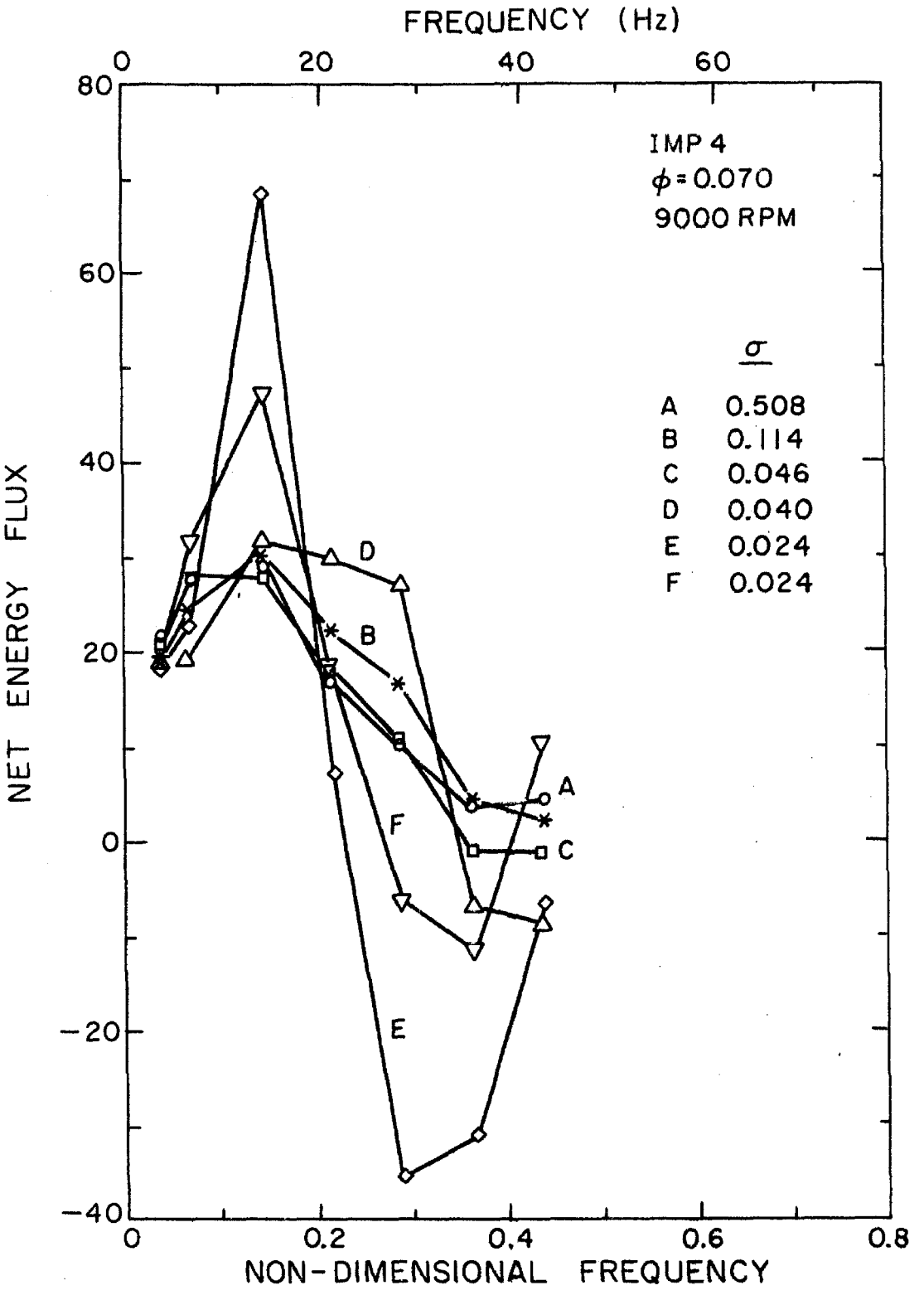

Fig. 4.11 Net flux of energy delivered to DPTF for one specific combination of system impedances and the 9000 RPM, φ = 0.070 Impeller 4 transfer functions. Positive values indicate stable operation of the system.

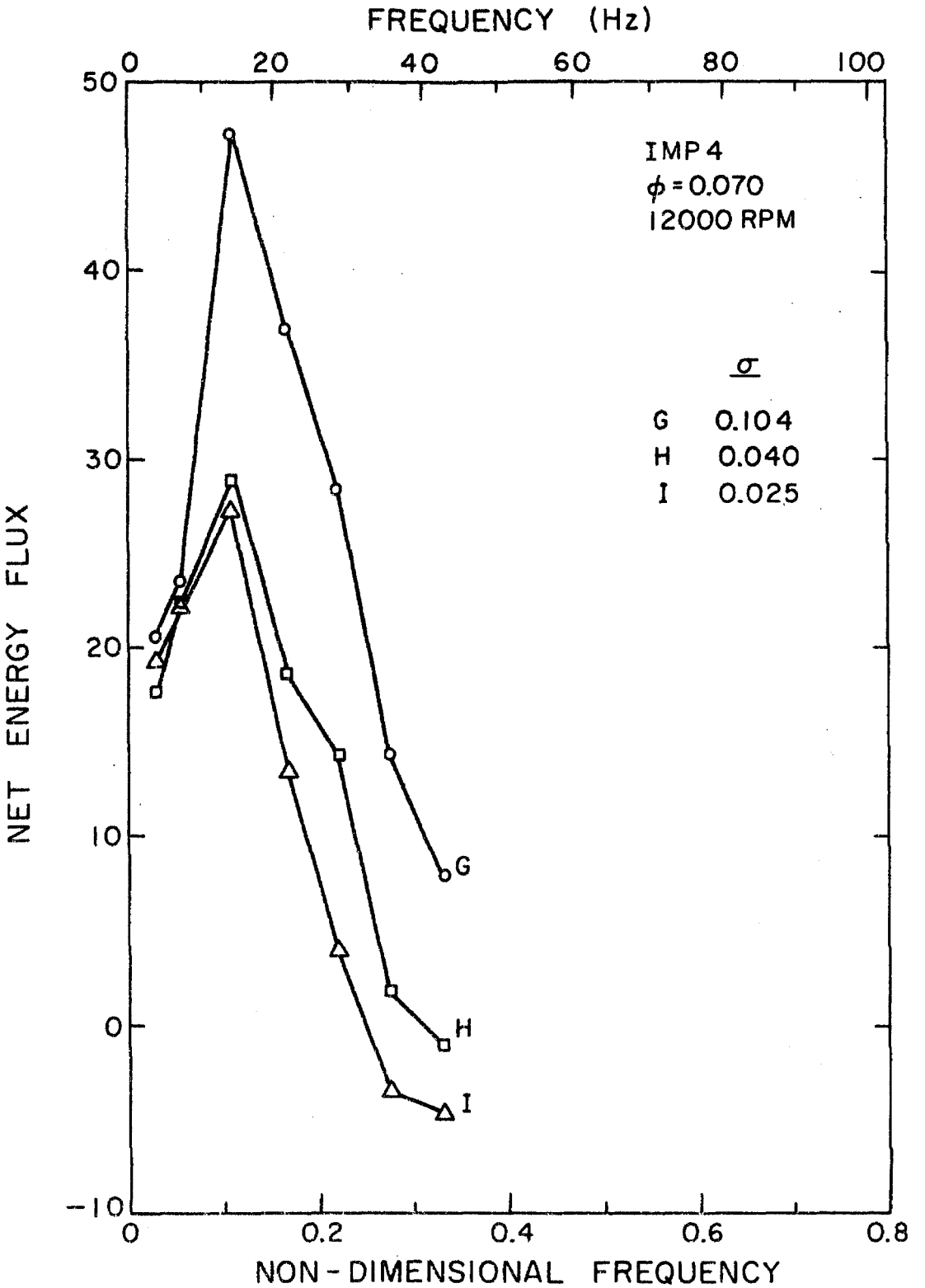

Fig. 4.12 Net flux of energy delivered to DPTF given one combination of system impedances and the 12000 RPM, $\varphi = 0.070$ Impeller 4 transfer functions. Positive values indicate stable operation of the system.

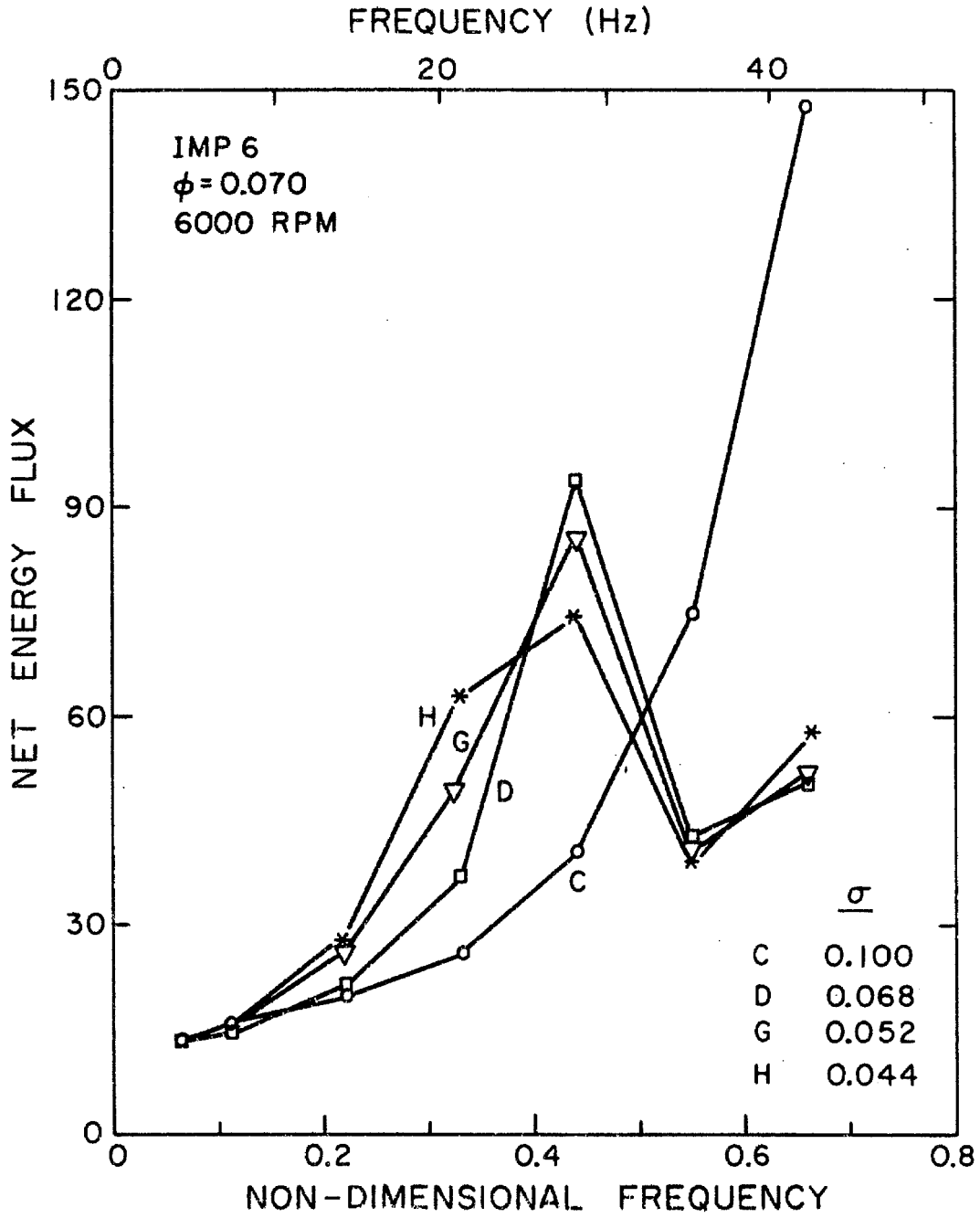

Fig. 4.13 Net flux of energy delivered to DPTF given one combination of system impedances and the 6000 RPM, $\varphi = 0.070$ Impeller 6 transfer functions. Positive values indicate stable operation of the system.

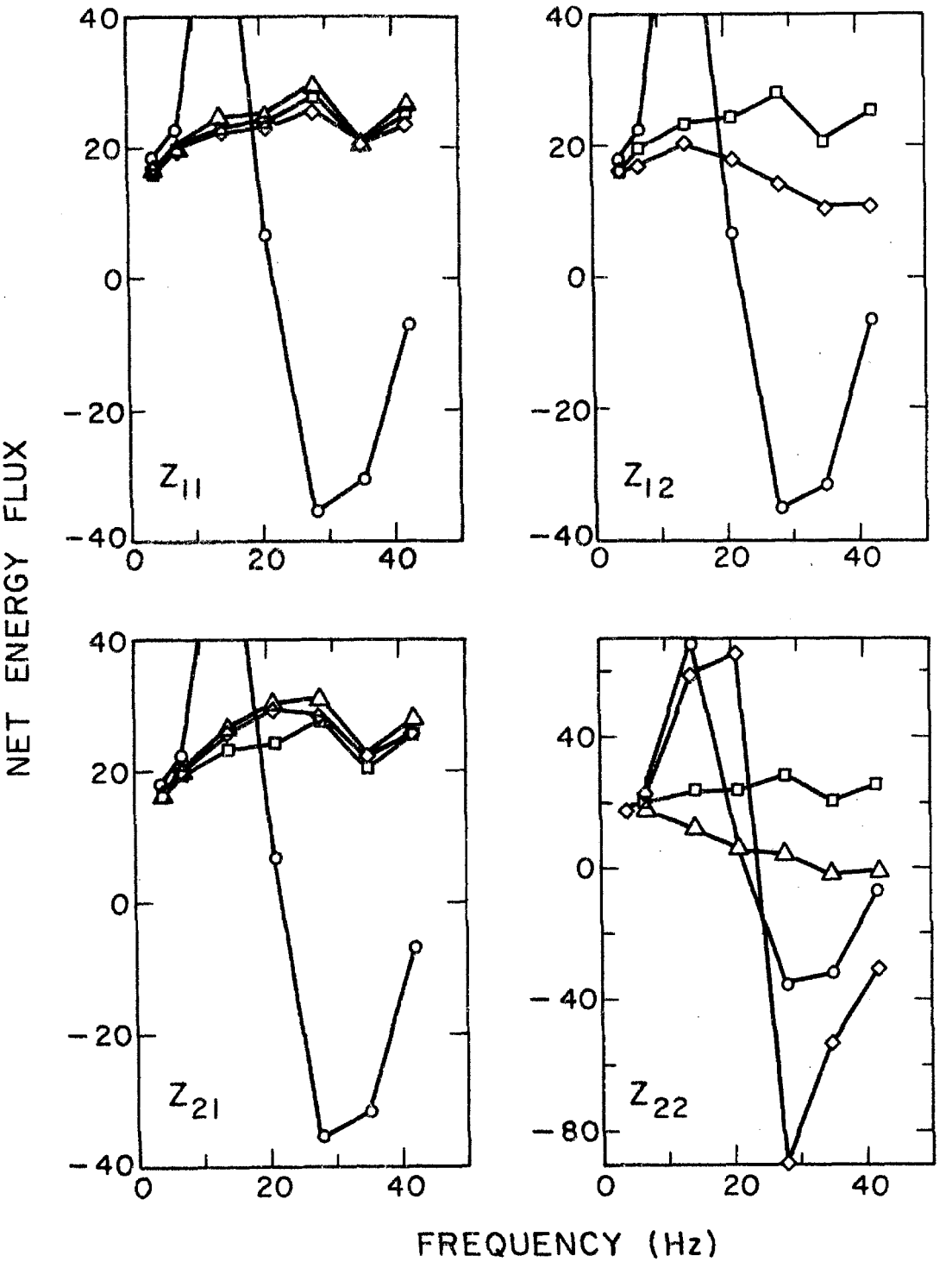

Fig. 4.14 Sensitivity of net energy flux delivered to DPTF to the individual parameters of the pump transfer function. The (□) and (○) curves represent the $\varphi = 0.070$, 9000 RPM Impeller 4 transfer functions at $\sigma = 0.508$ and $\sigma = 0.024$, respectively. The (◇) curves were created by separately replacing each element of the $\sigma = 0.508$ transfer function by its cavitating value. This modified [Z] matrix was then phase shifted according to Eq. (4.6.1) to obtain the (△) curves.

V. DETAILED AUTO-OSCILLATION MEASUREMENTS

5.1 Introduction

IMP6 was used in an additional series of experiments to obtain a more detailed and complete set of data on auto-oscillation. The effects of variations in flow coefficient, cavitation number and inducer rotational speed were investigated. The measurements consist of frequencies, amplitudes and phase angles of several pressures and mass flow rates around the system. The location of these measurements has been described in Chapter 2.

5.2 Auto-Oscillation Frequency Data

The frequencies, ω, of auto-oscillation will be presented in terms of non-dimensional frequency, Ω. The non-dimensional frequency is defined by Eq. (5.2.1).

$$\Omega = \frac{\omega \aleph}{U_T} \tag{5.2.1}$$

where

$\aleph$ = blade tip spacing = $2\pi R$/ number of blades

R = radius of the inducer.

The dominant frequencies in the pressure fluctuations at the inlet to IMP6 are presented in Fig. 5.1. The 535 Hz frequency at high cavitation numbers corresponds to the pressure fluctuations at twice the blade passage frequency. At lower cavitation numbers, the blade passage frequency, ω = 267 Hz, dominates the pressure spectra. The amplitude of the blade passage frequencies decreases axially away from the inducer. These pressure fluctuations appear to be confined to the tip clearance flow. The 20 Hz frequency at still

lower cavitation numbers indicates the region of auto-oscillation. During auto-oscillation, the low frequency oscillations completely obscure the blade passage effects. This figure shows that the auto-oscillation frequencies are much (i.e. in order of magnitude) smaller than the blade passage frequencies. Hence, it is unlikely that these internal hydrodynamic forcing frequencies are related to auto-oscillation.

The auto-oscillation frequency depends upon several parameters as indicated in Fig. 5.2 for IMP6. The parameters of importance are the mean flow rate through the pump, the cavitation number and the tip speed of the inducer. The large variation with flow coefficient suggests that the detailed structure of the inlet flow field is one of the controlling features of the instability. Referring to Figs. 3.2 and 3.4, a reduction in the auto-oscillation frequency is produced by an increase in the strength of the backflow jet and prerotation of the inlet flow. A section of honeycomb was inserted one diameter upstream of the inducer in order to investigate this further. The effect of the honeycomb was to "straighten" out the inlet flow by reducing the amount of backflow induced prerotation. This effect was particularly pronounced at the lower flow coefficients. This straightening of the inlet flow by the honeycomb is documented in Figs. 5.3 and 5.4. From these figures, it is apparent that the honeycomb produces a reduction in the swirl velocity. Two experiments were then performed on IMP7. In the first, the honeycomb was not inserted. Data on the auto-oscillation occurring at a flow coefficient of $\varphi = 0.067$ were obtained. Subsequently, the honeycomb section was installed; and data taken for the identical mean flow conditions. As expected, Fig. 5.5 shows that straightening the inlet flow resulted in higher auto-oscillation frequencies even

though the flow coefficient was held fixed. The performance with the honeycomb installed was thus equivalent to the performance at a higher flow coefficient.

The auto-oscillation frequency is also a function of the cavitation number. A decrease in the frequency occurs simultaneously with a decrease in cavitation number. This frequency reduction is physically related to the amount of cavitation occurring within the inducer. Since the dynamic behavior of the inducer is determined by the cavitation, this shift in the auto-oscillation frequency is direct evidence of a change in the dynamic characteristics of the inducer. These experimental measurements provide confirmation of the trend for a frequency reduction with cavitation number that was predicted by the results of the linear stability analysis in Section 4.3.5. The identical trend has been reported in Refs. [5, 38, 40, 56]. Acosta and Wade [4] have also reported observing a decrease in frequency corresponding to a decrease in cavitation number for cavitating hydrofoils in cascade.

Finally, the auto-oscillation frequency depends upon the tip speed of the inducer, U_T. In Fig. 5.2, data obtained at 4000 RPM are given by the dashed curves. Since the curves for the flow coefficient of 0.070 are very close, this indicates that Eq. 5.2.1 represents the correct scaling relationship. This scaling relationship was further investigated over a larger range of tip speeds. IMP7 was used for this test. A cavitation number for which auto-oscillation occurred at a flow coefficient of 0.055 was selected. The rotational speed, RPM was then varied while maintaining the chosen flow coefficient and cavitation number. The results of this experiment are presented in

Fig. 5.6. The results demonstrate that the scaling of the auto-oscillation frequency with tip speed is correct.

The observed auto-oscillation frequencies for IMP4 were generally smaller than the corresponding frequencies excited by IMP6. This difference can be attributed in part to changes in the system parameters caused by the system redesign. In addition, variations in the performance between these inducers contribute to the above differences.

5.3 Amplitude Data

The pressure and mass flow rate fluctuations at high cavitation numbers are random with a broad frequency spectrum and have small amplitudes except in the neighborhood of the inducer, as indicated in Fig. 5.1. These low level, random fluctuations do not become organized into a single dominant frequency until the system becomes unstable. The onset of auto-oscillation is quite dramatic, as indicated in Fig. 5.7. In that figure, the non-dimensional pressure and mass flow rate fluctuation amplitudes have been plotted against cavitation number for a flow coefficient of 0.070. These data were obtained on IMP6 at 6000 RPM. The amplitudes of the pressure fluctuations have been non-dimensionalized by ρU_T^2 and the mass flow rates by $\rho A_I U_T$. At cavitation numbers greater than 0.051, the amplitude of the fluctuations are vanishingly small. At a cavitation number of 0.047, a large jump in amplitude occurs. The amplitude remains high down to a cavitation number of 0.02 at which point the system becomes stable once more. The region of auto-oscillation or system instability is thus readily defined. In Fig. 5.8, amplitude data taken at 4000 RPM on IMP6 for $\varphi = 0.070$ are presented. It is apparent

that the non-dimensional amplitudes of the various quantities are smaller that those of the 6000 RPM data. In addition, the onset cavitation number 0.039 is significantly less than 0.047 at 6000 RPM. This is evidence of a system effect. The dynamic characteristics of the system do not scale with the tip speed of the inducer. Hence, such differences should be expected.

The regions of auto-oscillation at flow coefficients of 0.075, 0.065 and 0.055 are given Figs. 5.9-5.11. These data were obtained at 6000 RPM. The general characteristics of auto-oscillation at these flow coefficients are identical to those at $\varphi = 0.070$. In each of these figures, the amplitude of the downstream pressure and mass flow rate fluctuations are greater than those far upstream of the inducer. The amplitude of the pressure fluctuations near the inlet plane of IMP6 are comparable to the amplitude of the downstream pressure fluctuations. This correspondence is to be expected. The pressure transducers near the inlet plane are located in the housing of the inducer and are exposed to the tip clearance flow. The tip clearance flow responds directly to the pressure rise across the inducer blading as described in Section 3.3. Hence, the pressure fluctuations measured at the inlet should resemble those downstream of the inducer. However, this explanation does not completely account for the large amplitude of the pressure fluctuations at an axial location of 0.5 radii upstream of the inlet plane of IMP6. Referring to Figs. 3.2 and 3.4, the axial and swirl velocity profiles indicate that the steady state backflow jet does not penetrate to this axial location for the flow coefficients of 0.070 and 0.075. The upstream mass flow rate oscillations during auto-oscillation at these flow coefficients are not sufficiently great to reduce

the instantaneous flow coefficient to less than 0.067. At flow coefficients less than 0.067, a reversed flow region is observed 0.5 radii upstream of IMP6. The above considerations strongly suggest that the dynamics of the inlet flow field are an important and perhaps controlling factor in auto-oscillation.

Replotting the auto-oscillation amplitudes of the downstream pressure fluctuations against cavitation number for the four flow coefficients provides additional insight (Fig. 5.12). Clearly, the range of cavitation numbers for which the system exhibits an auto-oscillation varies with flow coefficient. It is interesting to note that the auto-oscillation occurred over a wider range of cavitation numbers at the design flow coefficient of 0.070. Also, the maximum amplitude of auto-oscillation tends to increase with a decrease in flow coefficient. This general trend was also observed at 4000 RPM on IMP6. This trend for larger amplitudes at the lower flow rates has been mentioned several times in the literature [21, 34, 38, 49, 50, 56]. In addition, Acosta and Wade [4] have documented a similar behavior for cavitating cascades of hydrofoils. When the angle of attack is increased, the amplitude of the instability increases. An angle of attack increase is equivalent to a decrease in the flow coefficient for an inducer and, in addition, results in a larger cavity volume. The above variations with flow coefficient are related to or result from the inlet velocity profiles and cavitation. As indicated before, these two effects are coupled and directly influence the dynamic characteristics of the inducer.

5.4 Phase Relationships

The relative phases of the dynamic measurements with respect

to the upstream mass flow rate fluctuations follow trends similar to those of the amplitude data. The relative phase angles corresponding to the amplitude data presented in Figs. 5.7 and 5.9-5.11 appear in Fig. 5.13. Again, the phase of the pressure fluctuations in the neighborhood of the inlet plane of IMP6 is more closely related to the downstream pressure fluctuations than to the far upstream pressure fluctuations. In Fig. 5.13, the relative phase angle of all quantities is a continuous function of the cavitation number. This variation with cavitation number is another manifestation of the changes in the dynamic characteristics of the inducer accruing from the existence of cavitation within the inducer. In addition, a reasonably smooth variation with flow coefficient is also evident.

The relative phase angle data also indicate that the dynamics of the inlet flow field contribute significantly to auto-oscillation.

5.5 Indications of Nonlinear Effects

The auto-oscillation measurements described above are not sufficient to distinguish whether auto-oscillation is a nonlinear limit cycle oscillation or the response of a very lightly damped linear system. The large jump in the amplitude of the various field quantities as the region of instability is entered is indicative of a jump resonance. However, lightly damped linear systems exhibit a similar rapid increase in amplification. In either case, the frequency reduction corresponding to a decrease in cavitation number (Fig. 5.2) indicates that the DPTF is a softening system. This softening could be attributed to the increasing "compliance" in the pump.

A series of experiments with IMP8 provides further insight.

Initially, this series of tests was intended to complement the IMP6 auto-oscillation data. Both inducers perform in a similar manner outside of the region of instability. Upon entering the large amplitude auto-oscillation region, IMP8 suffers a large decrease in the head coefficient. This loss in head production is indicated in Fig. 5.14. If the cavitation number is reduced still further, auto-oscillation continues and follows trends identical to those of IMP6. However, to exit the region of auto-oscillation, it is necessary to increase the cavitation number above the value at which the system originally became unstable. This hysteretic behavior is characteristic of a nonlinear system. It is curious that the steady state head rise produced during auto-oscillation is essentially the same for all flow coefficients whose fully wetted head coefficients is greater than the value during auto-oscillation.

This hysteretic behavior was not investigated on IMP6 simply because IMP6 did not exhibit such a dramatic loss in the head coefficient. The observation that the cavitating backflow collapsed back towards the inlet plane of IMP6 and extended further down the blade passage is an indication that a small decrease in head production occurred.

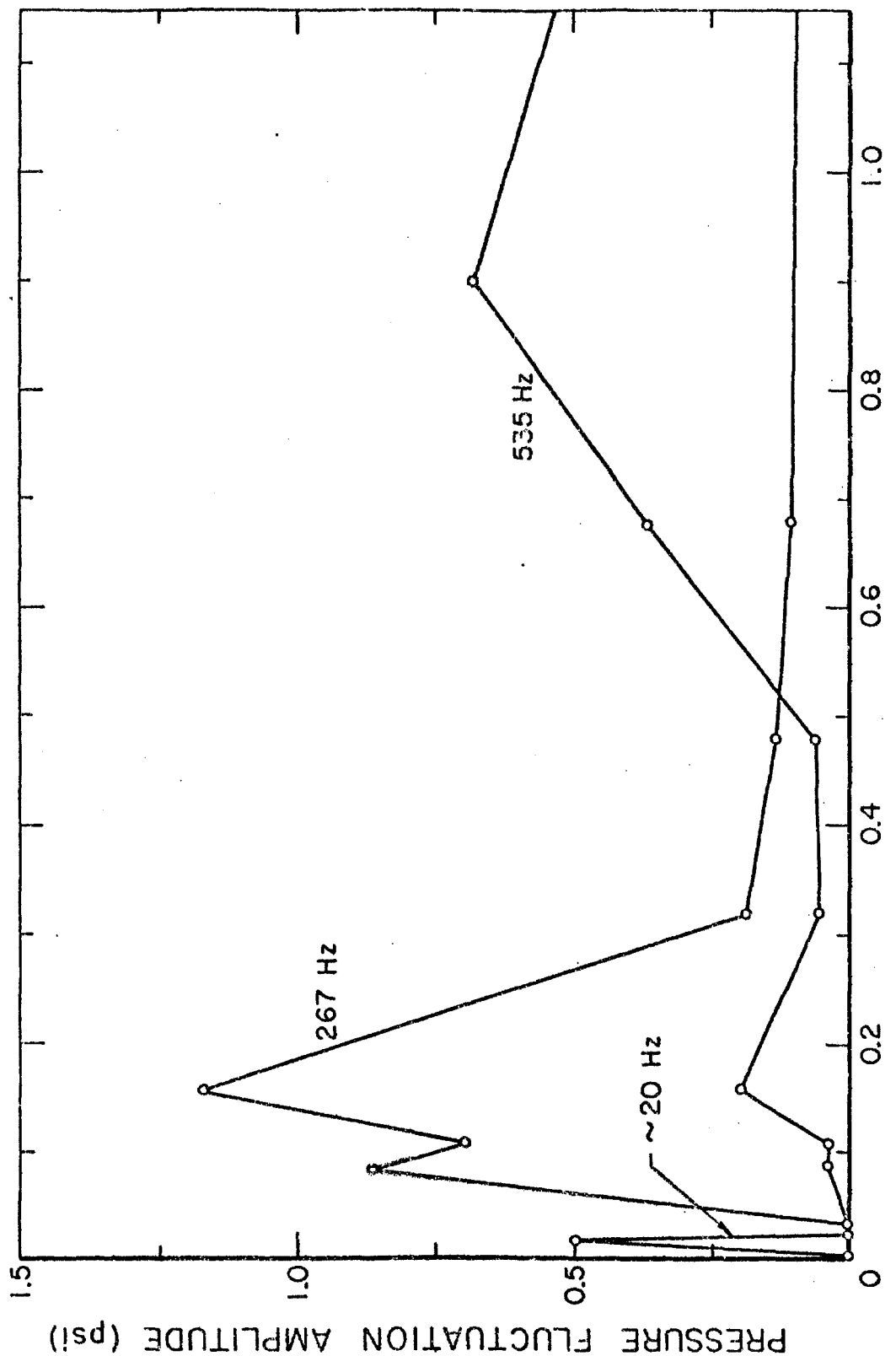

Fig. 5.1 Amplitude of the dominant frequency components of the wall pressure fluctuations within blade passage plotted against cavitation number for Impeller 6 at $\varphi = 0.070$.

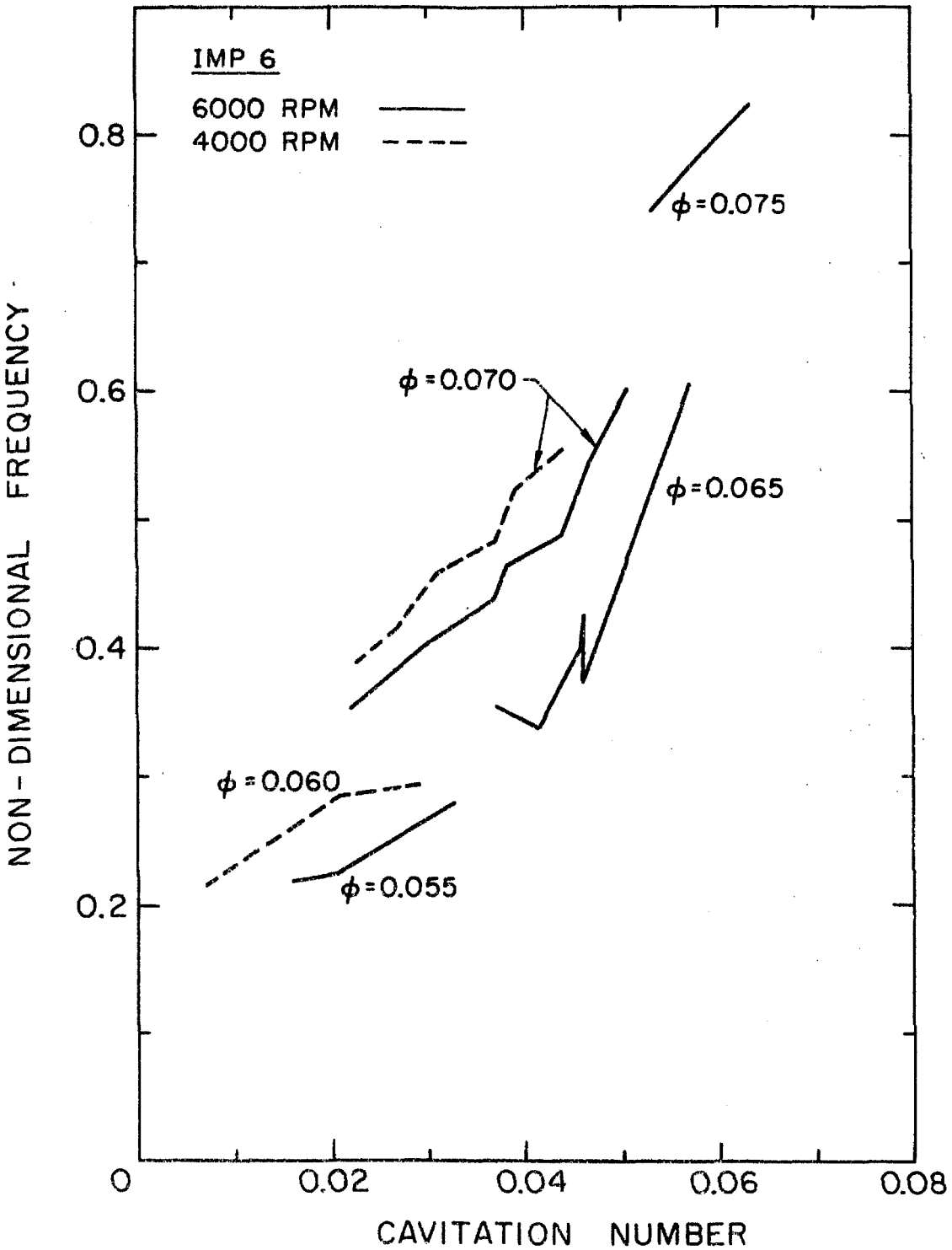

Fig. 5.2 Non-dimensional auto-oscillation frequencies associated with Impeller 6 at several flow coefficients and rotational speeds are plotted against cavitation number.

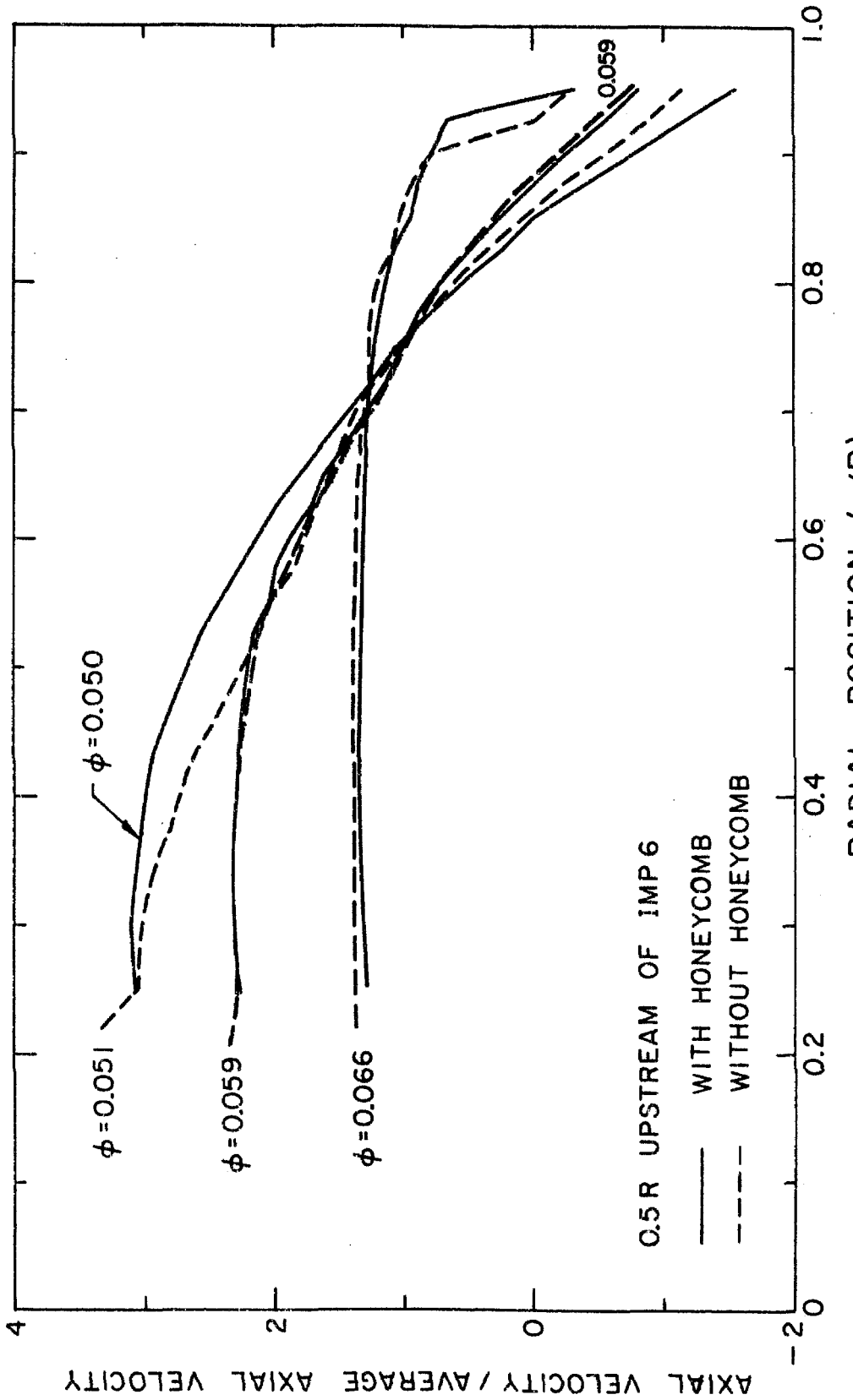

Fig. 5.3 Comparison of radial distribution of axial velocity profiles 0.5 radii upstream of Impeller 6 with and without the inlet flow straightener (honeycomb section mounted 2.0 radii upstream) at several flow coefficients.

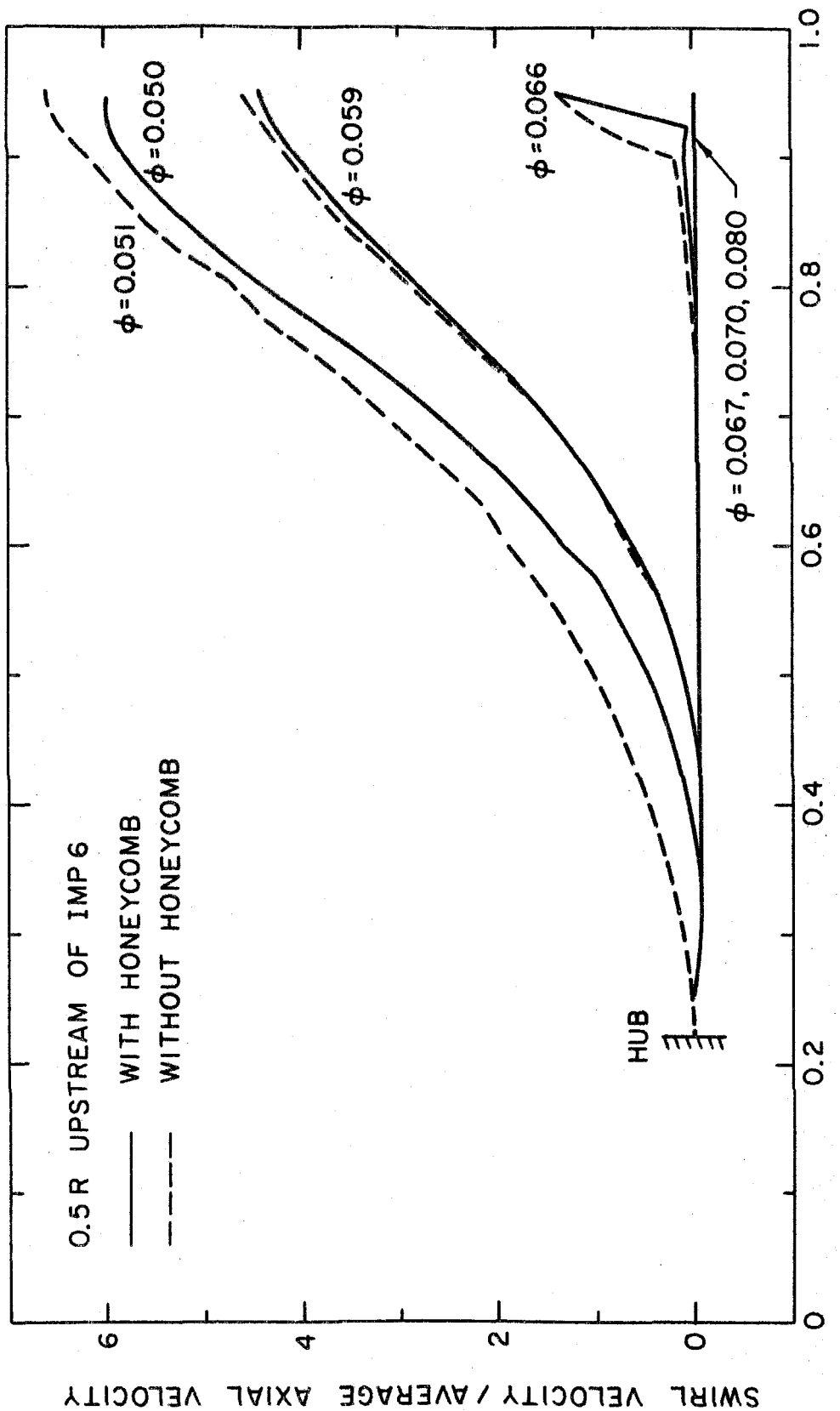

Fig. 5.4 Comparison of radial distribution of swirl velocity profiles 0.5 radii upstream of Impeller 6 with and without the inlet flow straightener (honeycomb section mounted 2.0 radii upstream) at several flow coefficients.

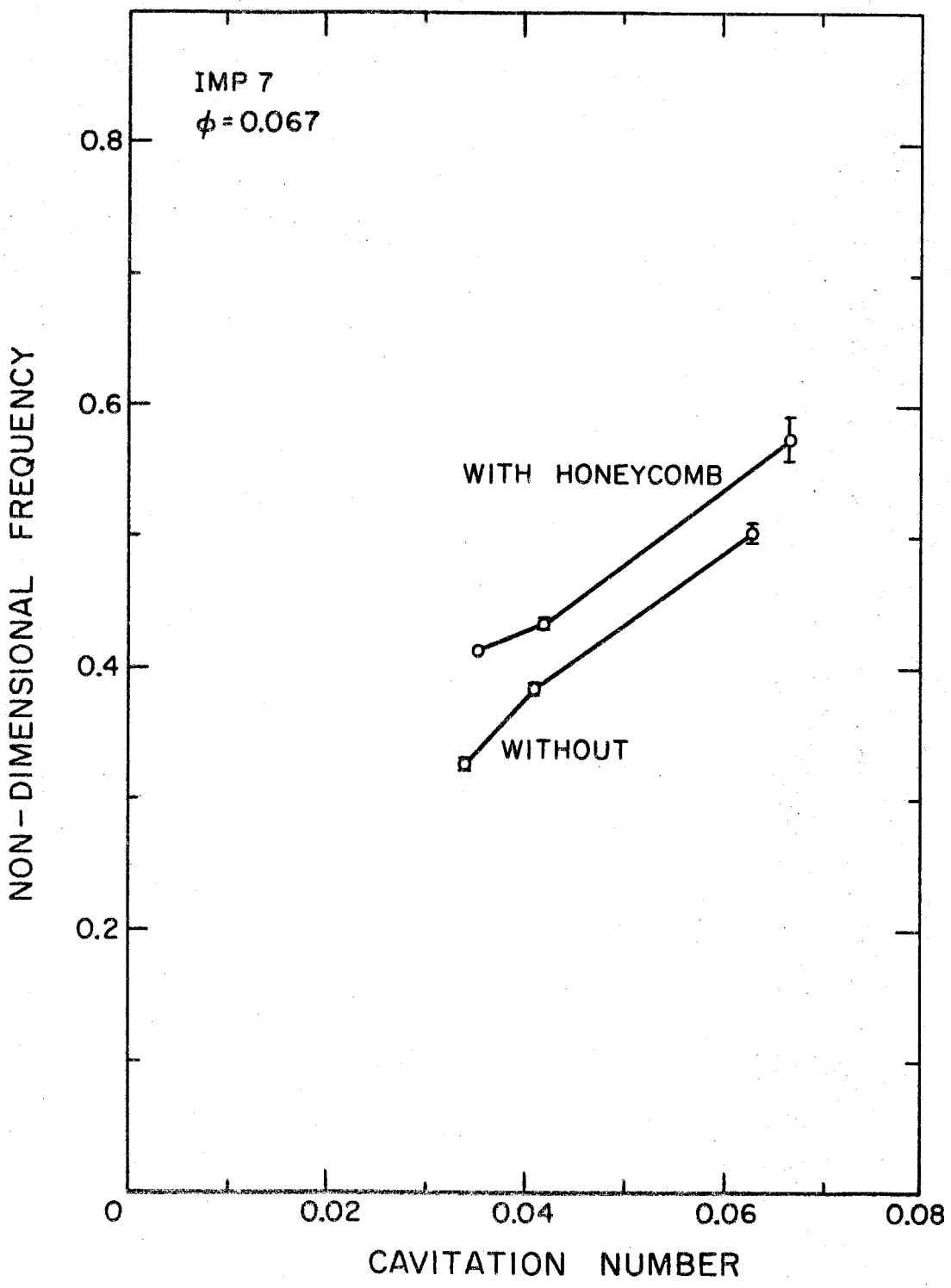

Fig. 5.5 Comparison between auto-oscillation frequencies associated with Impeller 7 operating at $\varphi = 0.067$ with and without the inlet flow straightener.

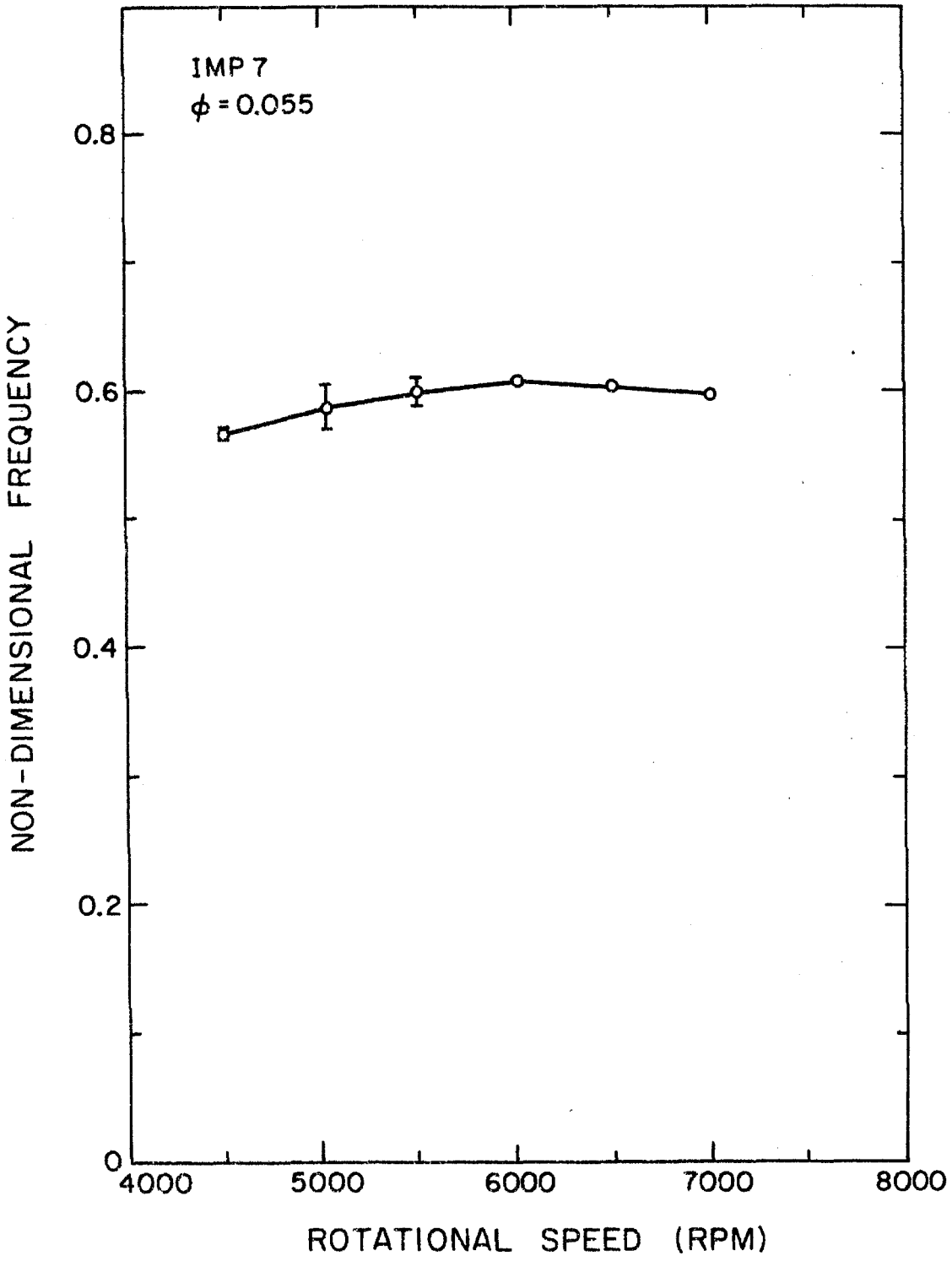

Fig. 5.6 Scaling of the auto-oscillation frequency with rotational speed of the inducer. Data were obtained with Impeller 7 at $\varphi = 0.055$ and $\sigma = 0.020$.

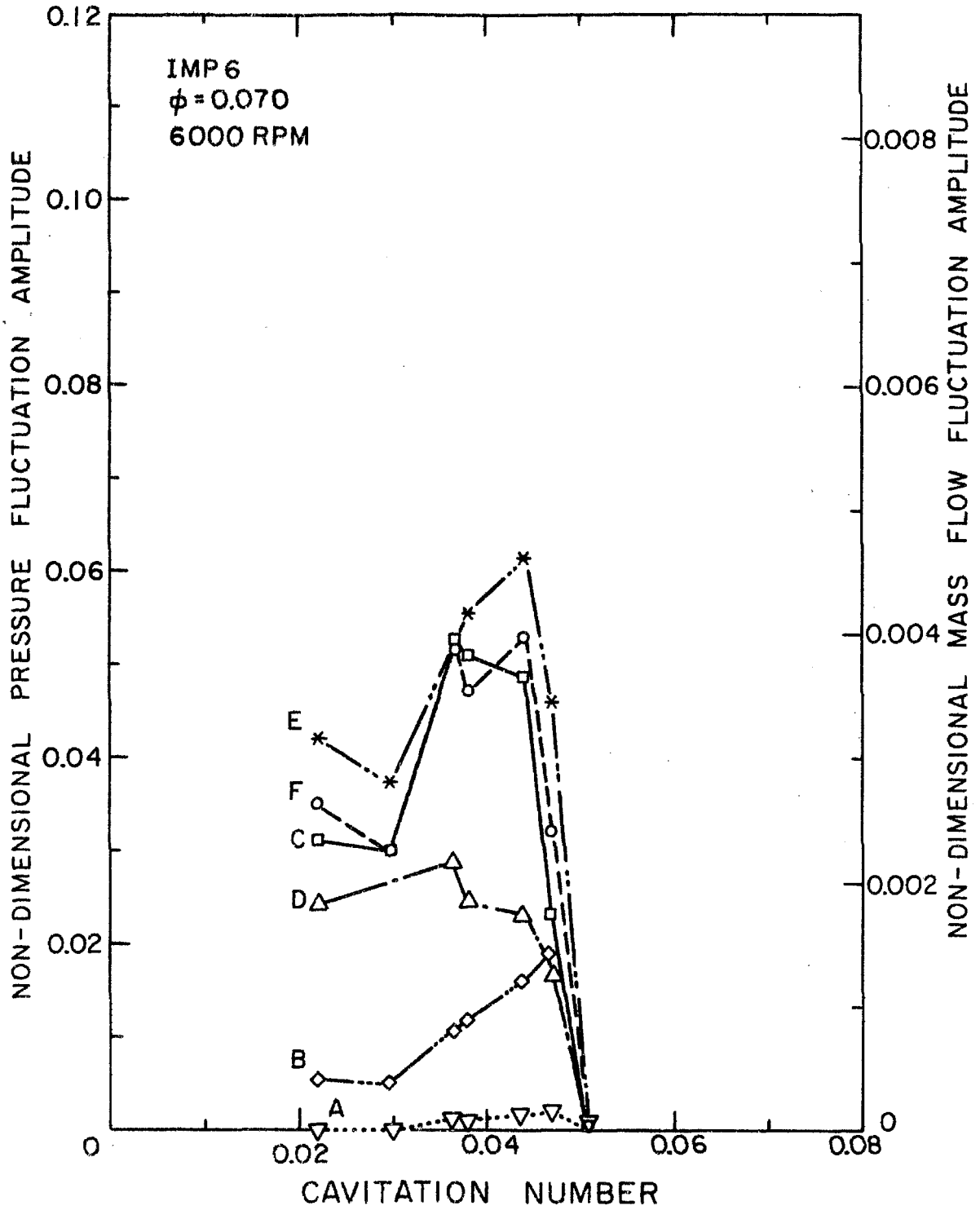

Fig. 5.7 Non-dimensional amplitudes of the fluctuating pressures and mass flow rates during auto-oscillation. These data were taken with Impeller 6 at $\varphi = 0.070$ and 6000 RPM. The letters correspond to the instrumentation so indicated on Fig. 2.3.

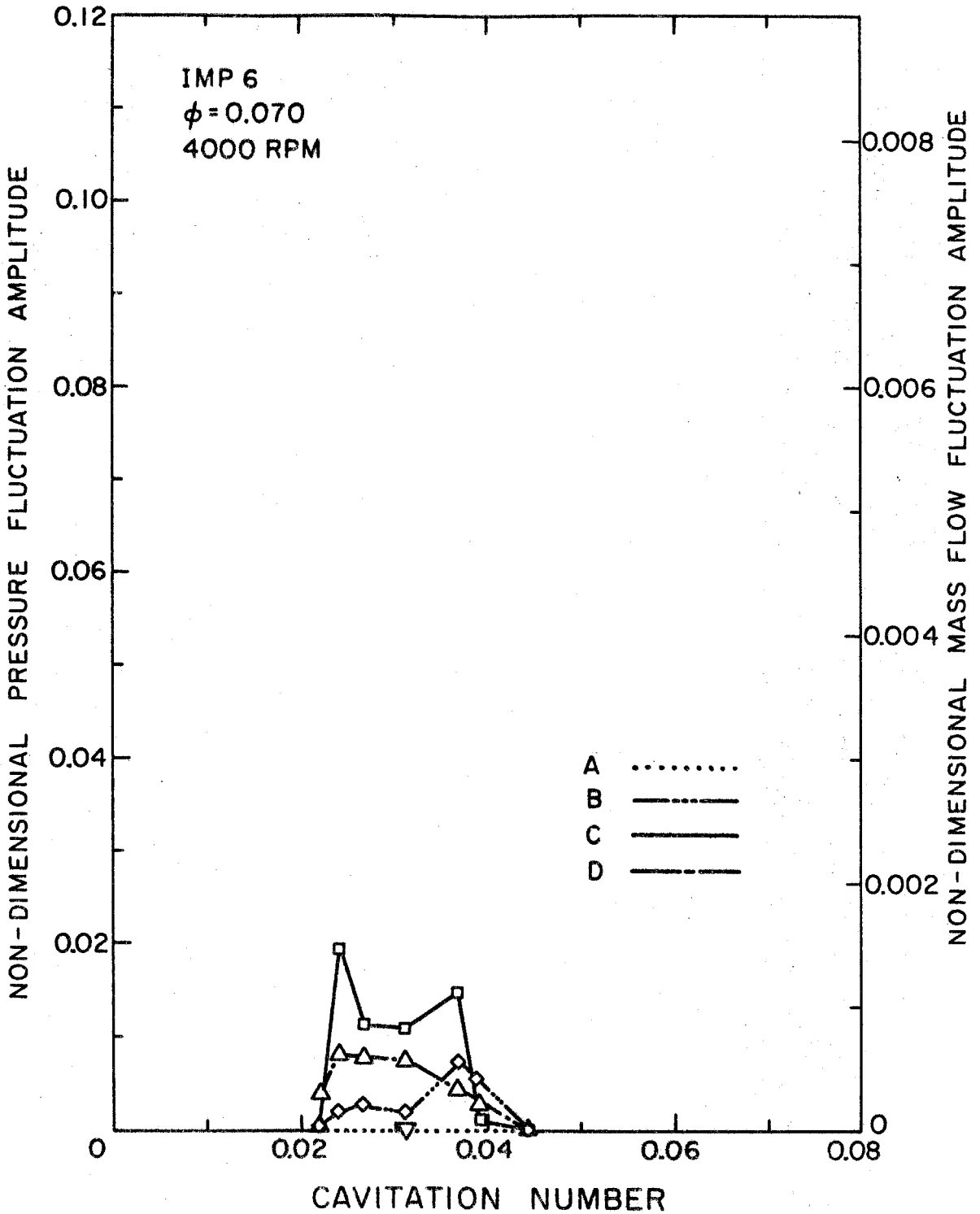

Fig. 5.8 Non-dimensional amplitudes of the fluctuating pressures and mass flow rates during auto-oscillation. These data were taken with Impeller 6 at φ = 0.070 and 4000 RPM. The letters correspond to the instrumentation so indicated in Fig. 2.3.

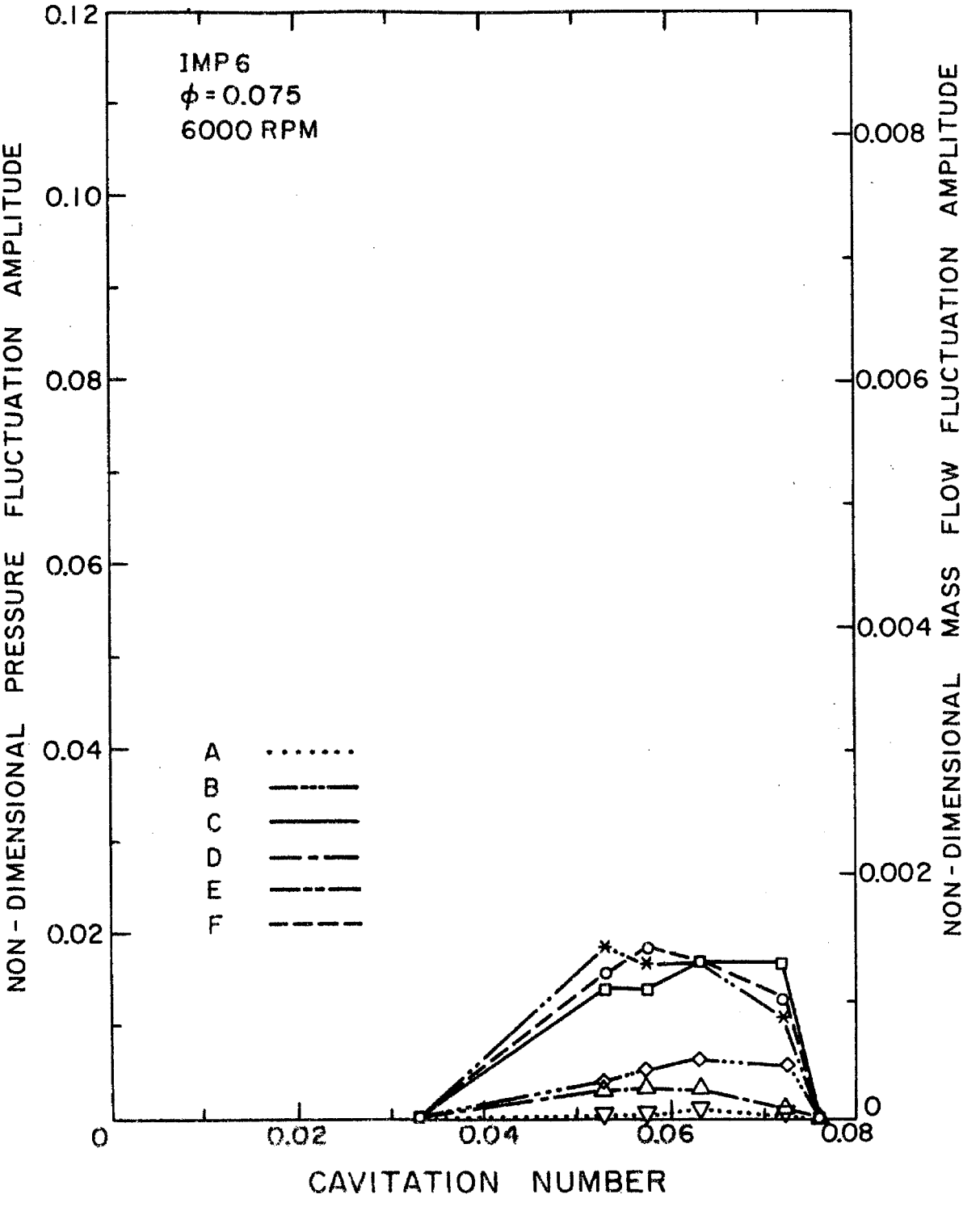

Fig. 5.9 Non-dimensional amplitudes of the fluctuating pressures and mass flow rates during auto-oscillation. These data were taken with Impeller 6 at φ = 0.075 and 6000 RPM. The letters correspond to the instrumentation so indicated in Fig. 2.3.

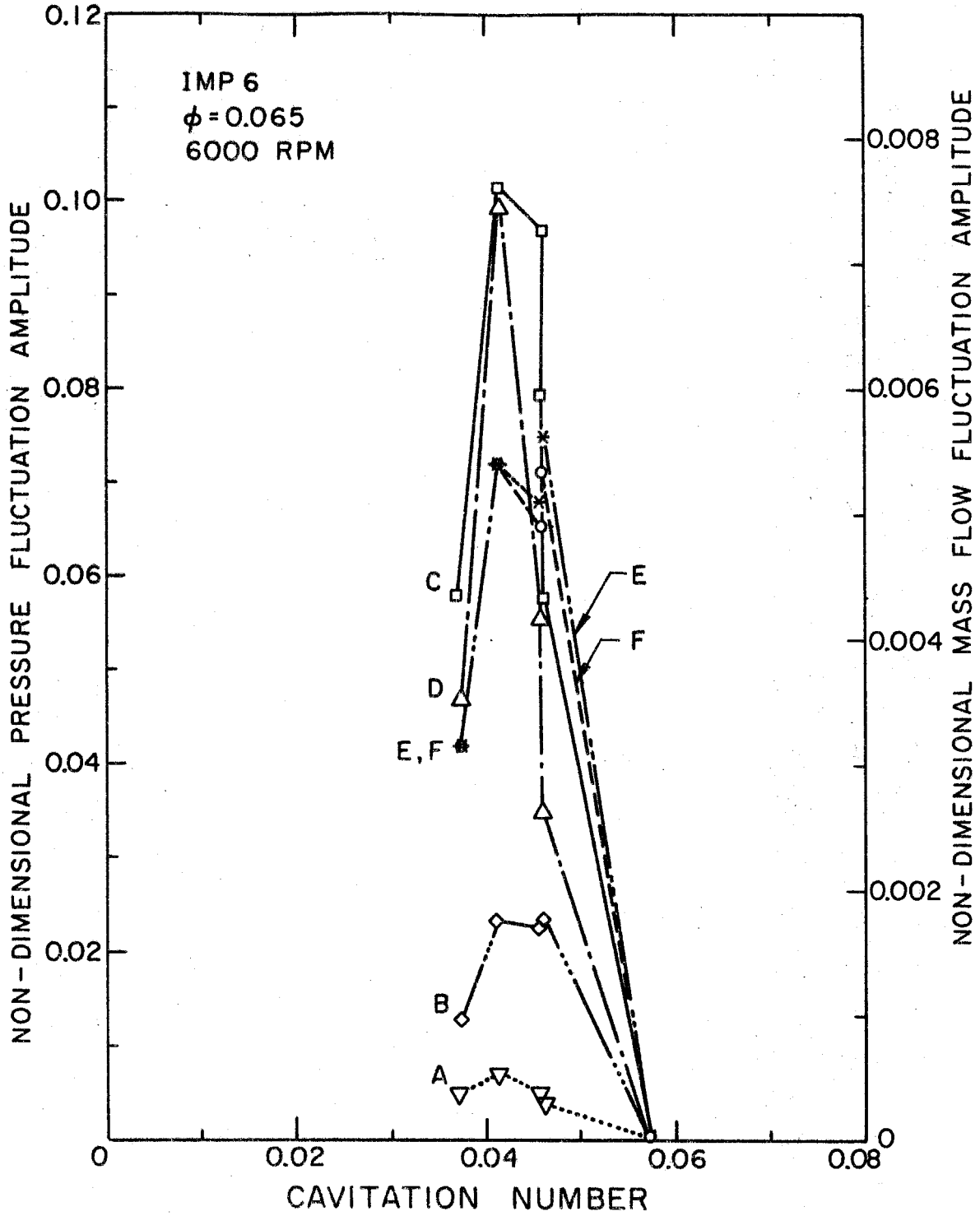

Fig. 5.10 Non-dimensional amplitudes of the fluctuating pressures and mass flow rates during auto-oscillation. These data were taken with Impeller 6 at $\varphi = 0.065$ and 6000 RPM. The letters correspond to the instrumentation so indicated in Fig. 2.3.

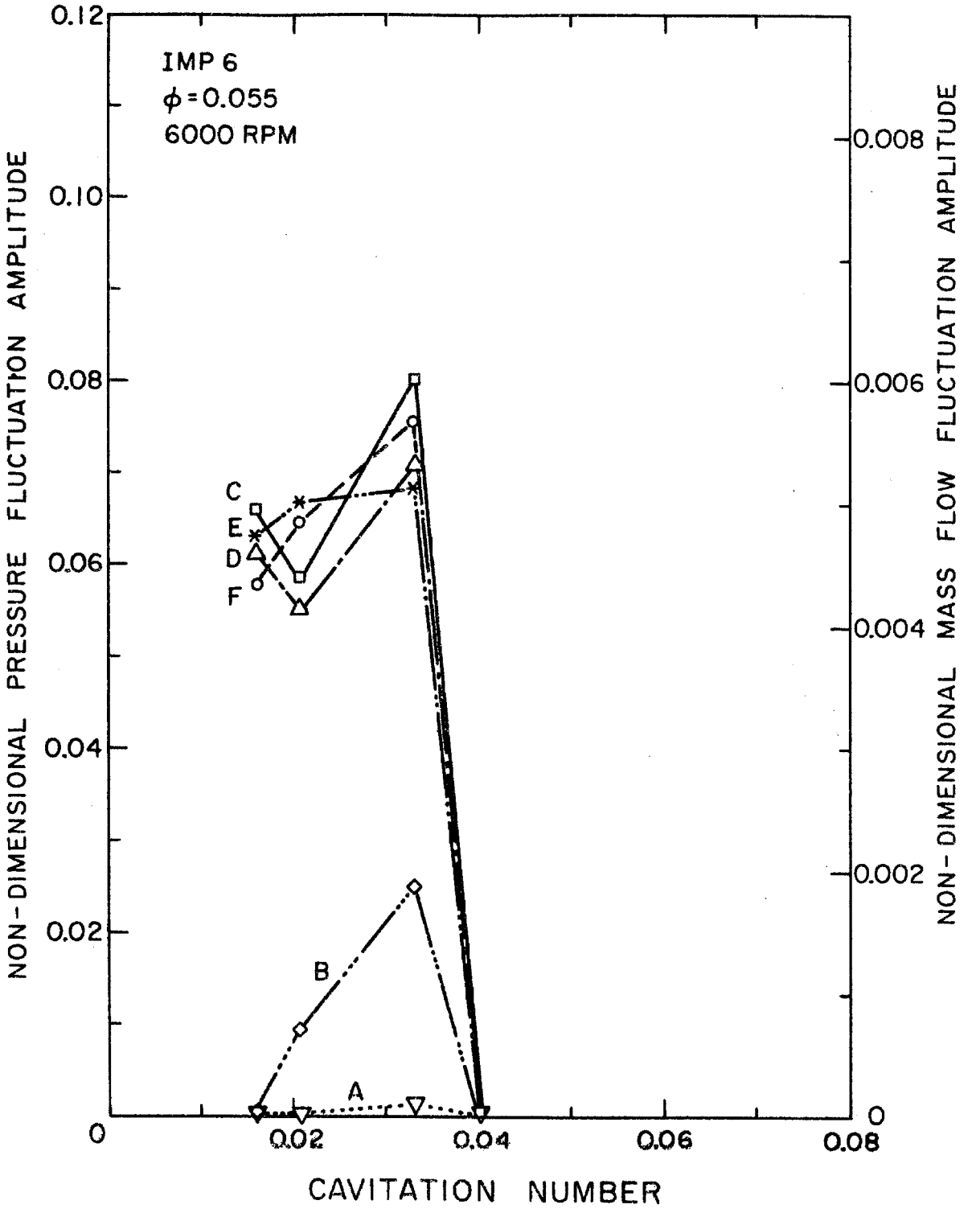

Fig. 5.11 Non-dimensional amplitudes of the fluctuating pressures and mass flow rates during auto-oscillation. These data were taken with Impeller 6 at φ = 0.055 and 6000 RPM. The letters correspond to the instrumentation so indicated in Fig. 2.3.

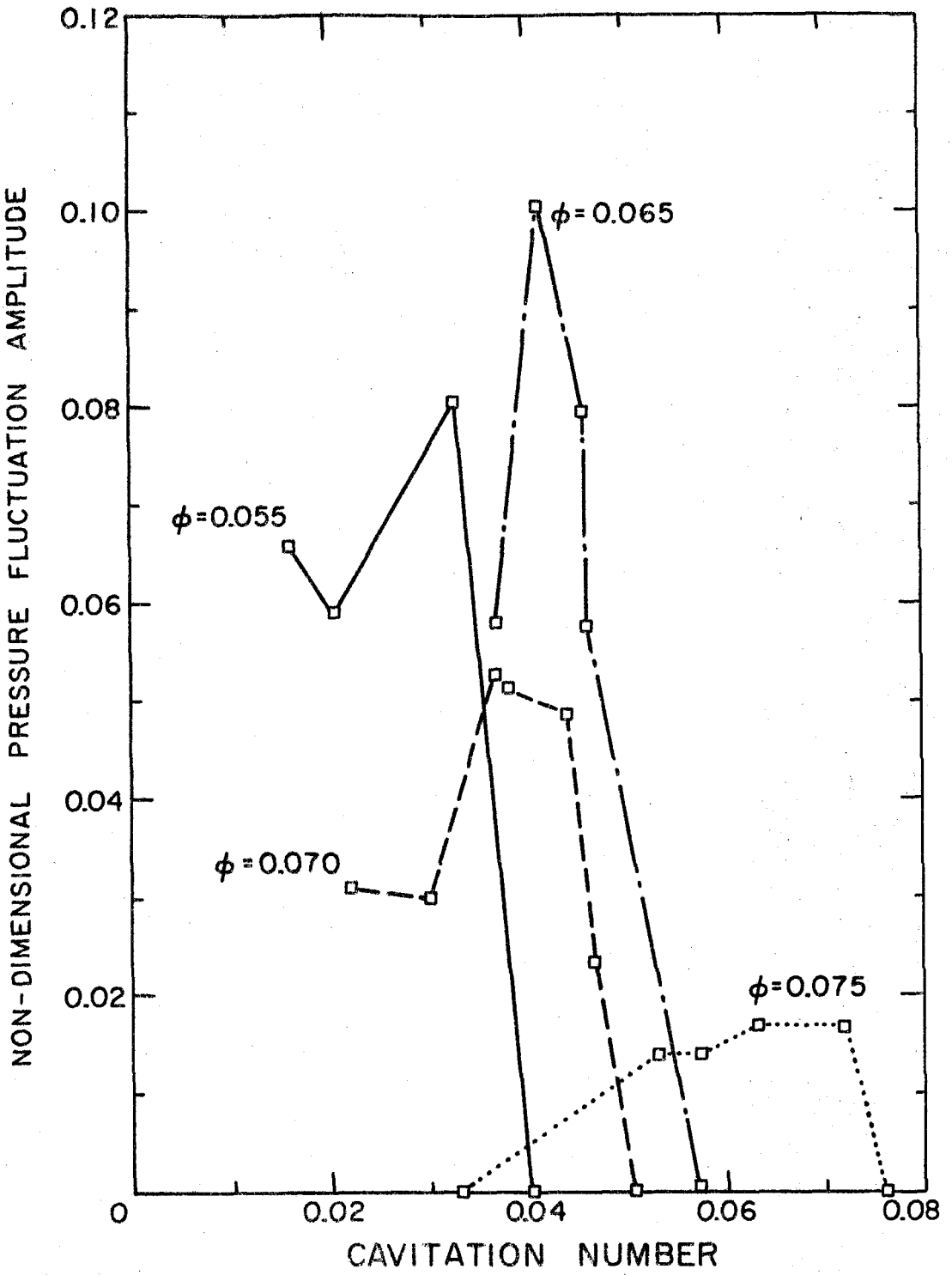

Fig. 5.12 Non-dimensional amplitude of the downstream pressure fluctuations during auto-oscillation at $\varphi = 0.075, 0.070, 0.065, 0.055$. These data were taken with Impeller 6 at 6000 RPM.

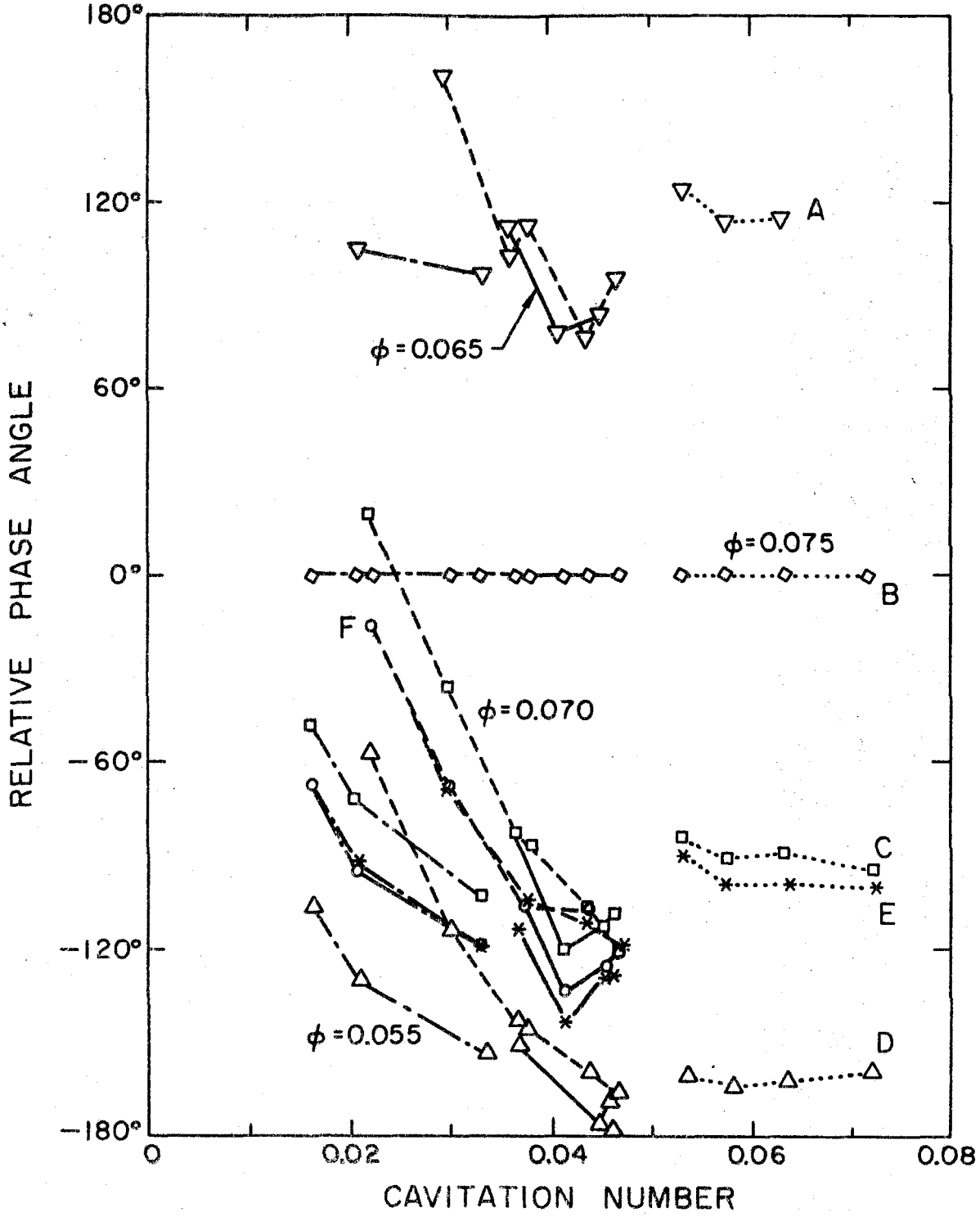

Fig. 5.13 Phase of fluctuating pressures and mass flow rates relative to the upstream mass flow rate (B) during auto-oscillation at φ = 0.075, 0.070, 0.065, 0.055. These data were taken with Impeller 6 at 6000 RPM. The letters correspond to the instrumentation so indicated in Fig. 2.3.

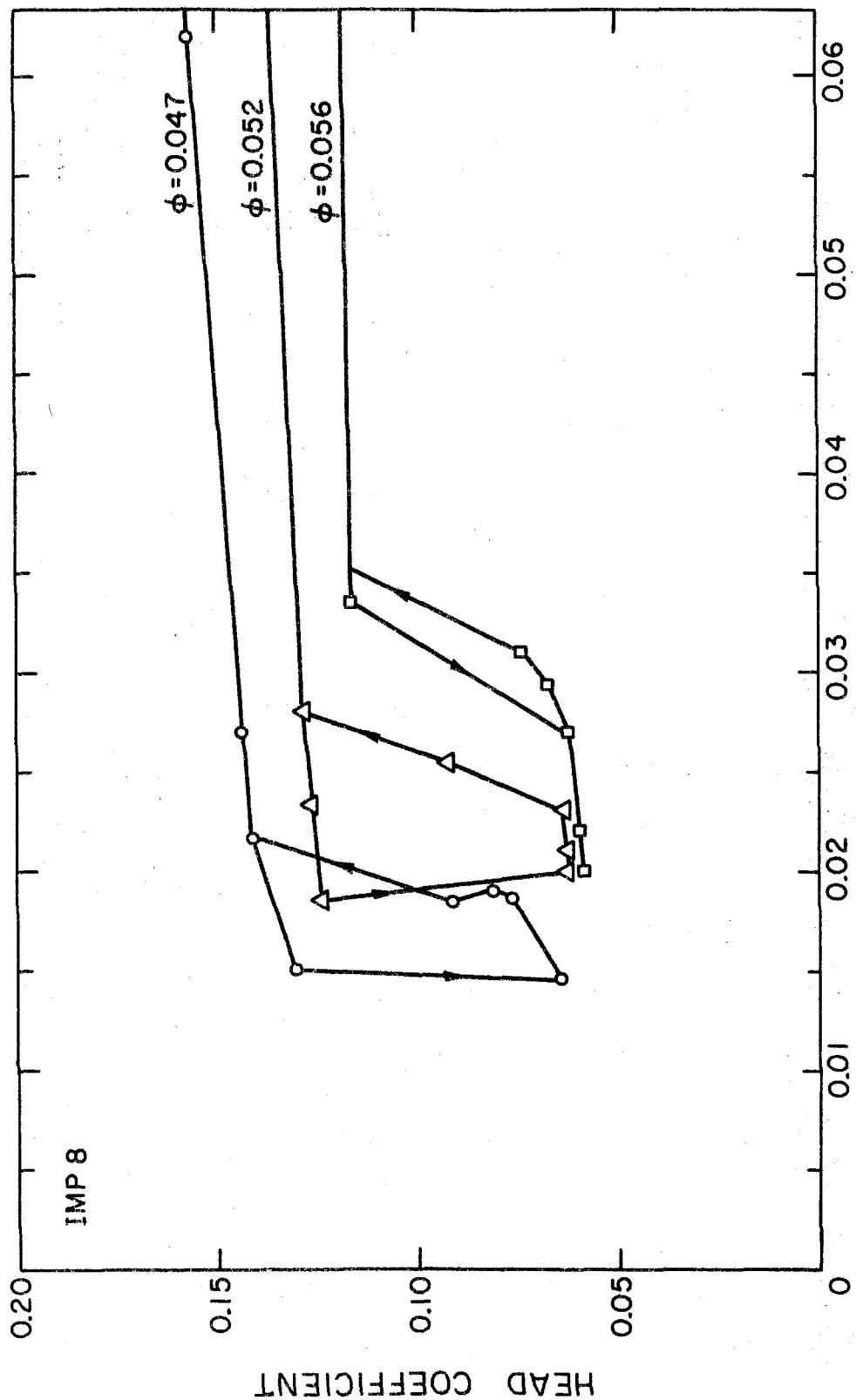

Fig. 5.14 Cavitation performance of Impeller 8 indicating hysteretic behavior and reduced head production associated with auto-oscillation.

VI. MODELS OF INLET FLOW DYNAMICS

6.1 Introduction

Several models of the inlet flow were proposed to independently investigate the dynamics of various features of this flow field. The parameters deemed important in light of the previous discussions are the inertance of the fluid within the system, the cavitation compliance in the backflow jet and the distribution of the swirl velocity ahead of the inducer. The complexity of the flow forced the models to be linear. Each of these models will be discussed in the remaining sections of this chapter.

6.2 Inertance Model

The simplest or most basic model of an unsteady, incompressible flow within a rigid pipe is the inertance model. This model neglects frictional effects and accounts solely for the pressure fluctuations resulting from the acceleration of the fluid within the pipe. The details of this model are described in Appendix D.1. The result of the analysis, Eq.(D.1.6), is repeated here.

$$\tilde{p}(z) = \tilde{p}_{\infty} - j\Omega z \tilde{w}_{\infty} \qquad (6.2.1)$$

where

$$p = \bar{p} + \tilde{p}\, e^{j\Omega t}$$

The far upstream pressure and velocity measurements, $\tilde{p}_{\infty}$ and $\tilde{w}_{\infty}$, were used as the reference quantities in this calculation. A typical axial pressure distribution calculated from Eq. (6.2.1) is presented in Figs. 6.1 and 6.2. These particular results were based on measurements of the upstream quantities $\tilde{p}_{\infty}$ and $\tilde{w}_{\infty}$ taken during

auto-oscillation at $\varphi = 0.070$ and $\sigma = 0.044$. The amplitudes and phases of the pressure fluctuations near the inlet to IMP6 are indicated on the figures. This model seems to predict the phase of the pressure fluctuations relative to the upstream mass flow rate reasonably well. The predicted amplitudes, however, are approximately an order of magnitude too small.

6.3 Compliant Backflow Model

The basic inertance model can be extended to include or simulate the effects of cavitation in the backflow jet. The cavitation will be assumed to form a continuous vapor layer of thickness $\delta(z,t)$ about the circumference of the pipe. The length of this cavitating region was selected arbitrarily but can be related to a particular flow coefficient through the inlet velocity profiles in Chapter 3 or photographs of IMP6 during auto-oscillation. In addition, the cavitation or vapor layer shall be assumed to act dynamically as a simple compliance. The details of this analysis are described in Appendix D.2. As in the inertance model, the far upstream velocity and pressure fluctuation measurements were used as the reference quantities. A typical axial distribution of the amplitude and phase of the pressure fluctuations is presented in Figs. 6.1 and 6.2. These particular results were based on measurements taken during auto-oscillation at $\varphi = 0.070$ and $\sigma = 0.044$. The length of the cavitating region was arbitrarily selected to be 3.0 radii. Again, the amplitudes predicted in the neighborhood of the inlet plane of IMP6 were an order of magnitude too small. In Fig. 6.2, the structure of the traveling waves generated by the cavitation is evident.

Clearly, the compressibility provided by the cavitation in the tip clearance jet does not adequately explain the experimental observations.

6.4 Swirling Inlet Flow Model

The previous two models have neglected the known three dimensional structure of the inlet flow field described in Chapter 3 and its effect upon the dynamics of this flow. As indicated in Chapter 5, the structure of the inlet flow field does influence the resulting auto-oscillation. For this reason, the structure of the steady flow field was incorporated into this third model, which is developed in Appendix E.

In addition to the incompressible, inviscid and axi-symmetric assumptions, it was necessary to neglect the known axial variation of the velocity field. The assumed steady velocities were therefore solely a function of the radial coordinate and were assumed to have the following form.

$$\begin{aligned} \mathcal{U}(r) &= U(r)/W_o = 0 \\ \mathcal{V}(r) &= V(r)/W_o = Nr^n \\ \mathcal{W}(r) &= W(r)/W_o = 1 + Kr^k \end{aligned} \tag{6.4.1}$$

where

$(\mathcal{U}, \mathcal{V}, \mathcal{W})$ is the non-dimensional velocity vector corresponding to (r, θ, z).

The problem is then linearized by perturbing this steady flow by a small amplitude harmonic traveling wave of the form $f(r)\, e^{(\alpha z + j\Omega t)}$. The dynamics of the inlet flow are then determined by the eigenvalue, α.

The eigenvalues, α, however, depend strongly upon the mean flow velocity profiles and the non-dimensional frequency, Ω. It turns out that a critical value of the swirl parameter, N, exists for given values of K and Ω. For values of N less than the critical value, N_{CR} the perturbation waves propagating upstream are attenuated. For these conditions, the flow is in a sense supercritical. Subcritical flow occurs for $N>N_{CR}$. The perturbation waves are not attenuated when $N>N_{CR}$.

In order to calculate the appropriate perturbation pressure and velocity fields, the values of the parameters K and N will be selected to correspond to the axial and swirl velocity profiles 0.5 radii upstream of IMP6 (Figs. 3.2 and 3.4). Table 6.1 lists the values of K and N for various "curvatures" in the mean velocity profiles for several flow coefficients. A consideration of Fig. E.4 in conjunction with the auto-oscillation frequency data, Fig. 5.2, indicates that these calculated values of N are all less than the appropriate critical swirl intensity. The predicted waves are therefore attenuated as they propagate upstream.

A typical example of the axial pressure distribution is presented in Figs. 6.3 and 6.4. These curves are based on the far upstream fluctuating pressure and mass flow rate measurements obtained during auto-oscillation at $\varphi = 0.065$ and $\sigma = 0.041$. The rapid attenuation of the perturbation waves corresponding to swirl intensities less than the critical value is apparent. In addition, the phase angle of the pressure fluctuations relative to the upstream mass flow rate rapidly converges to that of the inertance wave alone. The predicted phase angles of the pressure fluctuations at the inlet to IMP6 are in moderately good

agreement with the experimental data as indicated in Fig. 6.4. However, the amplitudes are not well predicted.

For comparison, the amplitudes and phases of the axial pressure distribution associated with a swirl intensity greater than the critical value are presented in Figs. 6.5 and 6.6. The same experimental data used in constructing Figs. 6.3 and 6.4 was used in these calculations. Again, the phase angle of the pressure field asymptotically approaches that of the inertance wave alone as the wave propagates further upstream. Similar statements concerning the predictive capability of the model under these conditions are applicable.

The neglect of the axial variation of the mean flow velocity distribution does not seem serious in the light of the above results. A systematic variation of the mean flow profiles to simulate their axial variation would not change the final conclusions.

This model of the inlet flow dynamics, as well as the previous two models, does not adequately predict the experimental observations. Since the inertance wave eventually masks the perturbation waves, this model is essentially no improvement over the inertance model. The results of Appendix E may, however, be of some use in other applications concerning confined rotating flows.

6.5 Transfer Function Model

It is now apparent that the various features of the inlet flow field do not act or respond independently of each other. Since the activity of an impeller results from cavitation and since a significant fraction of the cavitation occurs in the backflow ahead of the inducer, it seems possible that the transfer function of the inducer effectively

represents the dynamics of the inlet flow field. If so, then the transfer functions of IMP6 could be used to predict the inlet pressure fluctuations.

The IMP6 transfer function obtained at a flow coefficient of 0.070 and a cavitation number of 0.052 was used in the calculations. As before, the far upstream pressure and mass flow rate measurements obtained during auto-oscillation were used as the input variables. Since transfer functions at other flow coefficients were not available, the $\varphi = 0.070$ transfer function was used in all the calculations. The results of these calculations are presented in Table 6.2. The phases of the predicted inlet pressures are in good agreement with the data. An improvement in the amplitude prediction has occurred. The calculated amplitudes are approximately a factor of three low.

An alternate approach of using the measurements to determine the transfer function of this region of the flow has been attempted. Two linearly independent sets of data at each auto-oscillating condition are needed to uniquely define both elements of the transfer function. Unfortunately, only one set of data can ever be obtained. Thus, it is necessary to assume a value for one element and calculate the other. The results of this process are listed in Table 6.3. In this table, the elements of the original modified transfer function, X_{11} and X_{12}, appear in the first line. In the next two lines, the values of X_{11} and X_{12} determined from the auto-oscillation measurements are given. These results suggest that a large change in the dynamics of the inducer has occurred.

6.6 Discussion of Inlet Flow Models

As mentioned in Section 6.5, a large change in the dynamic

chacteristics of a cavitating inducer appears to accompany a condition of auto-oscillation. This is consistent with the indication of non-linearities in the performance of IMP8 described in Chapter 5. In addition, these models strongly suggest that the dynamics of the inlet flow field cannot be separated from those of the inducer. The coupling between the inlet flow and the inducer provided by the backflow is believed to be a central feature of the dynamics.

TABLE 6.1

		φ											
		0.080		0.070		0.067		0.066		0.059		0.051	
n	k	K	N	K	N	K	N	K	N	K	N	K	N
1	2	-.128	-.049	-.162	-.047	-.298	-.043	-.715	-.1663	-1.243	1.014	-1.369	1.396
2	2	-.128	-.061	-.162	-.059	-.298	-.052	-.715	.2555	-1.243	1.441	-1.369	1.970
3	2	-.128	-.067	-.162	-.067	-.298	-.056	-.715	.3436	-1.243	1.820	-1.369	2.444
1	-	0.0	-.052	0.0	-.050	0.0	-.049	0.0	.2459	0.0	2.244	0.0	3.217
2	-	0.0	-.064	0.0	-.063	0.0	-.059	0.0	.3779	0.0	3.189	0.0	4.540
3	-	0.0	-.070	0.0	-.071	0.0	-.064	0.0	.5081	0.0	4.027	0.0	5.631

TABLE 6.2

		INLET PRESSURE			
		AMPLITUDE		PHASE ANGLE	
φ	σ	EXPT	CALC	EXPT	CALC
0.055	0.033	22.94	10.80	-119.8	-127.8
0.065	0.041	16.67	6.21	-143.6	-134.3
0.070	0.044	12.68	3.65	-111.7	-109.6

TABLE 6.3

φ	σ	X_{11}		X_{12}	
		Real	Imag.	Real	Imag.
0.055	0.033	0.98	0.60	- 9.97	-14.34
		-21.40	12.92	-17.52	-33.24
0.065	0.041	0.81	0.72	- 8.22	-14.58
		- 4.44	5.09	-30.87	-31.63
0.070	0.044	0.19	1.02	- 3.62	-14.68
		-25.68	4.04	-18.10	-50.05

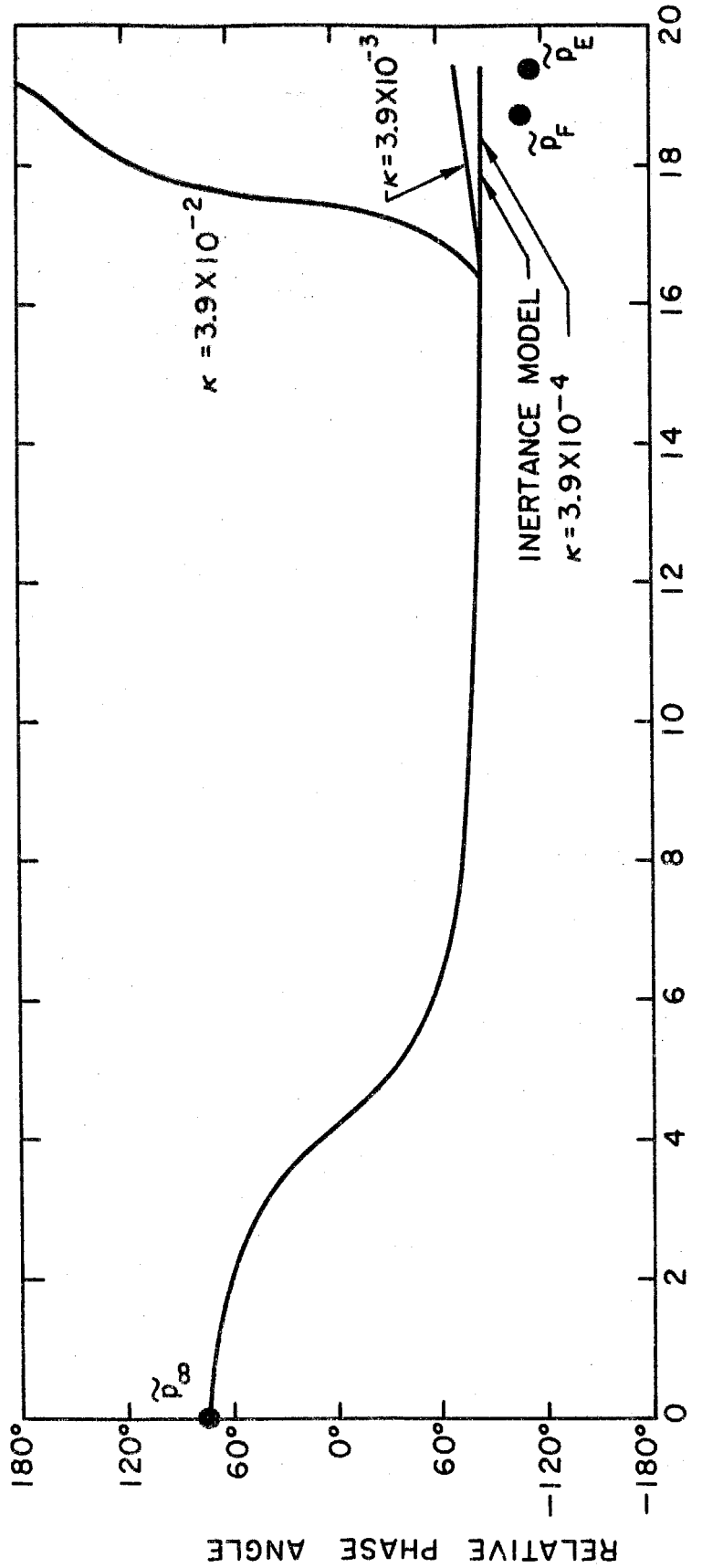

Fig. 6.1 Phase of pressure fluctuations relative to far upstream velocity fluctuations predicted by the inertance and compliant backflow models for auto-oscillation at $\varphi = 0.070$ and $\sigma = 0.044$. Also indicated are the measured phases of the inlet pressures, $\tilde{p}_E$ and $\tilde{p}_F$.

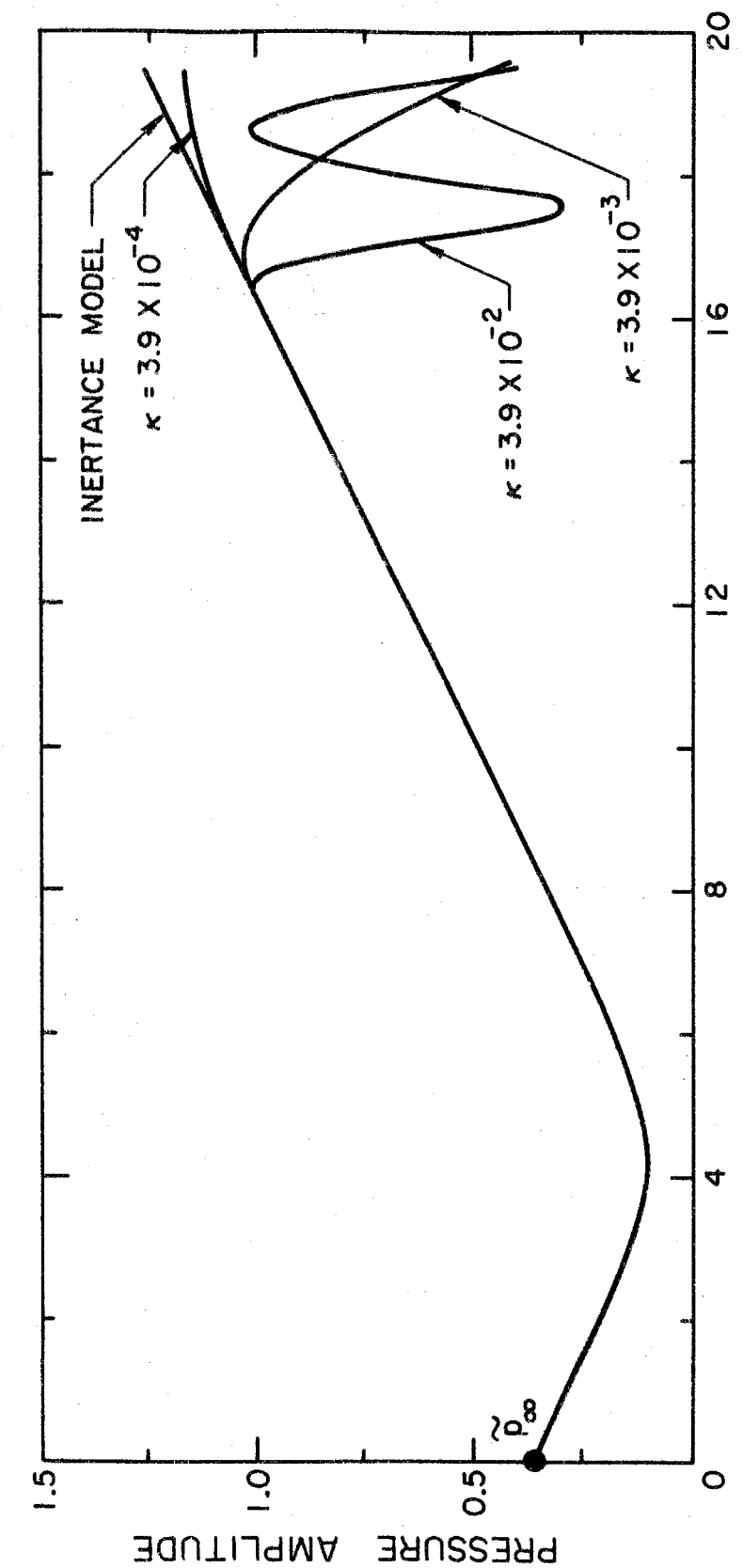

Fig. 6.2 Amplitude of axial pressure field predicted by the inertance and compliant backflow models. The measured amplitudes of the inlet pressure fluctuations, $\tilde{p}_E$ and $\tilde{p}_F$, were 12.7 and 10.8.

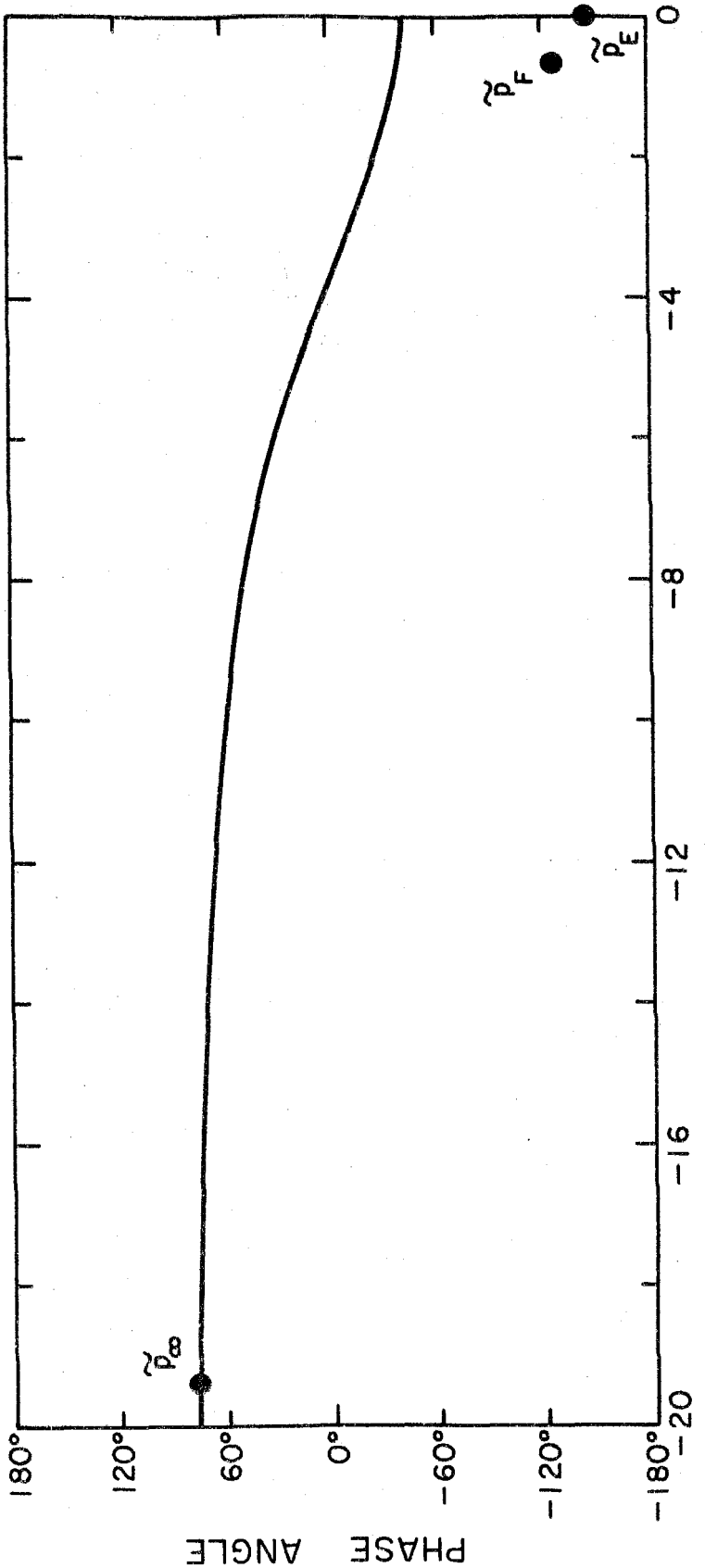

Fig. 6.3 Phase of wall pressure fluctuations relative to far upstream velocity fluctuations predicted by swirling inlet flow model for auto-oscillation at $\varphi = 0.065$ and $\sigma = 0.041$. The phases of the experimental inlet pressures $\tilde{p}_E$ and $\tilde{p}_F$ are also indicated.

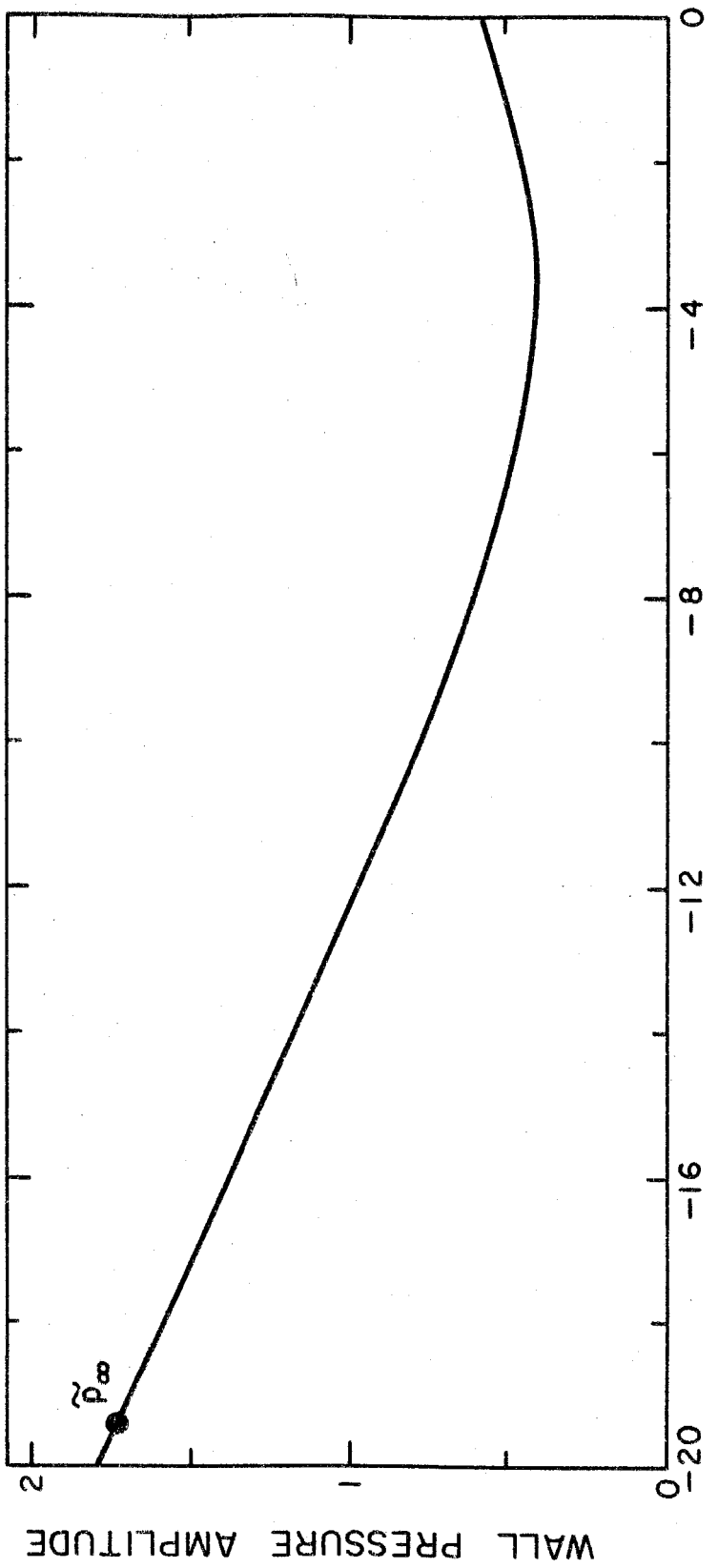

Fig. 6.4 Amplitude of wall pressure fluctuations predicted by swirling inlet flow model for auto-oscillation at $\varphi = 0.065$ and $\sigma = 0.041$. The measured amplitudes of the inlet pressure fluctuations, $\tilde{p}_E$ and $\tilde{p}_F$, were 16.7 and 17.6.

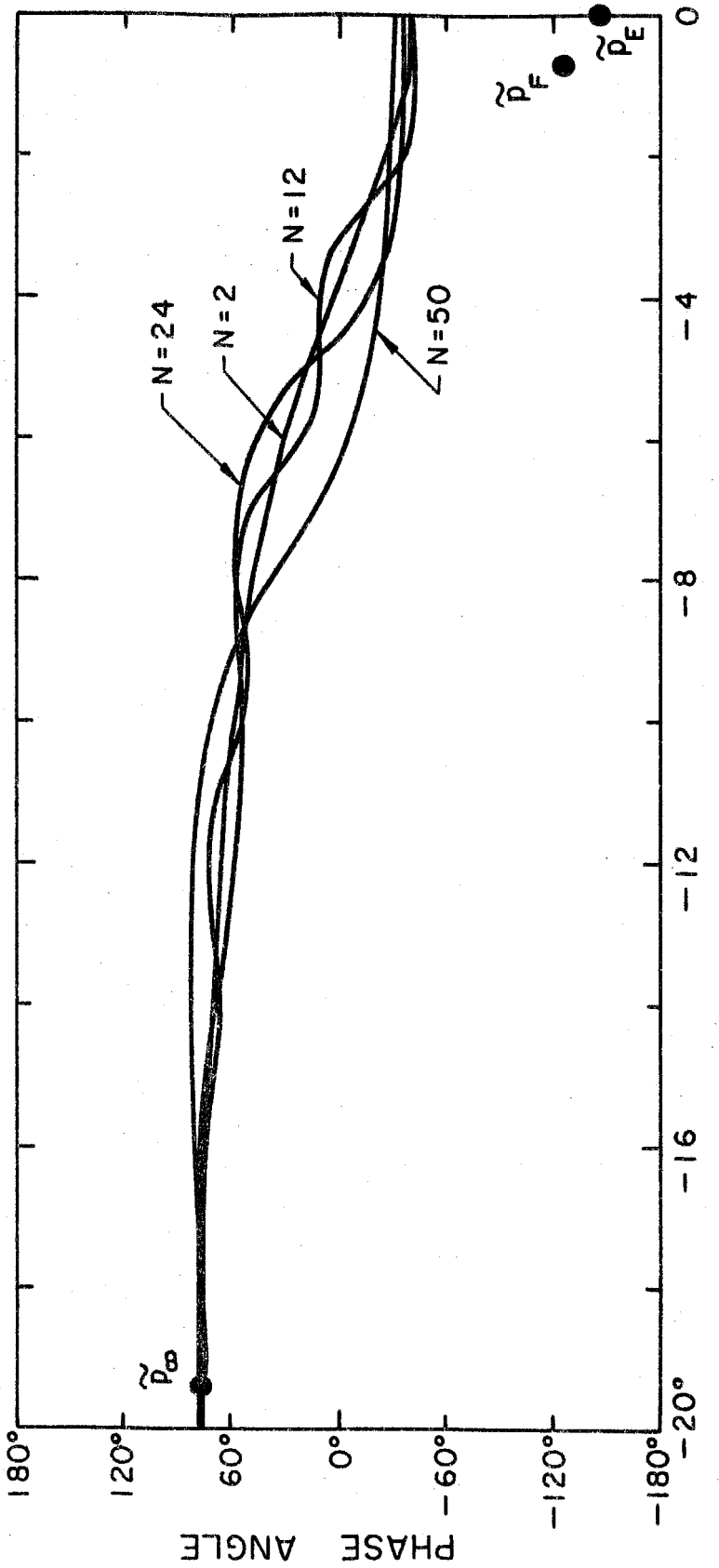

Fig. 6.5 Phase of wall pressure fluctuations relative to far upstream velocity fluctuations predicted by swirling inlet flow model for several different swirl velocity amplitudes ($V(r) = Nr^2$) and a uniform axial velocity. The solid circles indicate experimental measurements made during auto-oscillation at $\psi = 0.065$ and $\sigma = 0.041$.

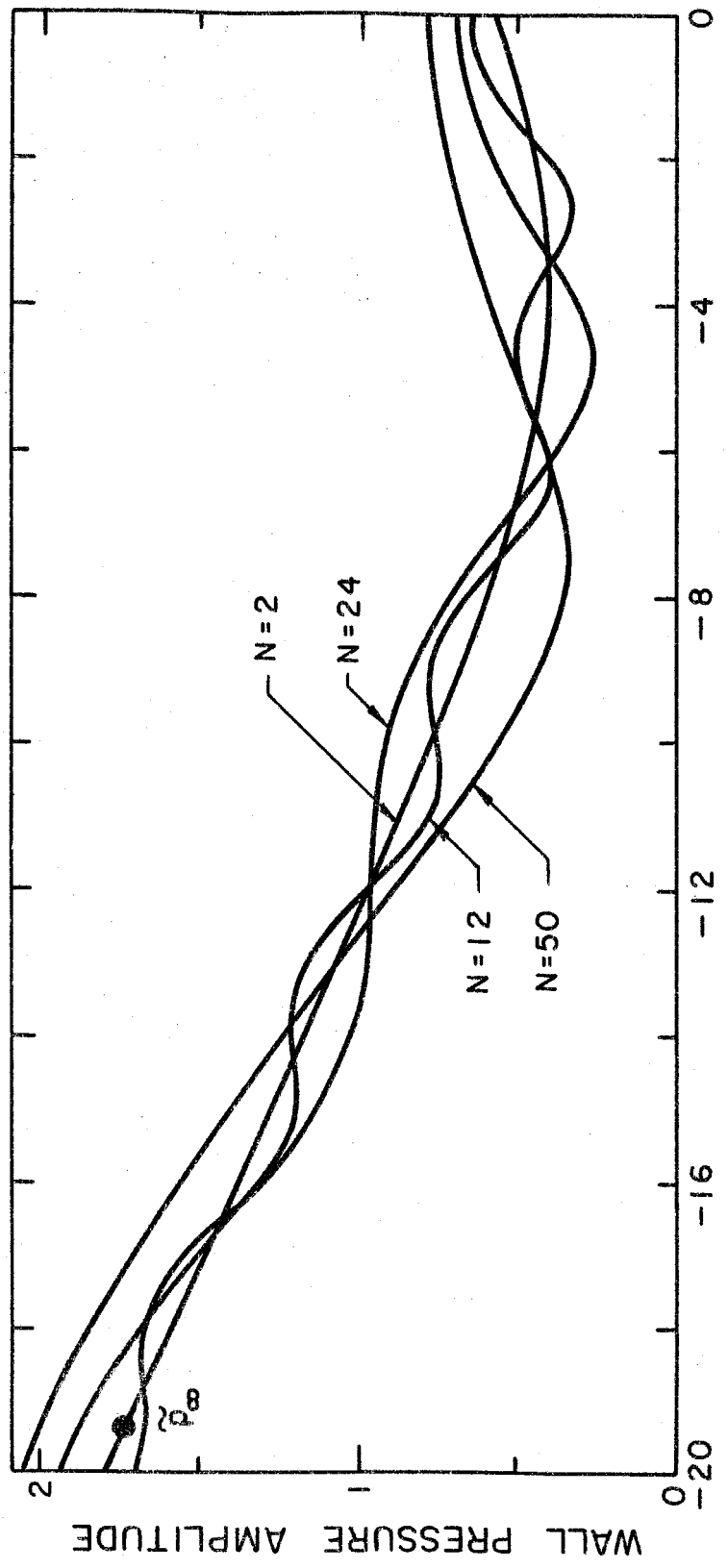

Fig. 6.6 Amplitude of wall pressure fluctuations predicted by swirling inlet flow model for several different swirl velocity amplitudes ($V(r) = Nr^2$) and a uniform axial velocity. The measured amplitudes of the inlet pressure fluctuation, $\tilde{p}_E$ and $\tilde{p}_F$, during auto-oscillation at $\varphi = 0.065$ and $\sigma = 0.041$ were 16.7 and 17.6.

SUMMARY AND CONCLUSIONS

The hydrodynamic, global instabilities associated with hydraulic systems containing cavitating inducer pumps have been investigated in the present research. A stability criterion was derived on the basis of a balance of flow energy "into" and "out" of the system. It was found that the linear stability of the system was determined by the dynamic characteristics of the entire system. The stability of the hydraulic system, however, was particularly sensitive to the dynamic characteristics of the inducer. The inducer is a dynamically active device. The activity of the inducer increases as the cavitation number decreases and thus is directly related to the cavitation induced dynamics of the inducer. The linear stability analysis is remarkably accurate in predicting both the onset and frequency of auto-oscillation. In addition, it successfully predicted the experimentally observed freqeuncy variation with cavitation number.

The underlying principles of the stability analysis are valid for a wide class of problems. Any system that can be modeled by a series combination of transfer functions is amenable to this type of analysis. It can be shown that a system will be unconditionally stable unless it contains at least one active element. Unfortunately, outside of the results of Refs. [10, 11, 16, 22, 41, 43], little is quantitatively known about the transfer functions of rotating fluid machinery, such as pumps and turbines, or other complex hydraulic elements. The results of this investigation indicate, however, that the use of quasi-static approximations of the pump performance is <u>not</u> adequate. The stability of the Dynamic Pump Test Facility is most sensitive to the mass flow gain factor, Z_{22}, and to a lesser degree the pump impedance, Z_{12}.

The pump compliance, Z_{21}, and dynamic pressure gain, Z_{11}, terms did not appreciably affect the stability of the system. The sensitivity of the Dynamic Pump Test Facility to the pump impedance and mass flow gain factor suggests that an accurate estimate of these quantities is required in the definition of the pump dynamics and in the stability analysis. It is recommended that the sensitivity of the results of any stability analysis to the parameters of the system's active element be investigated, especially if these are uncertainties concerning the actual values of these parameters.

Experimentally the instability, known as auto-oscillation, was found to occur in a well defined region of cavitation numbers just above head breakdown. Clearly, the entire hydraulic system participates in the instability since the large amplitude fluctuations in the pressure and mass flow rate occur throughout the system. However, in that the dynamics of the hydraulic system excluding the inducer are independent of cavitation number, auto-oscillation is a direct manifestation of the dynamically active behavior of the inducer. Furthermore, from the linear stability analysis, it is known that the stability of the Dynamic Pump Test Facility is extremely sensitive to the mass flow gain factor, Z_{22}. This suggests that the onset of auto-oscillation occurs when a critical value of this parameter is reached as the cavitation number is reduced. The frequency of oscillations is strongly influenced by the cavitation number and the tip speed of the inducer. Again, since the dynamic characteristics of the system excluding the inducer are independent of both the cavitation number and tip speed, these data indicate that the frequency of the instability is determined predominantly by the dynamics of the inducer. An estimate of the frequency can be obtained

in terms of the inertance and compliance of the inducer. Such an estimate does provide the correct scaling with tip speed of the inducer. In addition, calculations based on these parameters yield surprisingly accurate predictions of the auto-oscillation frequency. A certain amount of caution must be exercised when making estimates of this type, however, since the dynamics of the inducer are very complicated and physical effects are not isolated in only one element in the transfer function.

In comparing the pressure fluctuation measurements at the inlet of the inducer to those far upstream, it becomes clear that there are considerable dynamics associated with this flow field. The dynamics of the inlet flow field are included in the transfer functions of the inducer. Several dynamic models were proposed to separate out the dynamics of the inlet flow from those of the pump. These models separately incorporated the inertia of the fluid, the compliance effects of the cavitation and the backflow induced prerotation of the inlet flow. Although the models were unsuccessful in predicting the inlet pressure measurements, the dynamics of the inducer and inlet flow appear to be strongly coupled. It should also be noted that the mean or steady inlet velocity field is in itself not currently well understood.

Indications of nonlinear effects were also observed. The hysteretic behavior when entering and exiting the region of instability could cause some problems in the control of the system. However, the potentially large loss in the mean head production during auto-oscillation imposes an additional limitation on the operation of the hydraulic system. Besides structural integrity considerations in regards to the fluctuations in the flow, the decrease in the performance of the pump may also be unacceptable.

REFERENCES

1. Abbott, H. F., Gibson, W. L., and McCaig, I. W., 1963, "Measurements of Auto-Oscillation in Hydroelectric Supply Tunnel and Penstock System", Journal of Basic Engineering, Vol. 85, 1963, pp. 625-630.

2. Acosta, A. J., 1958, "An Experimental Study of Cavitating Inducers", Proceedings of Second O. N. R. Symposium on Naval Hydrodynamics, August 25-29, 1958, (ACR-38).

3. Acosta, A. J., 1974, "Cavitation and Fluid Machinery", Conference on Cavitation, Edinburgh, Scotland, September 3-4, 1974.

4. Acosta, A. J., and Wade, R. R., 1968, "Experimental Study of Cavitating Hydrofoils in Cascade", final report NASA contract NGR 05-002-059, February 1968.

5. Badowski, H. R., 1969, "An Explanation for Instability in Cavitating Inducers", ASME Cavitation Forum, 1969, pp. 38-40.

6. Barr, R.A., 1967, "Study of Instabilities in High Head Tandem Row Inducer Pumps", Hydronautics Interim Technical Report 703-1, February 1967.

7. Barton, M. V., 1951, "Vibration of Rectangular and Skew Cantilever Plates", Journal of Applied Mechanics, Vol. 18, 1951, pp. 129-134.

8. Braisted, D. M., and Brennen, C., 1978, "Observations on Instabilities of Cavitating Inducers", ASME Cavitation Forum, 1978, pp. 19-22.

9. Brennen, C., 1977, "On Non-Cavitating Axial Inducer Performance," Technical Brief, California Institute of Technology, Division of Engineering and Applied Science.

10. Brennen, C., 1977, "The Thermal-Hydraulic Transfer Function for a Phase Change in a Flowing Fluid System", to appear in the Journal of Fluids Engineering.

11. Brennen, C., 1978, "The Unsteady, Dynamic Characterization of Hydraulic Systems with Emphasis on Cavitation and Turbomachines", Proc. Int'l. Ctr. for Heat & Mass Trans. 1978 Seminar in Dubrovnik, Yugoslavia.

12. Brennen, C., 1978, "Bubbly Flow Model for the Dynamic Characteristics of Cavitating Pumps", Journal of Fluid Mechanics, Vol. 89, part 2, 1978, pp. 223-240.

13. Brennen, C., 1979, "A Linear Dynamic Analysis of Vent Condensation Stability", submitted to Journal of Fluids Engineering, July, 1979.

14. Brennen, C. and Acosta, A. J., 1973, "Theoretical, Quasi-static Analysis of Cavitation Compliance in Turbopumps", Journal of Spacecraft and Rockets, Vol. 10, No. 3, 1973, pp. 175-180.

15. Brennen, C. and Acosta, A. J., 1975, "The Dynamic Transfer Function for a Cavitating Inducer," ASME, 75-WA/FE-16.

16. Brennen, C., Meissner, C., Lo, E. Y., and Hoffman, G. S., 1979, "Scale Effects in the Dynamic Transfer Functions for Cavitating Inducers", (unpublished).

17. Brown, F. T., 1967, "A Unified Approach to the Analysis of Uniform One-Dimensional Distributed Systems", Journal of Basic Engineering, Vol. 89, 1967, pp. 423-432.

18. Dean, R. C. and Young, L. R., 1977, "Time Domain of Centrifugal Compressor and Pump Stability and Surge", Journal of Fluids Engineering, Vol. 99, pp. 53-63, 1977.

19. de Pian, L., 1962, Linear Active Network Theory, Prentice-Hall.

20. Doiran, H.H., 1977, "Space Shuttle Pogo Prevention", SAE, 770969.

21. Etter, R. J., 1970, "An Investigation of Tandem Row High Head Pump Inducers", Hydronautics Technical Report 703-9, May 1970.

22. Fanelli, M., 1972, "Further Considerations on the Dynamic Behavior of Hydraulic Turbo-machinery", Water Power, Vol. 24, No. 6, 1972, pp. 208-222.

23. Farrel, E. C. and Fenwick, J. R., 1973, "POGO Instabilities Suppression Evaluation, NASA Report CR-134500.

24. Freedland, B., Wing, O. and Ash, R., 1961, Principles of Linear Networks, McGraw-Hill.

25. Ghahremani, F. G., 1970, "Turbopump Cavitation Compliance", Report No. TOR-0059 (6531-01)-2, Aerospace Corporation, El Segundo, California.

26. Greitzer, E. M., 1976, "Surge and Rotating Stall in Axial Flow Compressors-Part I: Theoretical Compression System Model", Journal of Engineering for Power, Vol. 98, 1976, pp. 190-198.

27. Greitzer, E. M., 1976, "Surge and Rotating Stall in Axial Flow Compressors- Part II: Experimental Results and Comparison with Theory", Journal of Engineering for Power, Vol. 98, 1976, pp. 198-211.

28. Hennyey, Z., 1962, Linear Electric Circuits, Pergamon Press.

29. Hilten, J., Lederer, P., Vezzetti, C. and Mayo-Wells, J.F., 1976, "Development of Dynamic Calibration Methods for POGO Pressure Transducers", National Bureau of Standards (NBS) Technical Note 927, November 1976.

30. Hsu, Y.Y. and Graham, R.W., 1976, Transport Processes in Boiling and Two-Phase Systems, McGraw-Hill.

31. Jackson, E.D., 1966, "Final Report Study of Pump Discharge Pressure Oscillations", Rocketdyne Report No. R-6693-2.

32. Jaeger, C., 1963, "The Theory of Resonance in Hydropower Systems: Discussion of Incidents and Accidents Occurring in Pressure Systems", Journal of Basic Engineering Transactions, ASME, Vol. 85, pp. 631-640, 1963.

33. Kamijyo, K., 1975, "Closed Loop System Oscillations Associated with Cavitating Inducer", National Aerospace Laboratory, Japan.

34. Kamijyo, K., Shimura, T. and Watanabe, M., 1977, "An Experimental Investigation of Cavitating Inducer Instability", ASME, 77-WA/FE-14.

35. Lindholm, U.S., Kana, D.D., Chu, W.H. and Abramson, H.N., 1965, "Elastic Vibration Characteristics of Cantilever Plates in Water", Journal of Ship Research, Vol. 9, No. 1, June 1965, pp. 11-36.

36. Makhin, V.A., Gotsulenko, V.N. and Gotsulenko, N.N., 1975, "Instability (Surging) of Centrifugal Pump with Prepump", Soviet Aeronautics, Vol. 18, No. 8, pp. 150-154, 1975.

37. Meijer, M.C., 1959, "Some Experiments on Partly Cavitating Hydrofoils", Publication No. 12, International Shipbuilding Progress, Vol. 6, No. 60, 1959.

38. Miller, C.D. and Gross, L.A., 1967, "A Performance Investigation of an Eight-Inch Hubless Pump Inducer in Water and Liquid Nitrogen", NASA TN D-3807, March 1967.

39. Murphy, G.L., 1969, "POGO Suppression Analysis of the S-II and S-IVB LOX Feed Systems", Report No. ASD-ASTN-1040, Brown Engineering Company, Huntsville, Alabama.

40. Natazon, M.S., Bal'Tsev, N.I., Bazhanov, V.V. and Leydervarger, M.R., 1974, "Experimental Investigation of Cavitation Induced Oscillations of Helical Inducers", Fluid Mechanics - Soviet Research, Vol. 3, No. 1, pp. 38-45, January-February 1974.

41. Ng, S. L., 1976, "Dynamic Response of Cavitating Turbomachines", Ph. D. Thesis, California Institute of Technology, Pasadena, California.

42. Ng, S. L., Brennen, C., and Acosta, A. J., 1976, "The Dynamics of Cavitating Inducer Pumps", Conference on Two Phase Flow and Cavitation, Grenoble, 1976.

43. Ng, S. L., and Brennen, C., 1978, "Experiments on the Dynamic Behavior of Cavitating Pumps", Journal of Fluids Engineering, Vol. 100, pp. 166-176, June 1978.

44. Pearson, H. and Bowmer, T., 1949, "Surging of Axial Compressors", Aeronautical Quarterly, Vol. 1, pp. 195-210, 1949.

45. Powell, M. J. D., 1969, "Fortran Subroutine for Solving Systems of Nonlinear Algebraic Equations", Numerical Methods for Nonlinear Algebraic Equations, ed. P. Rabinowitz, Gordon and Breach Science Publishers.

46. Rosenmann, W., 1962, "Mark 10 LOX Inducer Test Report", Internal Correspondence TAMM 2115-17, North American Aviation, February 28, 1962.

47. Rosenmann, W., 1964, "Model Mark 10 LOX Inducer Test Report", Internal Correspondence TAMM 4115-67, North American Aviation, June 11, 1964.

48. Rubin, S., 1966, "Longitudinal Instability of Liquid Rockets due to Propulsion Feedback (POGO)", Journal of Spacecraft and Rockets, Vol. 3, No. 8, pp. 1188-1195, 1966.

49. Sack, L. E. and Nottage, H. B., 1965, "System Oscillations Associated with Cavitating Inducers", Journal of Basic Engineering, Vol. 87, pp. 917-924, December 1965.

50. Soltis, R. F., 1965, "Some Visual Observations of Cavitation in Rotating Machinery", NASA TN D-2681, July 1965.

51. Stepanoff, A. J., 1948, Centrifugal and Axial Pumps; Theory, Design and Application, Wiley.

52. Streeter, V. L., and Wylie, E. B., 1967, Hydraulic Transients, McGraw-Hill.

53. Taylor, W. E. Murrin, T. A. and Columbo, R. M., 1969, "Systematic Two-Dimensional Cascade Tests, Volume I - Double Circular Arc Hydrofoils", NASA CR-72498, December 1969.

54. Weinberg, L., 1962, Network Analysis and Synthesis, McGraw-Hill.

55. Yeh, H.,1959, "An Acutator Disc Analysis of Inlet Distortion and Rotating Stall in Axial Flow Turbomachines", Journal of the Aero/Space Sciences, pp.739-753, Vol. 26, November 1959.

56. Young, W.E., Murphy, R. and Reddecliff, J.M., 1972, "Study of Cavitating Inducer Instabilities", PWA FR-5131, Pratt-Whitney Aircraft, August 1972.

APPENDIX A
DYNAMIC PRESSURE TRANSDUCER CALIBRATION

A.1 Test Procedure

The dynamic pressure transducer calibration scheme is based upon inertially generated sinusoidal pressure fluctuations. The experimental setup consisted of a tube containing a column of water (see Fig. A.1). The top of the tube was left open to the atmosphere. The pressure transducers were connected to a mounting block at the base of the tube. This entire system was mounted vertically on a Ling electro-magnetic shaker. The shaker was used to provide a harmonic excitation of the water column. In addition, an Endevco Model 2272 piezioelectric accelerometer was mounted on the system to provide a reference waveform.

During the calibration tests, the maximum acceleration levels were kept at less than 0.5 g. Typically, data were obtained over a frequency range of 4-250 Hz. The transducer outputs were recorded on a four channel Hewlett Packard Model 3960 instrumentation tape recorder. The amplitude and phase relationships of the recorded data were obtained by means of a Spectral Dynamics Model SD360 Signal Analyzer. The signal analyzer used a Fast Fourier Transform to calculate the spectra of the data. The phase of the pressure transducer outputs relative to the base acceleration was determined by a cross-correlation of the two wave forms.

The results of these calibration tests are presented in Figs. A.2—A.5. Clearly, a resonance has occurred for each of the five pressure transducers.

A.2 Analysis of Calibration Scheme

A one-dimensional model of the flow within the tube yields the following result.

$$p(0) = p_{ATM} + \rho g \ell_o + \rho \ell_o \tilde{a} e^{j\omega t} \qquad (A.1)$$

where

g = gravitation acceleration

$\tilde{a}$ = amplitude of base acceleration

ℓ_o = height of water column.

Clearly, the pressure fluctuations depend entirely upon the base acceleration.

The above result must be modified if a compliant element exists within this system. The diaphragm of the pressure transducers provides such an effect. As a result, relative motion between the tube and water exists. The expression for the pressure at the base of the tube now becomes

$$p(0) = p_{ATM} + \rho g \ell(t) + \rho \ell(t) \tilde{a} e^{j\omega t} + \rho \ell(t) \frac{d}{dt} v_r(t) \qquad (A.2)$$

where

$\ell(t)$ = height of water column

$v_r(t)$ = velocity of water column relative to the tube.

This is not the pressure at the transducer, however. The transducer connections have dynamics of their own which must be accounted for. If ℓ_c and A_c represent the equivalent length and cross-sectional area of the transducer connections, then the pressure at the transducer is given by

$$p_{TR} = p(0) - \rho \ell_c \frac{d}{dt} u_r(t) \qquad (A.3)$$

where

$u_r(t)$ = velocity of water in transducer connections.

The pressure at the transducer is related to the volume change by

$$\frac{dp_{TR}}{dt} = \frac{1}{C} \frac{dv}{dt} \qquad (A.4)$$

where

C = compliance of pressure transducer

v = volume of transducer.

Continuity considerations yield the following relationships.

$$\frac{dv}{dt} = -A_T \frac{d\ell(t)}{dt}$$

$$v_r(t) = \frac{d\ell(t)}{dt} \qquad (A.5)$$

$$u_r(t) = -\frac{A_T}{A_c} \frac{d\ell(t)}{dt}$$

where

A_T = cross sectional area of the tube.

Substituting all of the above expressions into Eq. (A.3) gives the following result.

$$\left(\frac{\ell(t)}{A_T} + \frac{\ell_c}{A_c}\right) \frac{d^3\ell(t)}{dt^3} + \frac{1}{A_T} \frac{d\ell(t)}{dt} \frac{d^2\ell(t)}{dt^2}$$

$$+ \left(\frac{g + \tilde{a}e^{j\omega t}}{A_T} + \frac{1}{\rho C}\right) \frac{d\ell(t)}{dt} + \frac{j\omega \tilde{a} e^{j\omega t}}{A_T} \ell(t) = 0 \qquad (A.6)$$

Equation (A.6) can be linearized by assuming that

$$\ell(t) = \ell_o + \tilde{\ell} e^{j\omega t} \quad . \qquad (A.7)$$

Substituting this back into equation (A.6) yields an expression for the fluctuating height of the water column, $\tilde{\ell}$, in terms of the inertances of the water column and transducer connections, and the compliance of the pressure transducer.

$$\tilde{\ell} = \frac{\tilde{a}\ell_o}{A_T} \left[\frac{1}{\omega^2 \left(\frac{\ell_o}{A_T} + \frac{\ell_c}{A_c}\right) - \left(\frac{g}{A_T} + \frac{1}{\rho C}\right)} \right] \qquad (A.8)$$

It is apparent that a resonance can occur under appropriate circumstances. Equation (A.8) provides an explanation for the resonant behavior observed during the dynamic pressure transducer calibration tests. In addition, it can be seen that the natural frequency of the measuring system is sensitive to the compliance of the transducer or any other source of compliance (i.e. trapped air bubbles, cavitation, structural compressibility, etc.).

Equations (A.2) and (A.3) are then used to fit the experimental calibration curves up to the first resonance given in Figs. A.2 and A.4. This process determined the unknown compliance of the transducer. It was these fitted curves which were applied to the auto-oscillation data.

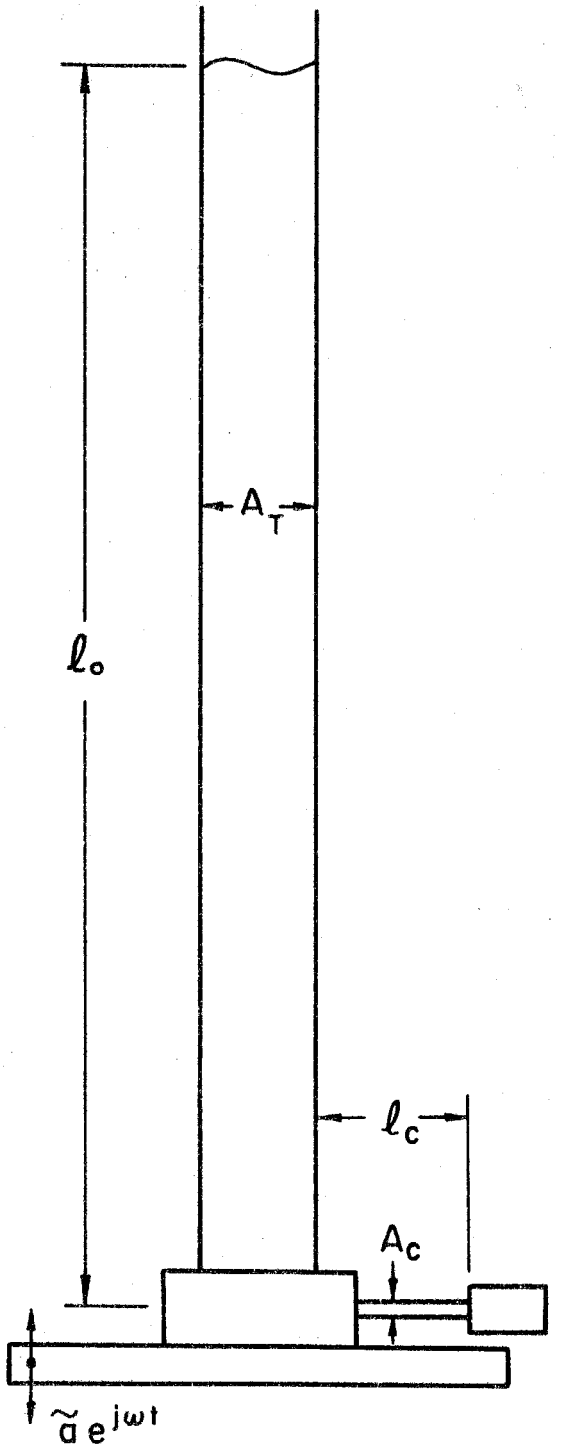

Fig. A.1 Schematic of dynamic pressure transducer calibration facility.

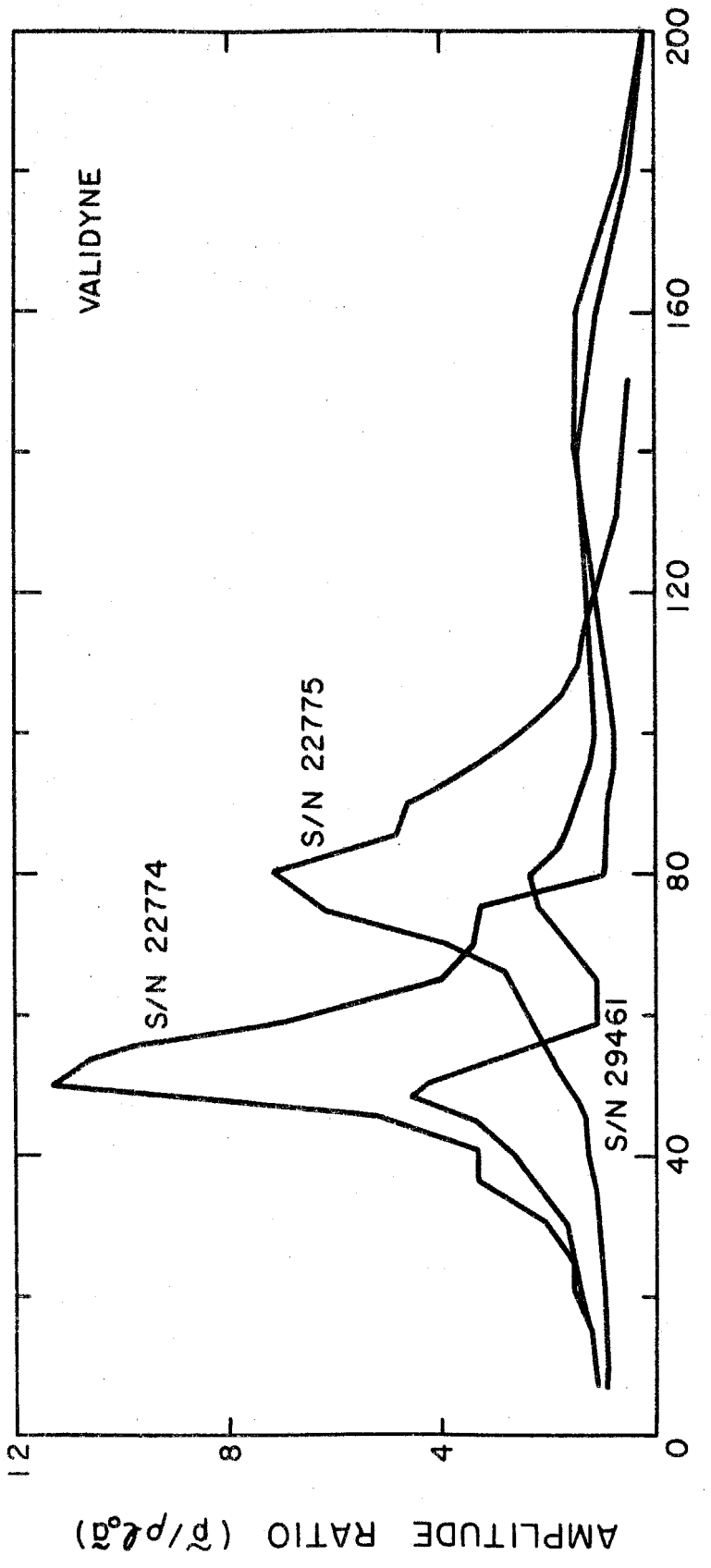

Fig. A.2 Amplitude response of the Validyne Model DP15 pressure transducers to imposed sinusoidal pressure fluctuations.

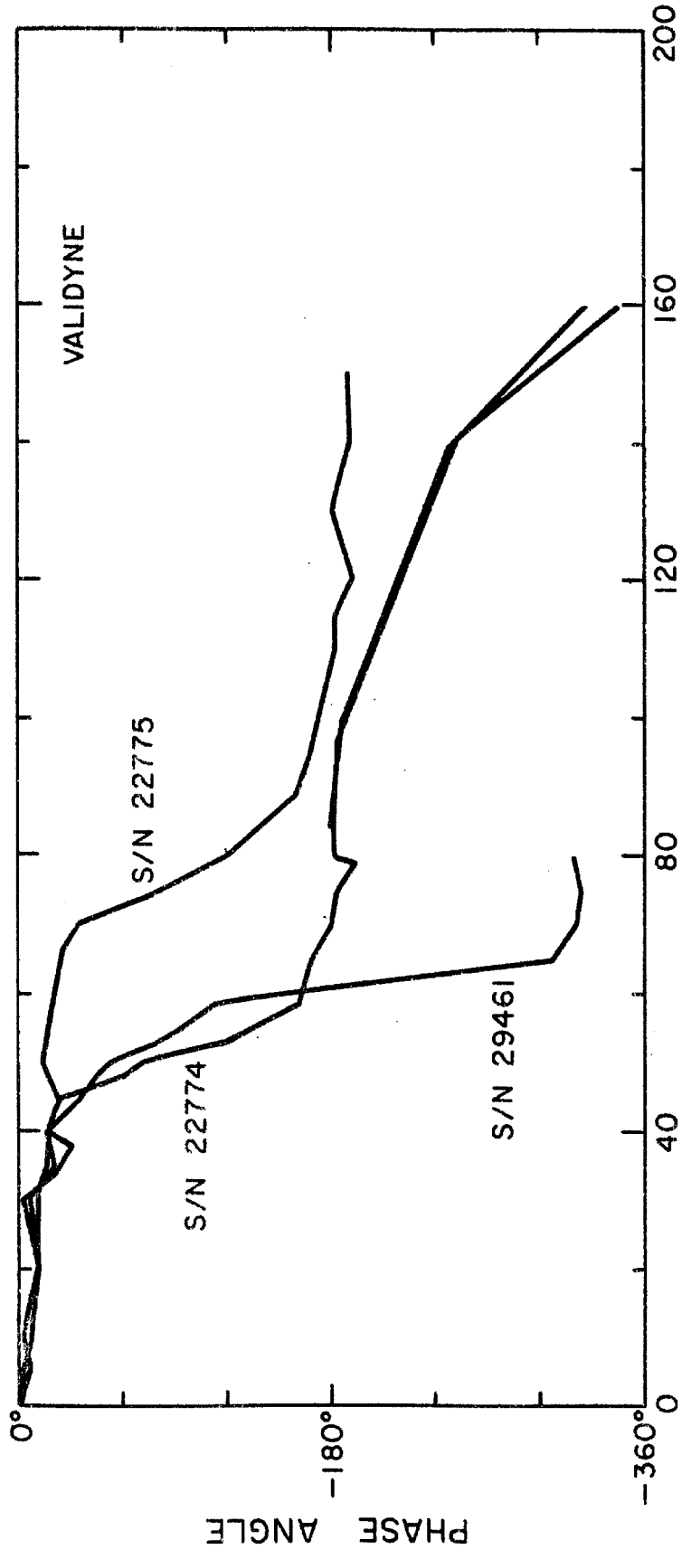

Fig. A.3 Phase shift associated with the dynamic properties of the Validyne pressure transducers and their connections.

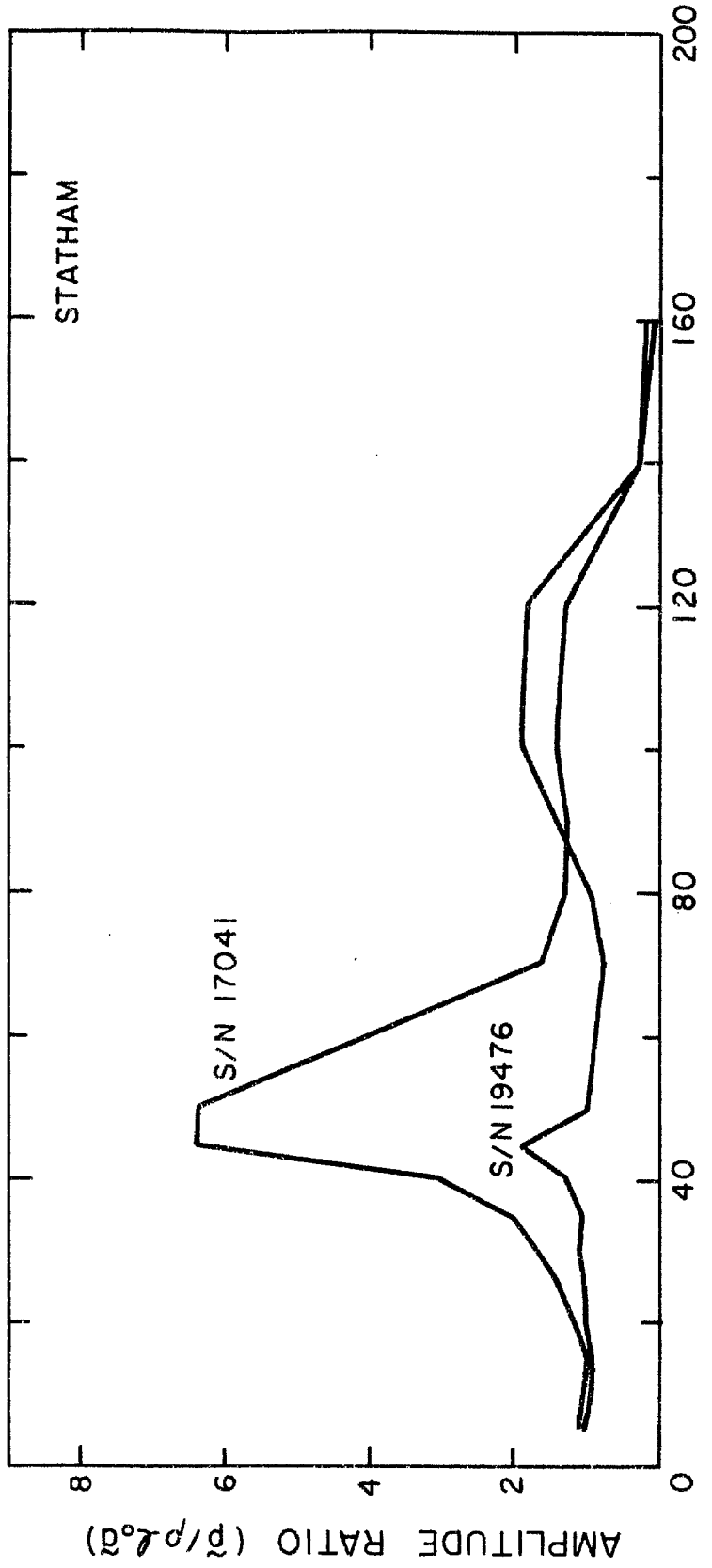

Fig. A.4 Amplitude response of the Statham Model PA822 pressure transducers to imposed sinusoidal pressure fluctuations.

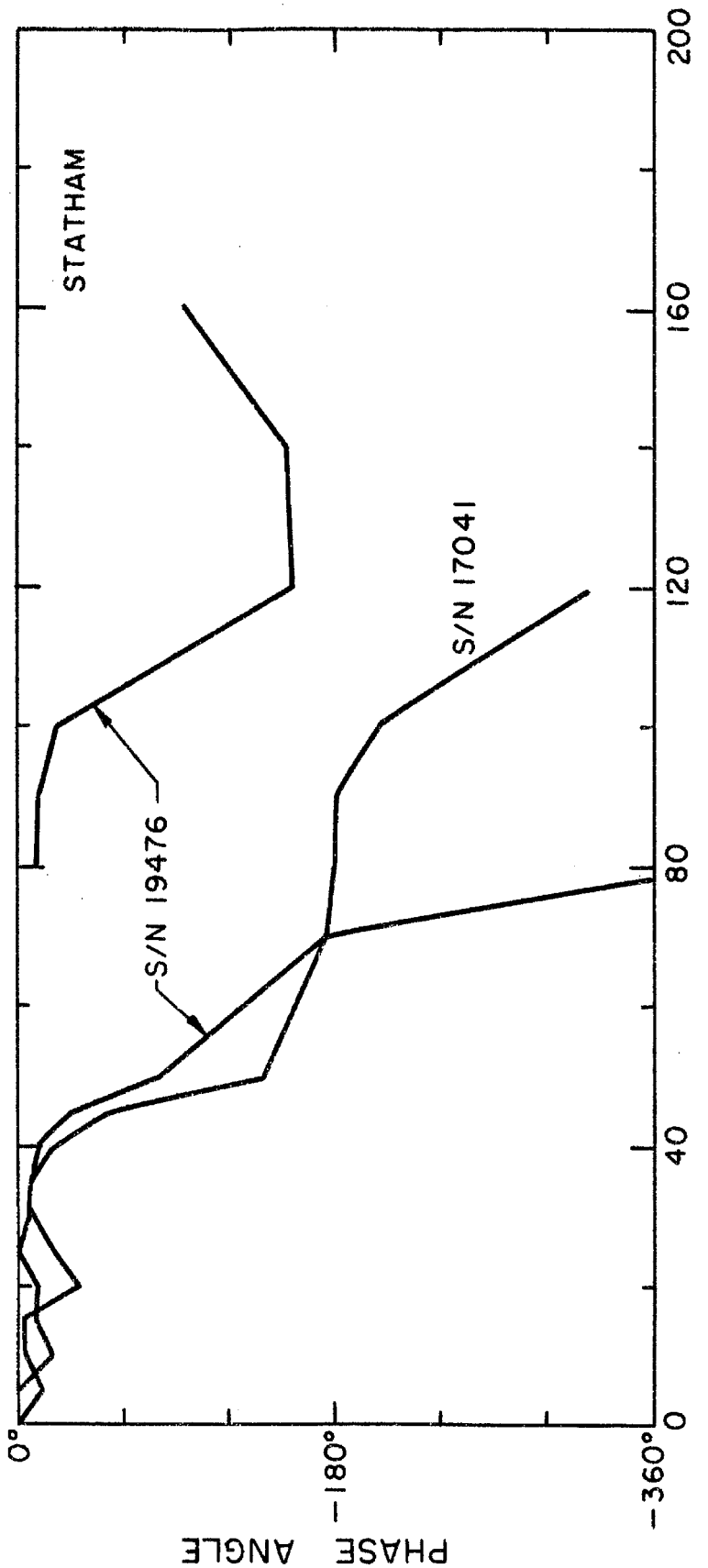

Fig. A.5 Phase shift associated with the dynamic properties of the Statham pressure transducers and their connections.

APPENDIX B
SYSTEM IMPEDANCES

As mentioned in Chapter 4, the inlet and discharge lines are dynamically modeled as impedances. An impedance is defined by

$$I = \frac{\tilde{\Delta p}}{\tilde{m}} \tag{B.1}$$

This requires the measurement of three fluctuating quantities: the entrance and exit pressures and a mass flow rate. The impedances are complex quantities. The following convention will be used to represent these impedances, i.e.

$$I = \mathcal{R} + j\omega\mathcal{L} \quad . \tag{B.2}$$

The real part of the impedance, $\mathcal{R}$, represents resistive contributions and the imaginary part, $\mathcal{L}$, the inertance contributions.

Besides the standard transfer function instrumentation, another Statham pressure transducer was mounted on the tank between the fluctuators. This provided the other necessary pressure measurement. The oscillations were generated by the fluctuators. When determining the downstream system impedance, the upstream fluctuator was used and vice versa.

Data were obtained at seven frequencies ranging from 4 to 42 Hz under non-cavitating conditions. After each set of data, the system configuration was modified so as to alter the value of the system impedance. The impedance of the inlet line was changed by varying the static position of the upstream fluctuator components. The "silent" throttle valve was used to vary the discharge line impedance. The

data were reduced in exactly the same manner as the transfer function data. Each data signal was cross-correlated against a reference sine wave to obtain its in-phase and quadrature components. After applying all the necessary calibrations and corrections to the data, the impedance was calculated as indicated by Eq. (B.1).

The resistance, $\mathcal{R}$, and the inertance, $\mathcal{L}$, of the impedances thus obtained are presented in Figs. B.1—B.4. Figures B.1 and B.2 correspond to the original system configuration pictured in Fig. 2.1. Figures B.3 and B.4 correspond to the modified version of the DPTF, Fig. 2.2.

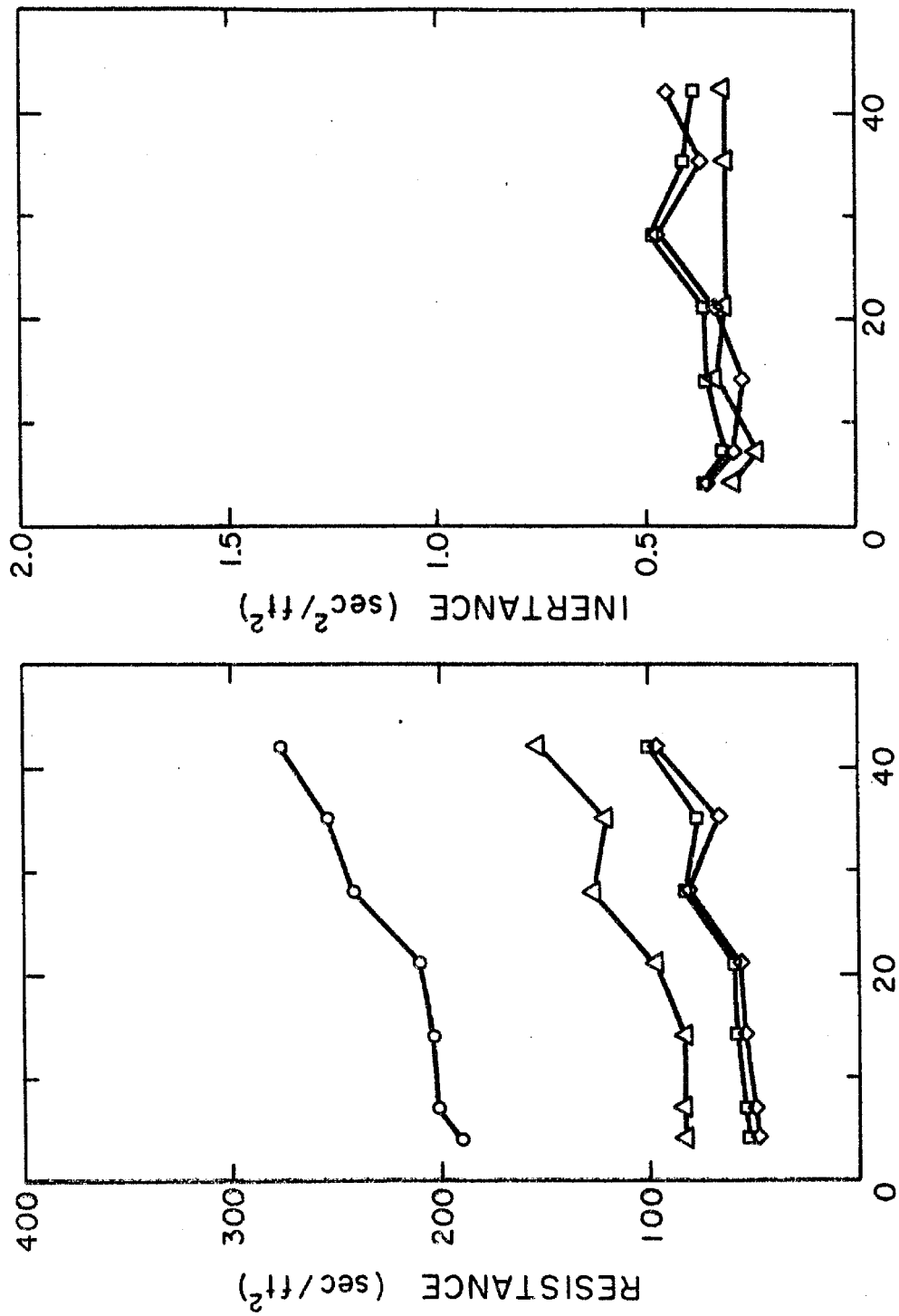

Fig. B.1 Resistance and inertance of inlet line (see Fig. 4.1) of original configuration of DPTF (Fig. 2.1) for different static positions of the fluctuator components. The data shown are for the slots open and 10% (O), 40% (Δ), 70 % (□) and 100% (◇) of the sintered bronze available for through flow.

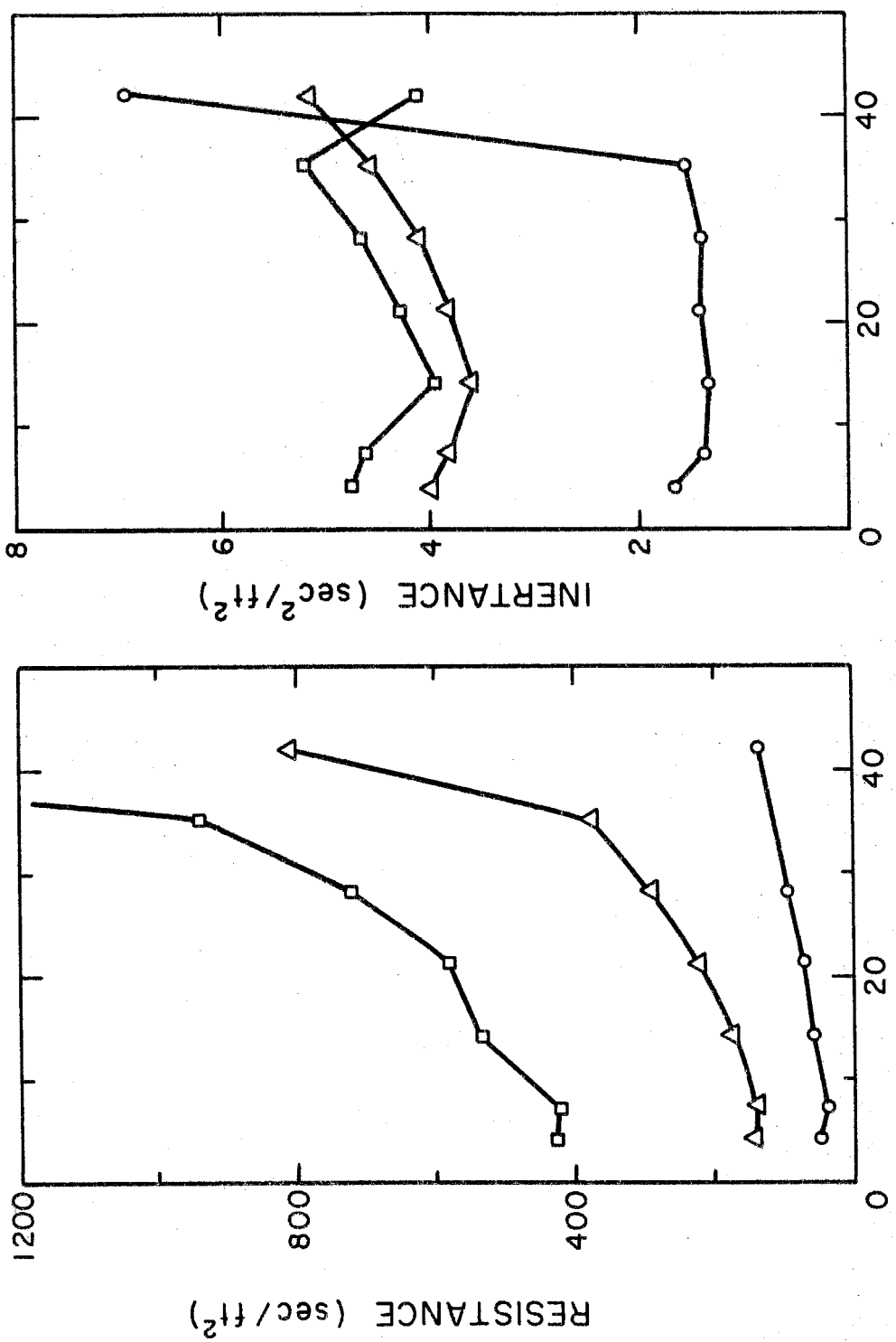

Fig. B.2 Resistance and inertance of discharge lines (see Fig. 4.1) of original configuration of DPTF (Fig. 2.1) for different settings of the silent throttle valve: high (□), medium (△) and low (○).

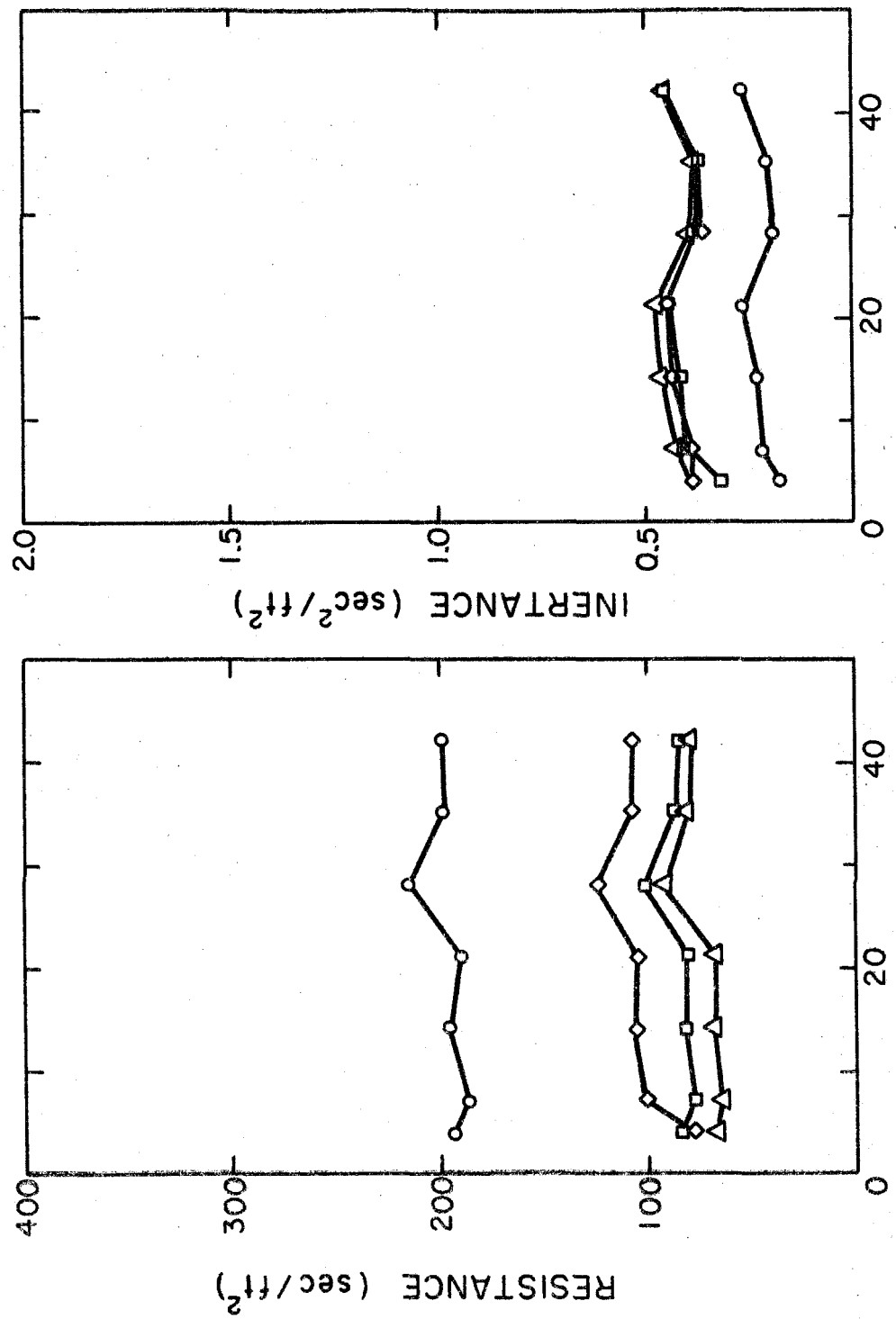

Fig. B.3 Resistance and inertance of inlet line after modification to DPTF (Fig. 2.2) for different static positions of the fluctuator components. The data shown are for the slots open and 0% (◇), 50% (□), 80% (△) and 100% (○) of the sintered bronze available for through flow.

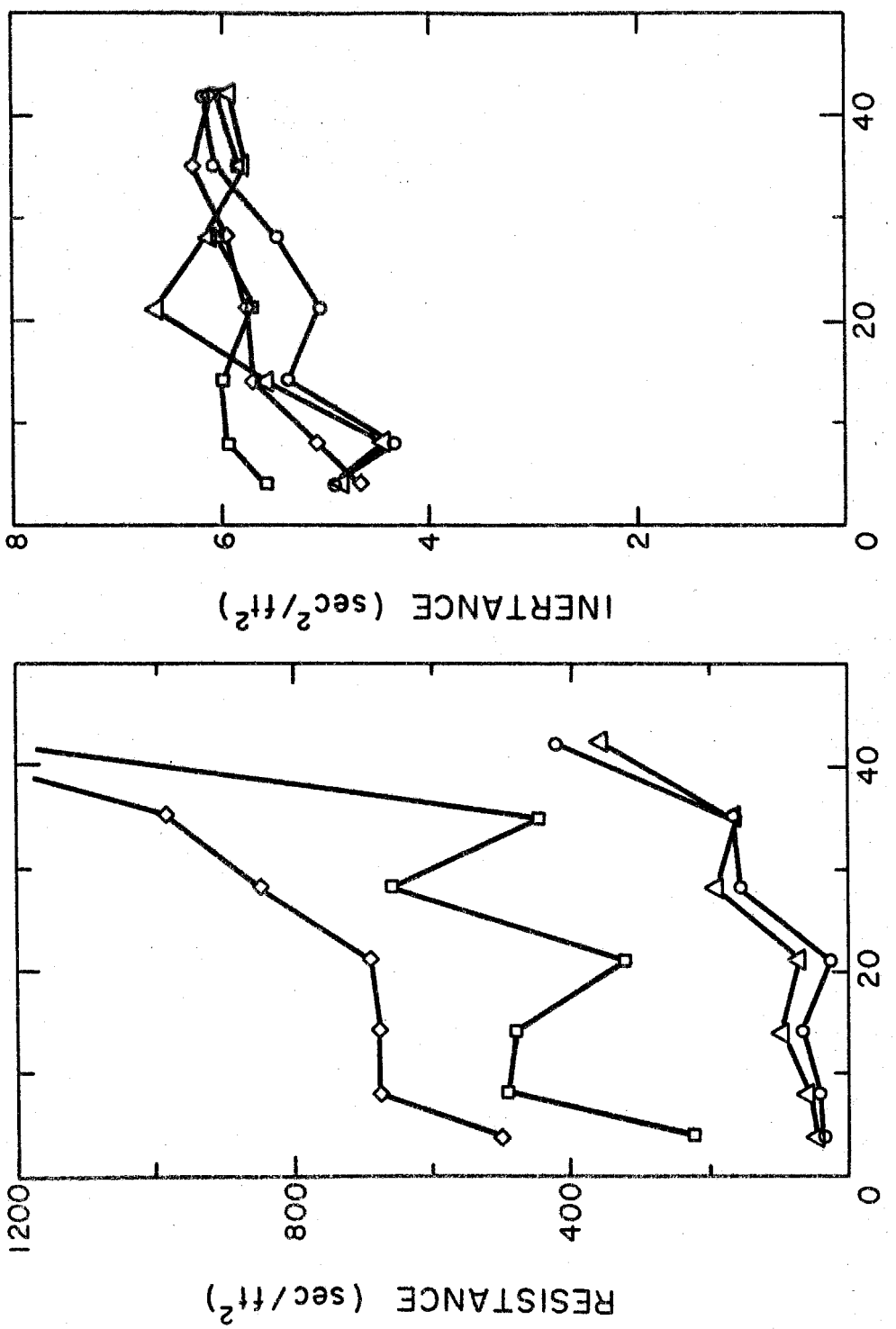

Fig. B.4 Resistance and inertance of discharge line after modifications to DPTF (Fig. 2.2) for different settings of the silent throttle valve: 0% (○), 17% (△), 50% (□), and 67% (◇) of maximum throttle setting.

APPENDIX C
INLET VELOCITY PROFILES

C.1 Test Procedures

The mean or steady velocity profiles in the inlet flow field of IMP6 at two axial locations were obtained by means of a wedge probe and a total head probe. These probes were connected to manometers via relatively long connecting lines. The inertia of the fluid in the lines effectively smoothed or averaged out any time dependent or non-axi-symmetric structure in the flow.

A radial traverse with the wedge probe was first performed to determine the flow angle. Once the angle of the flow was known, a radial traverse with the total head probe at the flow angle was performed. The data obtained from the total head probe test were stagnation pressures, $h(r)$, referenced to an upstream pressure, p_∞. The form of this measurement is expressed in Eq. C.1.

$$h(r) = p(r) + \frac{1}{2}\rho \, |V(r)|^2 - p_\infty \qquad (C.1)$$

where

$p(r)$ = radial pressure distribution

$|V(r)|$ = magnitude of the velocity vector.

In terms of the flow angle, $\gamma(r)$, and $|V(r)|$, the axial and swirl velocities, w and v, are defined by

$$v(r) = |V(r)| \sin\gamma(r)$$

and

$$w(r) = |V(r)| \cos\gamma(r) \qquad (C.2)$$

C.2 Data Reduction

It was further assumed that the inlet flow field was in a state of radial equilibrium. The condition of radial equilibrium is expressed in Eq. (C.3).

$$\frac{dp(r)}{dr} = \rho \frac{v^2(r)}{r} \tag{C.3}$$

Taking the derivative of Eq. (C.1) and substituting from Eq. (C.3) results in

$$\frac{dh(r)}{dr} = \rho \frac{|V(r)|^2 \sin^2 \gamma(r)}{r} + \frac{1}{2} \rho \frac{d}{dr} |V(r)|^2 \quad . \tag{C.4}$$

This equation can be used directly to calculate $|V(r)|$ through finite difference techniques. Alternately, Eq. (C.4) can be put into the following form:

$$\frac{\rho}{2} \frac{d}{dr} \left[G(r) |V(r)|^2 \right] = \frac{dh(r)}{dr} G(r) \tag{C.5}$$

where

$$G(r) = e^{2 \int_0^r \frac{\sin^2 \gamma(\mathcal{T})}{\mathcal{T}} d(\mathcal{T})}$$

Integrating this equation yields the required result:

$$|V(r)|^2 = \frac{2}{\rho G(r)} \int_0^r G(\mathcal{T}) \frac{dh(\mathcal{T})}{d\mathcal{T}} d\mathcal{T} + \frac{|V(0)|^2}{G(r)} \quad . \tag{C.6}$$

To use Eq. (C.6), an estimate of the centerline velocity must be made. This estimate is refined by comparing the calculated mass flow rate to that obtained with the turbine flow meter. The axial and swirl velocity profiles are then calculated from Eq. (C.2).

APPENDIX D
INERTANCE AND COMPLIANT BACKFLOW MODELS

D.1 Inertance Model

The linear inertance model is the simplest representation of an unsteady flow in a pipe. In this model, the flow within the pipe is assumed to be one-dimensional, inviscid and incompressible. The inertance model solely accounts for the pressure fluctuations produced by the acceleration of the fluid within the pipe. Under the one-dimensional and incompressible flow assumptions, continuity considerations require that

$$\frac{\partial w^*}{\partial z^*} = 0 \quad . \tag{D.1.1}$$

The equation of motion in the axial direction then reduces to

$$\frac{\partial w^*}{\partial t^*} = -\frac{1}{\rho}\frac{\partial p^*}{\partial z^*} \quad . \tag{D.1.2}$$

From Eqs. (D.1.1) and (D.1.2), it is apparent that the steady mean flow velocity, W_o, and pressure, P_o, are constants and not functions of the axial coordinate. Before linearizing these two equations by superimposing small amplitude harmonic perturbations on the steady mean flow, it is convenient to non-dimensionalize these relations. The length scale in this flow model is the radius of the cylindrical pipe, R; and the characteristic velocity is taken to be W_o. The corresponding time and pressure scales are R/W_o and ρW_o^2, respectively. The linearized equations of motion are

$$\frac{\partial \tilde{w}}{\partial z} = 0 \tag{D.1.3}$$

and

$$j\Omega \tilde{w} = -\frac{\partial \tilde{p}}{\partial z} \tag{D.1.4}$$

where

$$w = 1 + \tilde{w} e^{j\Omega t}$$

$$p = \varphi_o + \tilde{p}\, e^{j\Omega t}$$

Equation (D.1.3) requires that

$$\tilde{w}(z) = \tilde{w}_\infty \tag{D.1.5}$$

Integrating Eq. (D.1.4) and applying the boundary condition that $\tilde{p}(z=o) = \tilde{p}_\infty$ results in the following expression.

$$\tilde{p}(z) = \tilde{p}_\infty - j\Omega z \tilde{w}_\infty \tag{D.1.6}$$

This expression can now be used to compare or predict the pressure field at the inlet of the inducer given data concerning the amplitude of the pressure and mass flow rate fluctuations far upstream and the relative phase difference between these quantities.

D.2 Compliant Backflow Model

The simple inertance model can be extended to include the compressibility effects of the cavitation in the backflow jet. The cavitation shall be assumed to form a circumferentially symmetric layer of thickness $\delta^*(z,t)$ and length L_v^* as illustrated in Fig. D.1. The length of this compliant backflow region can be related to the mean flow rate. The thickness of the vapor layer will be assumed small (i.e. $\delta = \delta^*/R << 1$). The cavitation will also be assumed to respond

to local pressure fluctuations as a simple compliance. Thus, by definition, the cavitation responds to pressure fluctuations as indicated in Eq. (D.2.1).

$$\frac{\partial v^*}{\partial t^*} = -C\frac{\partial p^*}{\partial t^*} \tag{D.2.1}$$

where

v^* = volume of cavitation region

C = compliance

In terms of the compliant layer thickness, equation (D.2.1) reduces to

$$\frac{\partial \delta^*}{\partial t^*} = -\varkappa^* \frac{\partial p^*}{\partial t^*} \tag{D.2.2}$$

where

$\varkappa^*$ = modified compliance coefficient.

In addition, the fluid outside of this region will be considered inviscid and incompressible.

Since the thickness of the compliant layer is small, the steady mean flow velocity, W_o, and pressure, P_o, are again constants independent of the axial coordinate. The other equations governing this flow model are

$$\frac{\partial}{\partial z^*}(w^* A^*) = \pi \frac{\partial}{\partial t^*}\left(R^2 - (R - \delta^*)^2\right) \tag{D.2.3}$$

and

$$\frac{\partial w^*}{\partial t^*} + w^* \frac{\partial w^*}{\partial z^*} = -\frac{1}{\rho}\frac{\partial p^*}{\partial z^*} \tag{D.2.4}$$

where

$$A^* = \pi(R - \delta^*)^2 \quad .$$

Before linearizing the model by superimposing small harmonic perturbations on the velocity and pressure fields, these relations can be non-dimensionalized in the same manner as Section D.1. The resulting set of linear equations which describe the flow are

$$\tilde{\delta} = -\varkappa \tilde{p} \tag{D.2.5}$$

$$j\Omega\tilde{\delta} + \frac{\partial \tilde{\delta}}{\partial z} = \frac{1}{2}\frac{\partial \tilde{w}}{\partial z} \tag{D.2.6}$$

and

$$j\Omega\tilde{w} + \frac{\partial \tilde{w}}{\partial z} = -\frac{\partial \tilde{p}}{\partial z} \tag{D.2.7}$$

where

$$w(z,t) = 1 + \tilde{w}(z)\, e^{j\Omega t}$$

$$p(z,t) = \mathcal{P}_o + \tilde{p}(z)\, e^{j\Omega t}$$

$$\delta(z,t) = \tilde{\delta}(z)\, e^{j\Omega t}$$

This set of equations can be further simplified by assuming an exponential dependence upon the axial coordinate (i.e. $\tilde{w}(z) \sim e^{\alpha z}$). Upon substitution and after further manipulation, the following dispersion relation is obtained.

$$\alpha^2\left(2 - \frac{1}{\varkappa}\right) + 4j\Omega\alpha - 2\Omega^2 = 0 \tag{D.2.8}$$

The solutions to this dispersion relation are

$$\alpha_{1,2} = \left(\frac{-1 \pm \Lambda}{1 - \Lambda^2}\right) j\Omega \tag{D.2.9}$$

where

$$\Lambda^2 = \frac{1}{2\varkappa} \quad .$$

Since the α's are purely imaginary, these harmonic perturbations represent two traveling waves. The non-dimensional speeds and wave lengths are given by Ω/α and $2\pi/\alpha$, respectively.

The two as yet unknown amplitudes of these waves are determined if the fluctuating pressure and velocity are known or specified at some location. The solution in terms of the fluctuating pressure and velocity, $\tilde{p}_1$ and $\tilde{w}_1$, at $z=0$ is given by Eqs. (D.2.10) and (D.2.11).

$$\tilde{w}(z) = \frac{\tilde{w}_1}{2}\left(e^{\alpha_1 z} + e^{\alpha_2 z}\right) - \varkappa \tilde{p}_1 \left[(1-\Lambda)\, e^{\alpha_1 z} + (1+\Lambda)\, e^{\alpha_2 z}\right] \qquad (D.2.10)$$

$$\tilde{p}(z) = \frac{\tilde{w}_1}{4\varkappa\Lambda}\left(e^{\alpha_1 z} - e^{\alpha_2 z}\right) - \frac{\tilde{p}_1}{2\Lambda}\left[(1-\Lambda)\, e^{\alpha_1 z} - (1+\Lambda) e^{\alpha_2 z}\right] \qquad (D.2.11)$$

The amplitude and relative phase of the fluctuating pressure and velocity at $z=0$, $\tilde{p}_1$ and $\tilde{w}_1$, can be related to the far upstream pressure and velocity measurements, $\tilde{p}_\infty$ and $\tilde{w}_\infty$, by use of the results of Section D.1. The result of this calculation is the following relation.

$$\tilde{p}_1 = \tilde{p}_\infty - j\Omega L \tilde{w}_\infty \qquad (D.2.12)$$

and

$$\tilde{w}_1 = \tilde{w}_\infty \qquad (D.2.13)$$

where

L = distance between the far upstream pressure measurement and the upstream end of the cavitation region.

Equations (D.2.10)–(D.2.13) can now be used to calculate an axial pressure distribution based upon measurements of the far upstream pressure and velocity fluctuations and various estimates of the compliance and length of the vapor layer.

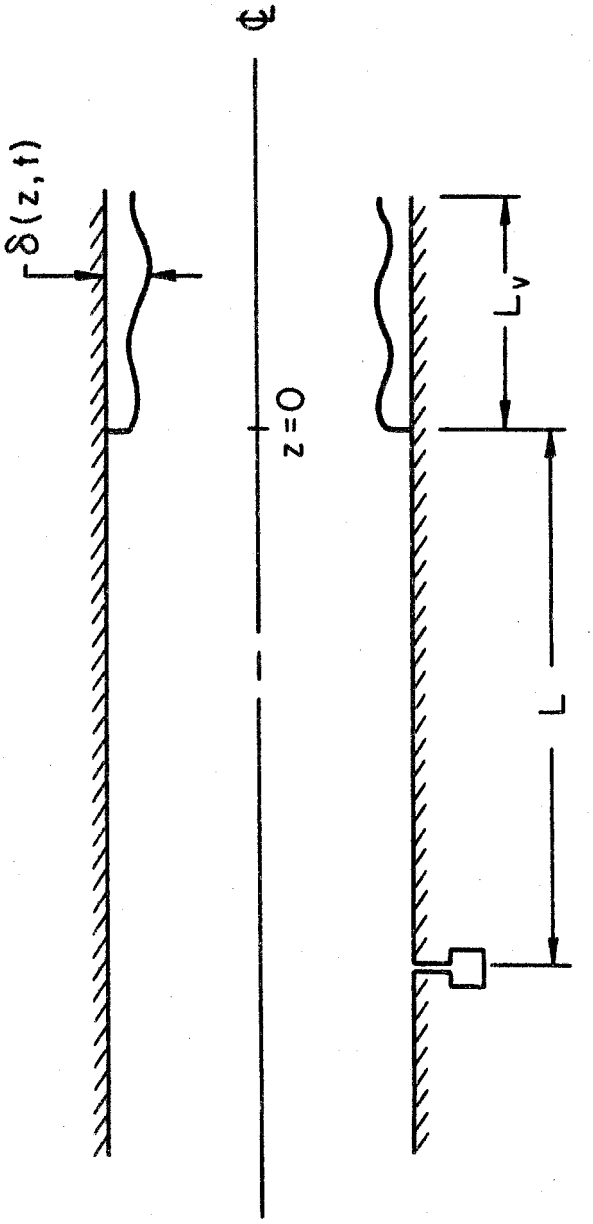

Fig. D.1 Flow model used in compliant backflow model.

APPENDIX E
SWIRLING INLET FLOW MODEL

E.1 Model of Mean Flow

The dynamics of the inlet flow field is thought to influence and control the occurrence of auto-oscillation. The mean flow which is known to be purely axial and nearly uniform far upstream becomes highly rotational and non-uniform in the neighborhood of the inlet to the inducer. The flow is further complicated by the extensive cavitation that occurs due to the upstream penetration of the tip clearance jet. In addition, this backflow jet rolls up into vortex sheets which causes extensive mixing to occur. Since the mechanics of the momentum and vorticity transport processes of this flow are not well understood, it is necessary to simplify the mean flow field. For the purpose of this model, the mixing provided by the vortex sheets and the compliance provided by the cavitation in the backflow will be neglected. In addition, the flow will be assumed inviscid, incompressible and axi-symmetric. Under the above restrictions, the following continuity and momentum equations define the steady mean flow.

$$\frac{1}{r^*}\frac{\partial}{\partial r^*}(r^* U) + \frac{\partial W}{\partial z^*} = 0$$

$$U\frac{\partial U}{\partial r^*} + W\frac{\partial U}{\partial z^*} - \frac{V^2}{r^*} = -\frac{1}{\rho}\frac{\partial P}{\partial r^*} \qquad \text{(E.1.1)}$$

$$U\frac{\partial V}{\partial r^*} + W\frac{\partial V}{\partial z^*} + \frac{UV}{r^*} = 0$$

$$U\frac{\partial W}{\partial r^*} + W\frac{\partial W}{\partial z^*} = -\frac{1}{\rho}\frac{\partial P}{\partial z^*}$$

where

(U, V, W) are the velocity components in the (r^*, θ^*, z^*) directions.

It is necessary to further restrict the class of flows. This is accomplished by assuming that the axial velocity, W, does not depend upon the axial coordinate, z^*. This restricts the allowable class of flows to

$$W = W(r^*) = W_o + W_1(r^*) \quad . \tag{E.1.2}$$

Since the radial velocity, U, must vanish at $r^* = 0$, the continuity equation and the azimuthal equation of motion require that

$$U = 0 \tag{E.1.3}$$

and

$$V = V(r^*) \quad . \tag{E.1.4}$$

The exact functional dependence of $V(r^*)$ and $W(r^*)$, however, is not fixed by either the continuity or momentum equations.

The above velocity field constitutes the proposed model of the mean inlet flow. Although the actual flow field is considerably more complicated, it is hoped that this model contains the essential features important to the dynamics.

E.2 Perturbation Analysis

To investigate the linear dynamic behavior of the specified steady flow, a small amplitude harmonic perturbation to the velocity and pressure fields is superimposed upon the steady flow field. Before linearizing the unsteady, inviscid, incompressible, axi-symmetric

Navier-Stokes equations, it is useful to non-dimensionalize these equations. The length scale in the assumed flow model is the radius of the cylindrical pipe, R ; and the characteristic velocity is taken from Eq. (E.1.2) as W_o . The corresponding characteristic time and pressure scales are R/W_o and ρW_o^2, respectively. Substituting and retaining only terms to first order in the perturbation quantities yields the following set of linearized continuity and momentum equations.

$$\frac{1}{r}\frac{\partial}{\partial r}(r\hat{u}) + \frac{\partial \hat{w}}{\partial z} = 0$$

$$j\Omega\hat{u} + [1+\mathbb{w}(r)]\frac{\partial \hat{u}}{\partial z} - \frac{2\mathbb{V}(r)\hat{v}}{r} = -\frac{\partial \hat{p}}{\partial r} \qquad \text{(E.2.1)}$$

$$j\Omega\hat{v} + [1+\mathbb{w}(r)]\frac{\partial \hat{v}}{\partial z} + \frac{1}{r}\frac{d}{dv}[r\mathbb{V}(r)]\hat{u} = 0$$

$$j\Omega\hat{w} + [1+\mathbb{w}(r)]\frac{\partial \hat{w}}{\partial z} + \hat{u}\frac{d\mathbb{w}(r)}{dr} = -\frac{\partial \hat{p}}{\partial z}$$

where

$$u(r,z,t) = \hat{u}(r,z)e^{j\Omega t}$$

$$v(r,z,t) = \mathbb{V}(r) + \hat{v}(r,z)e^{j\Omega t}$$

$$w(r,z,t) = 1 + \mathbb{w}(r) + \hat{w}(r,z,)e^{j\Omega t} + \chi\, e^{j\Omega t}$$

$$p(r,z,t) = \mathcal{P}(r) + \hat{p}(r,z)e^{j\Omega t} - j\Omega z\chi\, e^{j\Omega t} + Ye^{j\Omega t}$$

and

$$0 \leq r = r^*/R \leq 1$$

$$-\infty < z = z^*/R \leq 0 \ .$$

The term $\chi e^{j\Omega t}$ in the perturbation axial velocity field will be referred to as an inertance wave.

The above relations, Eq. (E.2.1), are simplified further by assuming an exponential dependence on the axial coordinate. The

perturbation velocity and pressure fields now represent traveling waves. Substitution of this separated form of the perturbation quantities allows separable solutions of equations (E.2.1). The result is four coupled ordinary differential equations for the four as yet unknown radial distributions of the perturbation pressure and velocities. This set of four equations can be reduced to the following second order ordinary differential equation involving only the radial distribution of the radial velocity.

$$r^2 \frac{d^2\tilde{u}}{dr^2} + r \frac{d\tilde{u}}{dr} + \left\{ \alpha^2 r^2 - 1 + \frac{2\alpha^2 V(r)}{j\Omega + \alpha[1+W(r)]} \frac{d}{dr}[rV(r)] \right.$$

$$\left. + \frac{\alpha}{j\Omega + \alpha[1+W(r)]} \frac{1}{r}\left[\frac{dW(r)}{dr} - \frac{d^2W(r)}{dr^2}\right] \right\} \tilde{u} = 0 \qquad \text{(E.2.2)}$$

where

$$\hat{u}(r,z) = \tilde{u}(r)e^{\alpha z}$$

The radial velocity is subject to the boundary conditions specified in Eq. (E.2.3).

$$\tilde{u}(0) = 0$$

$$\tilde{u}(1) = 0 \qquad \text{(E.2.3)}$$

The radial distributions of the other perturbation quantities are calculated from $\tilde{u}(r)$. The process of elimination which generated Eq. (E.2.2) also yielded the following relations.

$$\tilde{v}(r) = \frac{-1}{j\Omega + \alpha[1+\mathbb{w}(r)]} \frac{1}{r} \frac{d}{dr}[r\mathbb{V}(r)]\tilde{u}(r)$$

$$\tilde{w}(r) = \frac{-1}{\alpha r} \frac{d}{dr}[r\tilde{u}(r)] \qquad \text{(E.2.4)}$$

$$\tilde{p}(r) = \frac{j\Omega + \alpha[1+\mathbb{w}(r)]}{\alpha^2} \left\{ \frac{1}{r} \frac{d}{dr}[r\tilde{u}(r)] - \frac{\alpha}{j\Omega + \alpha[1+\mathbb{w}(r)]} \frac{d\mathbb{w}(r)}{dr} \tilde{u}(r) \right\}$$

where

$$\hat{v}(r,z) = \tilde{v}(r)e^{\alpha z}$$

$$\hat{w}(r,z) = \tilde{w}(r)e^{\alpha z}$$

$$\hat{p}(r,z) = \tilde{p}(r)e^{\alpha z}$$

It is apparent that this procedure has led to an eigenvalue problem with eigenvalues, α, and eigenvectors, $\tilde{u}(r;\alpha)$. An infinite hierachy of solutions exist which are distinguished by the number of internal zeros the eigenvector possesses. Due to the fact that the problem is linear, it is sufficient to consider only one eigenvalue–eigenvector pair at a time. Hence, only those α's corresponding to $\tilde{u}(r;\alpha)$ with no internal zeros shall be considered.

To continue the analysis further, it becomes necessary to specify the functional form of the steady axial and swirl velocity distributions, $\mathbb{w}(r)$ and $\mathbb{V}(r)$. For the special case of rigid body rotation and a uniform axial velocity profile, an explicit solution exists. For this special case, $\mathbb{w}(r) = 0.0$ and $\mathbb{V}(r) = Nr$, the acceptable solution to Eq. (E.2.2) is

$$\tilde{u}(r;\alpha) = J_1\left(\alpha\sqrt{1+\frac{4N^2}{(j\Omega+\alpha)^2}}\; r\right) \quad . \qquad \text{(E.2.5)}$$

The eigenvalues, α, are determined by the boundary conditions at the wall, $r=1$; and they satisfy the following quartic equation.

$$\alpha^4 + 2j\Omega\alpha^3 + (4N^2 - \Omega^2 - \eta^2)\alpha^2 - 2j\Omega\eta^2\alpha + \eta^2\Omega^2 = 0 \qquad \text{(E.2.6)}$$

where

η = first zero of Bessel function $J_1 = 3.832$.

The alphas are independent functions of the swirl and frequency parameters, N and Ω. The explicit dependence upon these parameters will be explained in Section E.3.

The form of Eq. (E.2.2) suggests that alternate choices of the steady velocity profiles be of the form

$$V(r) = Nr^n$$

and

$$W(r) = Kr^k \quad . \qquad \text{(E.2.7)}$$

As long as k and n are selected from the set of positive integers, a solution for $\tilde{u}(r)$ can be obtained in terms of a power series such as

$$\tilde{u}(r) = \sum_{i=-\infty}^{\infty} \beta_i r^i \quad . \qquad \text{(E.2.8)}$$

The coefficients of the power series, β_i, are determined by the constraints (i.e. boundary conditions) at $r=0$ and $r=1$ previously specified in Eq. (E.2.3). The first of these boundary conditions forces

$$\beta_i \equiv 0 \quad ; \quad \text{for all } i \leq 0 \tag{E.2.9}$$

The remaining coefficients are prescribed by the differential equation for $\tilde{u}(r)$, Eq. (E.2.2), in the usual manner; and they are functions of parameters k, K, n, N and Ω. The m^{th} term in the recursion relation for the β_i's is

$$\beta_m = 0 \quad ; \quad \text{if } m \text{ is even}$$

and

$$\beta_m = \frac{-1}{(m^2-1)(j\Omega+\alpha)^2} \left\{ \begin{array}{l} \alpha^2(j\Omega+\alpha)^2\,\beta_{m-2} + \\ 2\alpha^3 K(j\Omega+\alpha)\,\beta_{m-k-2} \end{array} \right. \tag{E.2.10}$$

$$+ [2(m-k-1)(m-k+1) + k(k-2)]\,\alpha K(\alpha + j\Omega)\,\beta_{m-k}$$

$$+ [(m-2k-1)(m-2k+1) + k(k-2)]\,\alpha^2 K^2\,\beta_{m-2k}$$

$$\left. + \alpha^4 K^2\,\beta_{m-2k-2} + 2(n+1)\,\alpha^2 N^2\,\beta_{m-2n} \right\} \quad ; \quad \text{if m is odd} .$$

Application of the boundary condition at $r = 1$ determines the eigenvalues, α, and the corresponding eigenvectors, $\tilde{u}(r;\alpha)$. For specific choices of the parameters k, K, n, N and Ω, the values of α corresponding to eigenvectors, $\tilde{u}(r;\alpha)$, with no internal zeros were calculated numerically. The numerical search routine used Newton's method assisted by the method of steepest descent (see Ref. [45]). As in the special case of rigid body rotation, four eigenvalues were located for each mode. The convergence of the numerical scheme has been confirmed by comparison to the results obtained from Eq. (E.2.6) for the special case of rigid body rotation and uniform axial velocity. The agreement between the alphas obtained from Eq. (E.2.6) and via

the search routine was remarkable. There was no problem in achieving an agreement to four significant figures.

Once the eigenvalues, α, and corresponding eigenvectors, $\tilde{u}(r;\alpha)$, are determined, the radial distribution of the other perturbation field quantities are readily computed by means of Eq. (E.2.4).

The linear perturbation analysis is now complete except for the four as yet undetermined constants – the leading coefficient in the power series. The value of these constants are fixed by conditions specified at either $z = 0$ or far upstream.

E.3 The Eigenvalues

E.3.1 Special Case of Rigid Body Rotation

The four eigenvalues for the special case of rigid body rotation and uniform axial velocity are depicted in Fig. E.1. Their real and imaginary components have been plotted with respect to the swirl parameter, N, for a specific non-dimensional frequency, Ω. Several interesting observations are established by these curves. Of the four complex eigenvalues, two invariably have positive imaginary parts and two are negative. The imaginary component of the alphas determines both the wave number, or equivalently the wave length, and the wave speed. The non-dimensional wave speed is defined by

$$S = \frac{\Omega}{\text{Imag}\{\alpha\}} \quad ; \qquad (E.3.1)$$

and the non-dimensional wave number is defined by

$$\kappa = \frac{2\pi}{\lambda} = \text{Imag}\{\alpha\} \quad . \qquad (E.3.2)$$

The waves propogate upstream towards negative infinity in the axial direction if the imaginary part of alpha is positive. Consideration shall be restricted to only those disturbances (waves) which are generated by the inducer. This condition requires that the leading coefficient in the power series expansion for $\tilde{u}(r;\alpha)$ corresponding to alphas with negative imaginary parts to vanish. Hence, only those alphas with positive imaginary components, $\alpha(1)$ and $\alpha(2)$, need be considered further. The other useful piece of information to be gleaned from the imaginary component of the eigenvalues concerns the wave speed. The assumed form of the steady axial velocity profile indicates that unless the wave speed of the waves is greater than 1.0 the effective direction of propagation is downstream. Such a wave cannot effect the inlet flow and hence is unimportant to the dynamics of this flow field. The following equation spells out this criterion.

$$\text{Imag}\{\alpha\} \leq \Omega . \qquad \text{(E.3.3)}$$

Referring again to Fig. E.1, the eigenvalue $\alpha(2)$ does not satisfy this criterion for values of the swirl parameter greater than 5.5. Since the effective direction of propagation of these waves is downstream, waves corresponding to eigenvalue $\alpha(2)$ and swirl parameters greater than 5.5 will not be considered further.

The behavior of the real part of $\alpha(1)$ and $\alpha(2)$ is more complicated. For values of the swirl parameter, N, greater than 5.5, the real parts of $\alpha(1)$ and $\alpha(2)$ vanish. Below this critical value of 5.5, the real part of $\alpha(1)$ is positive and the real part of $\alpha(2)$ is negative. Thus, a wave possessing an eigenvalue with positive real

part, $\alpha(1)$, is attenuated as it propagates upstream. To prevent infinite perturbation velocity amplitudes within the flow field, those waves which are amplified as they propagate upstream (i.e. Real$\{\alpha\} < 0$) must be rejected. Therefore, waves corresponding to the eigenvalue $\alpha(2)$ and swirl parameters less than the critical value of 5.5 shall not be considered further since these waves are amplified as they propagate upstream.

The functional dependence upon the frequency of the oscillation is quite apparent in Fig. E.2. In Fig. E.2, $\alpha(1)$ has been plotted as a function of swirl intensity, N, for several frequencies. It is important to notice that the value of the critical swirl parameter is a monotonically increasing function of frequency. For values of N larger than the critical value, N_{CR}, the imaginary part of $\alpha(1)$ increases with frequency. Referring to Eq. (E.3.1), this trend corresponds to a reduction in wave speed with frequency. Below the critical value, N_{CR}, both the wave speed and rate of attenuation are increased with increasing frequency.

A graph of the critical value of swirl intensity plotted as a function of frequency appears in Fig. E.3. In the region above the curve, one wave (in addition to the inertance wave) propagates upstream without a change in amplitude. An attenuating wave propagates upstream for values of the swirl parameter which lie in the region below the curve.

A comparison between the special case of rigid body rotation and uniform axial velocity and other mean flow fields is given in the next section.

E.3.2 Other Mean Flow Velocity Profiles

As in the case of rigid body rotation described above, four eigenvalues exist for each mode for all other combinations of $V(r) = Nr^n$ and $W(r) = Kr^k$. The waves corresponding to two of these eigenvalues propagate downstream and are not considered further. One of the other two eigenvalues was eliminated for the same reasons that $\alpha(2)$ was eliminated previously.

A comparison of the critical swirl curve for the various mean flow profiles listed in Table E.1 is given in Figs. E.4a and b. In Fig. E.4a, the critical swirl intensity curve is shifted towards larger values of N with an increase in the curvature of the steady swirl velocity profile (i.e. an increase in n). The direction of the shift in the critical swirl intensity curve for non-uniformity in the steady axial velocity profile depends upon the sign of K as demonstrated in Fig. E.4b. A positive value of K leads to larger critical values; while the more physically appropriate negative value of K leads to a smaller value of the critical swirl intensity.

The variation in attenuation rate and wave speed with changes in the curvature of the steady swirl velocity profile are illustrated in Fig. E.5. As with the frequency dependence, the rate of attenuation is increased by an increase in the curvature of the swirl velocity profile. The wave speed is increased for $N<N_{CR}$ and reduced for $N>N_{CR}$

Non-uniformity in the steady axial velocity profile produces smaller variations as depicted in Fig. E.6. Negative values of K lead to a higher rate of attenuation and slower wave speeds for swirl intensities below the critical value. For $N>N_{CR}$, the wave speed of the disturbance is increased slightly.

E.4 Radial Distributions of Perturbation Pressure and Velocities

The radial distribution of the perturbation velocity and pressure fields are calculated from Eqs. (E.2.4) once $\alpha(1)$ has been determined. A typical example of the velocity and pressure profiles for a non-dimensional frequency of 4.0 is given in Figs. E.7 through E.10. The selected steady flow profiles were uniform axial velocity and a quadratic swirl velocity. For reference, the critical swirl intensity lies between 7.0 and 7.5.

E.5 Data Simulation

The axial distribution of the pressure fluctuations at the wall of the cylindrical pipe provides a means of verifying the analysis. However, the amplitudes of the inertance and perturbation waves have yet to be determined. To determine the relative amplitude of the perturbation wave with respect to the amplitude of the inertance wave, χ, a condition at some axial location must be applied. It shall be assumed that the unsteady flow field must remain parallel to the steady flow field at $z = 0$. This effectively defines the blade angle of the inducer assuming the flow remains tangent to the blades. This condition requires that

$$\frac{Nr^n + \tilde{v}(r)e^{(\alpha z + j\Omega t)}}{1.0 + Kr^k + \tilde{w}(r)e^{(\alpha z + j\Omega t)} + \chi e^{j\Omega t}} = \frac{Nr^n}{1.0 + Kr^k} \qquad (E.5.1)$$

Substituting for the perturbation axial and swirl velocities determines the relative amplitude of the leading coefficient in the power series expansion for $\tilde{u}(r; \alpha(1))$.

In order to determine the appropriate values for the unknown coefficients χ and Υ in Eq. (E.2.1) and hence the absolute amplitude of the perturbation wave, it is necessary to use the far upstream pressure and velocity measurements. These measurements will be used to define the absolute amplitude of the inertance wave. The perturbation wave is not involved in this calculation since the flow is both uniform and irrotational far upstream which results in a rapid attenuation (see Figs. E.6 and E.7) of the perturbation wave. If $\tilde{w}_\infty e^{j\Omega t}$ and $\tilde{p}_\infty e^{j\Omega t}$ represent the experimental velocity and pressure measurements taken at a distance L upstream of $z = 0$, then χ and Υ are defined as follows.

$$\chi = \tilde{w}_\infty$$

$$\Upsilon = \tilde{p}_\infty - j\Omega L \tilde{w}_\infty \qquad \text{(E.5.2)}$$

The fluctuating pressure field reduces to

$$p(r,z,t) = \tilde{p}(r)e^{(\alpha z + j\Omega t)} - j\Omega\tilde{w}_\infty(L+z)e^{j\Omega t} + \tilde{p}_\infty e^{j\Omega t} \quad . \qquad \text{(E.5.3)}$$

Both the phase and amplitude of the pressure fluctuations at the wall ($r = 1$) can be calculated from Eq. (E.5.3). The phase angle, Φ, of the pressure fluctuations at $r = 1.0$ is given by

$$\tan\Phi = \frac{\text{Imag}\left\{\tilde{p}(1)e^{\alpha z} + \tilde{p}_\infty - j\Omega\tilde{w}_\infty(L+z)\right\}}{\text{Real}\left\{\tilde{p}(1)e^{\alpha z} + \tilde{p}_\infty - j\Omega\tilde{w}_\infty(L+z)\right\}} \qquad \text{(E.5.4)}$$

E.6 Non-Axi-Symmetric Perturbations Analysis

It is also possible to investigate the dynamic behavior of the steady flow specified in Section E.1 to non-axi-symmetric perturbations. After relaxing the axi-symmetric assumption, the appropriate linearized, non-dimensional Navier-Stokes equations are

$$\frac{1}{r}\frac{\partial(r\hat{u})}{\partial r} + \frac{1}{r}\frac{\partial \hat{v}}{\partial \theta} + \frac{\partial \hat{w}}{\partial z} = 0$$

$$\frac{\partial \hat{u}}{\partial t} + \frac{V(r)}{r}\frac{\partial \hat{u}}{\partial \theta} - \frac{2V(r)\hat{v}}{r} + [1 + W(r)]\frac{\partial \hat{u}}{\partial z} = \frac{-\partial \hat{p}}{\partial r}$$

$$\frac{\partial \hat{v}}{\partial t} + \hat{u}\frac{dV(r)}{dr} + \frac{V(r)}{r}\frac{\partial \hat{v}}{\partial \theta} + \frac{\hat{u}\,V(r)}{r} + [1 + W(r)]\frac{\partial \hat{v}}{\partial z} = \frac{-1}{r}\frac{\partial \hat{p}}{\partial \theta}$$

$$\frac{\partial \hat{w}}{\partial t} + \hat{u}\frac{dW(r)}{dr} + \frac{V(r)}{r}\frac{\partial \hat{w}}{\partial \theta} + [1 + W(r)]\frac{\partial \hat{w}}{az} = \frac{-\partial \hat{p}}{\partial z} \qquad \text{(E.6.1)}$$

where

$$u = \hat{u}(r, \theta, z, t)$$
$$v = V(r) + \hat{v}(r, \theta, z, t)$$
$$w = 1 + W(r) + \hat{w}(r, \theta, z, t) + \chi\, e^{j\Omega t}$$
$$p = \mathcal{P}(r) + \hat{p}(r, \theta, z, t) - j\Omega z\, \chi\, e^{j\Omega t} + \Upsilon\, e^{j\Omega t}.$$

As in the axi-symmetric case, the perturbation pressure and velocity fields will be assumed to have the following form:

$$\hat{u}(r, \theta, z, t) = \tilde{u}(r)\, e^{(\alpha z + j\mu\theta + j\Omega t)}$$
$$\hat{v}(r, \theta, z, t) = \tilde{v}(r)\, e^{(\alpha z + j\mu\theta + j\Omega t)}$$
$$\hat{w}(r, \theta, z, t) = \tilde{w}(r)\, e^{(\alpha z + j\mu\theta + j\Omega t)}$$
$$\hat{p}(r, \theta, z, t) = \tilde{p}(r)\, e^{(\alpha z + j\mu\theta + j\Omega t)} \qquad \text{(E.6.2)}$$

Under this assumption, Eqs. (E.6.1) reduce to

$$\frac{1}{r}\frac{d}{dr}(r\tilde{u}) + j\mu\tilde{v} + \alpha\tilde{w} = 0$$

$$\Gamma(r)\tilde{u} - \frac{2\mathcal{V}(r)}{r}\tilde{v} + \frac{d\tilde{p}}{dr} = 0$$

$$\frac{1}{r}\frac{d}{dr}[r\mathcal{V}(r)]\tilde{u} + \Gamma(r)\tilde{v} + \frac{j\mu}{r}\tilde{p} = 0$$

$$\frac{d\mathcal{W}(r)}{dr}\tilde{u} + \Gamma(r)\tilde{w} + \alpha\tilde{p} = 0 \quad . \tag{E.6.3}$$

where

$$\Gamma(r) = j\Omega + j\mu\frac{\mathcal{V}(r)}{r} + \alpha[1 + \mathcal{W}(r)] \quad .$$

This set of four equations can be reduced to the following second order ordinary differential equation for the radial distribution of the radial velocity.

$$\left[\frac{r^2\Gamma(r)}{\alpha^2r^2-\mu^2}\right]\frac{d^2\tilde{u}(r)}{dr^2} + \left[\frac{2j\mu\mathcal{V}(r)}{\alpha^2r^2-\mu} + \frac{r^2}{\alpha^2r^2-\mu^2}\frac{d\Gamma(r)}{dr}\right.$$

$$-\left(\frac{\alpha^2r^2+\mu^2}{(\alpha^2r^2-\mu^2)^2}\right)r\Gamma(r) + \frac{2r\Gamma(r)}{\alpha^2r^2-\mu^2} - \frac{j\mu}{\alpha^2r^2-\mu^2}\frac{d}{dr}[r\mathcal{V}(r)]$$

$$\left. - \frac{\alpha r^2}{\alpha^2r^2-\mu^2}\frac{d\mathcal{W}(r)}{dr}\right]\frac{d\tilde{u}(r)}{dr} + \left[\Gamma(r) + \frac{j\mu}{\alpha^2r^2-\mu^2}\frac{2\mathcal{V}(r)}{r}\right.$$

$$+ \left(\frac{2\alpha^2}{\alpha^2r^2-\mu^2}\right)\frac{\mathcal{V}(r)}{\Gamma(r)}\frac{d}{dr}[r\mathcal{V}(r)] - \left(\frac{2j\mu\alpha}{\alpha^2r^2-\mu^2}\right)\frac{\mathcal{V}(r)}{\Gamma(r)}\frac{d\mathcal{W}(r)}{dr}$$

$$+ \frac{r}{\alpha^2r^2-\mu}\frac{d\Gamma(r)}{dr} - \frac{\alpha^2r^2+\mu^2}{(\alpha^2r^2-\mu^2)^2}\Gamma(r) + \frac{2j\mu\alpha^2r}{(\alpha^2r^2-\mu^2)^2}\frac{d}{dr}[r\mathcal{V}(r)]$$

$$- \frac{j\mu}{\alpha^2r^2-\mu^2}\frac{d^2}{dr^2}[r\mathcal{V}(r)] - \frac{\alpha^2r^2}{\alpha^2r^2-\mu^2}\frac{d^2\mathcal{W}(r)}{dr^2}$$

$$\left. + \frac{2\mu^2\alpha r}{(\alpha^2r^2-\mu^2)^2}\frac{d\mathcal{W}(r)}{dr}\right]\tilde{u}(r) = 0 \tag{E.6.4}$$

The radial velocity is again subject to the boundary conditions specified in Eq. (E.2.3). The radial distributions of the other perturbation quantities are calculated from $\tilde{u}(r)$.

The radial distribution of the mean swirl and axial velocities will be prescribed according to Eq. (E.2.7). As before, a solution for $\tilde{u}(r)$ can be obtained in terms of the power series given in Eq.(E.2.8). Clearly, the coefficients β_i vanish for all $i \leq 1$.

In the case of a quadratic swirl velocity ($V(r) = Nr^2$) and a uniform axial velocity ($W(r) = 0$), the m^{th} term in the power series expansion for $\tilde{u}(r)$ is

$$\beta_m = \frac{-1}{\mu^2\hat{\Gamma}^2[\mu^2-(m+1)^2]} \left\{ j\mu^3\hat{\Gamma}N\left[2\mu^2 + 1 - 2(m-1)(m+1)\right]\beta_{m-1} \right.$$

$$+ \left[\mu^4N^2(m(m-2)-2-\mu^2) + \alpha^2\hat{\Gamma}^2\left((m-2)^2-1-2\mu^2\right)\right]\beta_{m-2}$$

$$+ j\alpha^2\mu\hat{\Gamma}N\left[1+2(m-3)^2-4\mu^2\right]\beta_{m-3}$$

$$+ \left[\alpha^4\hat{\Gamma}^2 + \alpha^2\mu^2N^2(2\mu^2-8-(m-4)^2)\right]\beta_{m-4}$$

$$\left. + 2j\alpha^4\mu\hat{\Gamma}N\beta_{m-5} + \alpha^4N^2(6-\mu^2)\beta_{m-6} \right\} \qquad \text{(E.6.5)}$$

where

$$\hat{\Gamma} = \alpha + j\Omega .$$

When the boundary conditions are applied, it transpires that

$$\beta_m = 0 \text{ ; for all } m < \mu-1 \qquad \text{(E.6.6)}$$

For $m \geq \mu - 1$, the coefficients are calculated by means of Eq. (E.6.5) relative to $\beta_{\mu-1}$. In addition, the above recursion relation reduces to the following expression for large values of m.

$$\beta_m = -\left(\frac{2j\mu N}{\alpha+j\Omega}\right)\beta_{m-1} + \left[\frac{\mu^2N^2}{(\alpha+j\Omega)^2} + \frac{\alpha^2}{\mu^2}\right]\beta_{m-2}$$

$$- \frac{2j\alpha^2N}{\mu(\alpha+j\Omega)}\beta_{m-3} + \frac{\alpha^2N^2}{(\alpha+j\Omega)^2}\beta_{m-4} \qquad \text{(E.6.7)}$$

In order for the power series to converge, the modulus of all the above ratios must be strictly less than one. Consequently, the following two inequalities must hold for the series to converge.

$$\left|\frac{\alpha}{\mu}\right| < 1 \qquad \text{(E.6.8)}$$

and

$$\left|\frac{2\mu N}{\alpha+i\Omega}\right| < 1 \qquad \text{(E.6.9)}$$

The second of these two inequalities, Eq. (E.6.9), can be put into the following form:

$$2N < \frac{|\alpha|}{\mu}\left(1 + \frac{\Omega}{|\alpha|}\right) < 1 \quad . \qquad \text{(E.6.10)}$$

The magnitude of the swirl velocity is linearly related to the frequency of the perturbations. At low frequencies, a power series solution for $\tilde{u}(r)$ exists only for very small swirl velocities. Larger swirl velocities are associated with higher frequency waves. An eigenvalue search has not yet been performed. However, if the eigenvalues, α, follow the same general behavior as those of the axi-symmetric perturbations, (i.e. see Fig. E.5), then the non-axi-symmetric perturbations corresponding to auto-oscillation frequencies will be attenuated as they propagate upstream. If the assumed similarity between the axi-symmetric and non-axi-symmetric eigenvalues is correct, then the alphas will be composed of a large positive real part and a small

positive imaginary component. Thus, the first convergence criterion Eq. (E.6.8), merely puts a bound upon the rate of attenuation of the perturbations; it is proportional to the azimuthal wave number, μ. It appears that the waves with a greater periodicity in the azimuthal direction are attenuated at a greater rate. If the assumed similarity is not valid and the alphas are purely imaginary, then Eq. (E.6.8) requires that the axial wave length of the perturbations be larger than the azimuthal wave length, i.e.

$$\frac{2\pi R}{\mu} < \lambda^* \qquad \text{(E.6.11)}$$

where

λ^* = dimensional wavelength of the perturbations in the axial direction (Imag $\{\alpha\} = 2\pi/\lambda$).

The non-axi-symmetric perturbation analysis was not carried any further. This section was included in order to indicate the feasibility of such calculations.

TABLE E.1

$V(r) = Nr^n$	$w(r) = Kr^k$	
n	K	k
1	0.0	—
2	0.0	—
3	0.0	—
3	-0.40	2
3	0.40	2

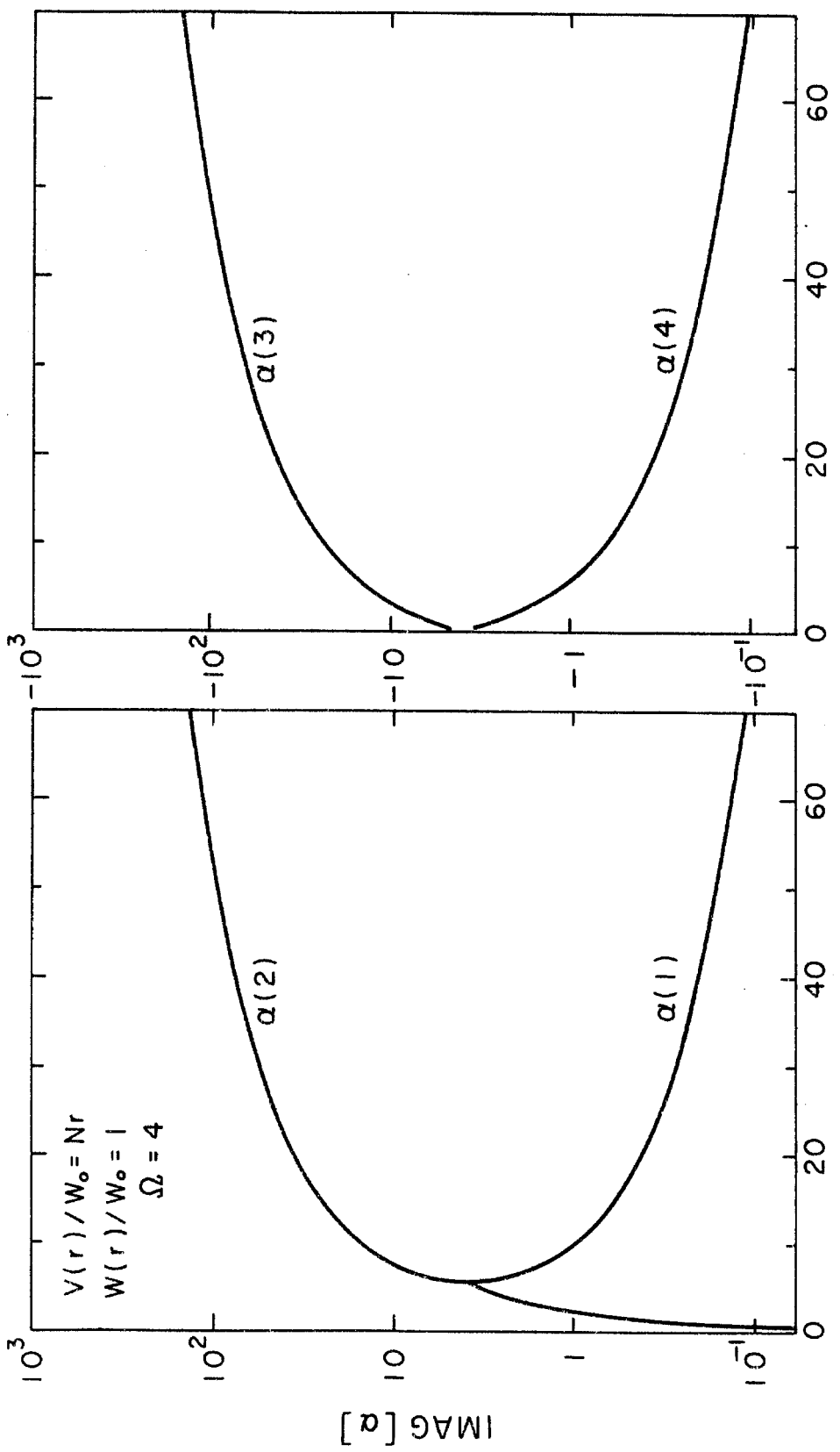

Fig. E. 1a Imaginary part of eigenvalues, α, associated with uniform axial velocity and rigid body rotation for the given non-dimensional frequency of 4.

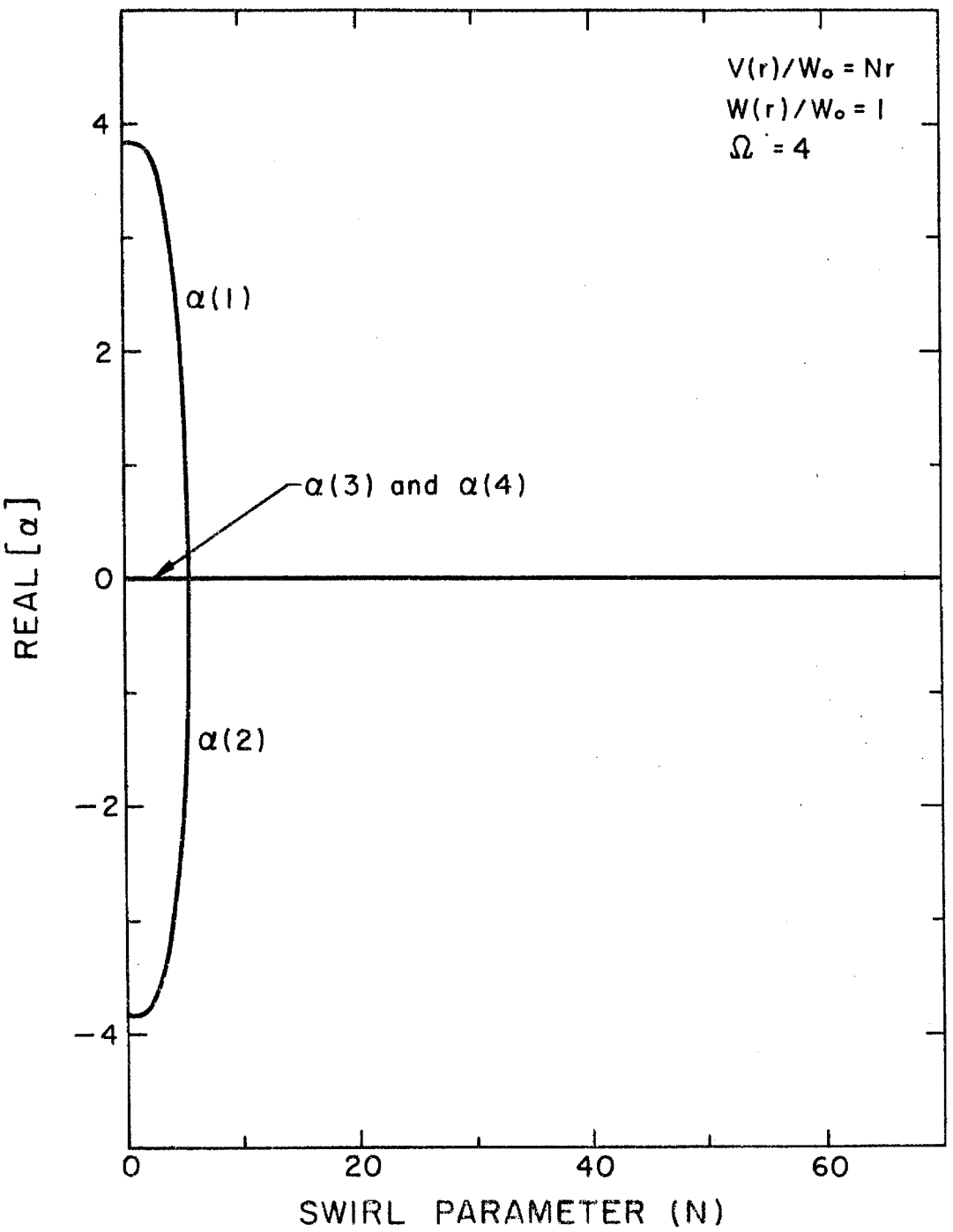

Fig. E. 1b Real part of eigenvalues, α, associated with uniform axial velocity and rigid body rotation for the given non-dimensional frequency of 4.

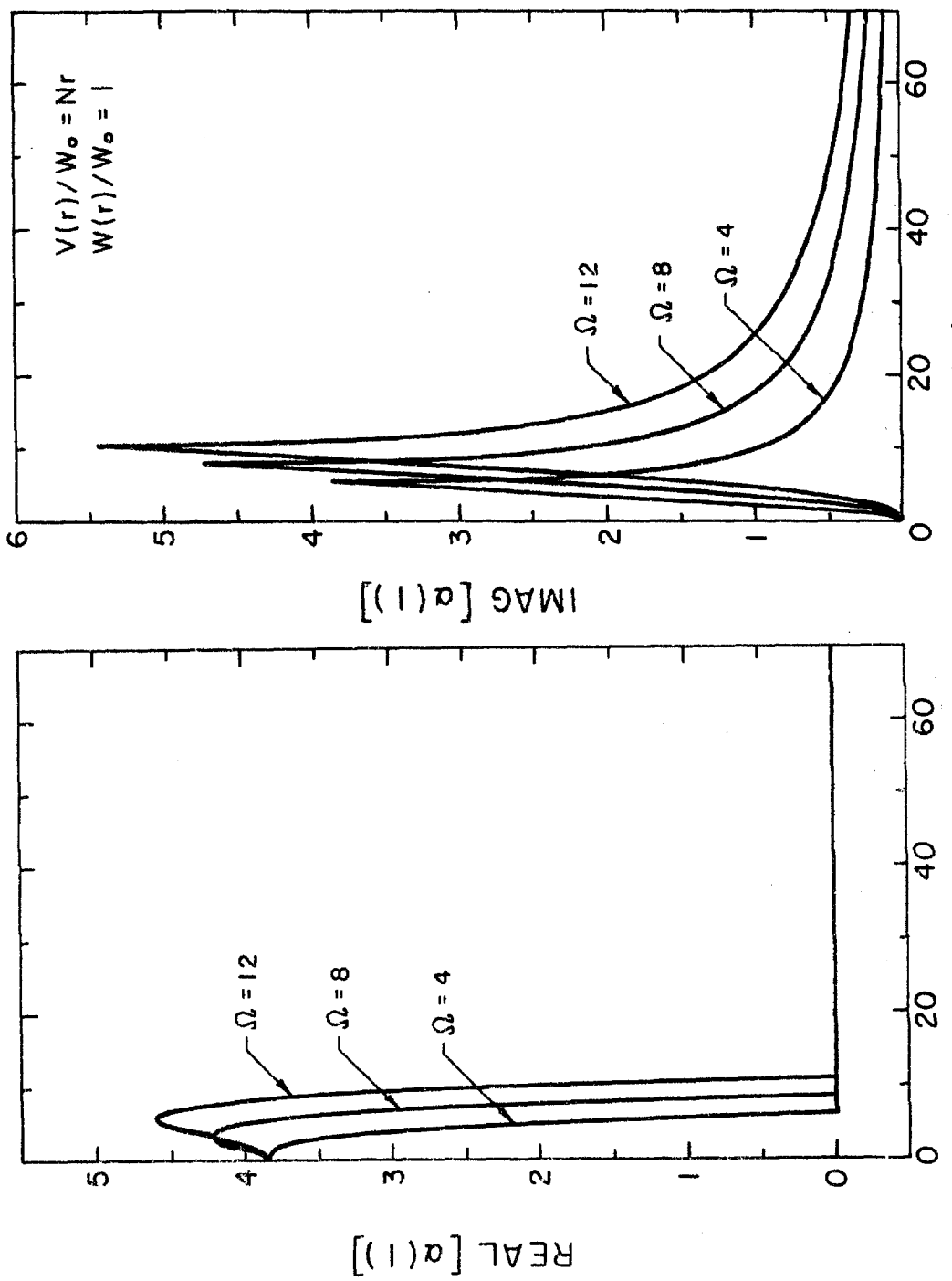

Fig. E.2 Frequency variation of the real and imaginary parts of the eigenvalue, $\alpha(1)$, associated with uniform axial velocity and rigid body rotation plotted against the strength of the swirl velocity.

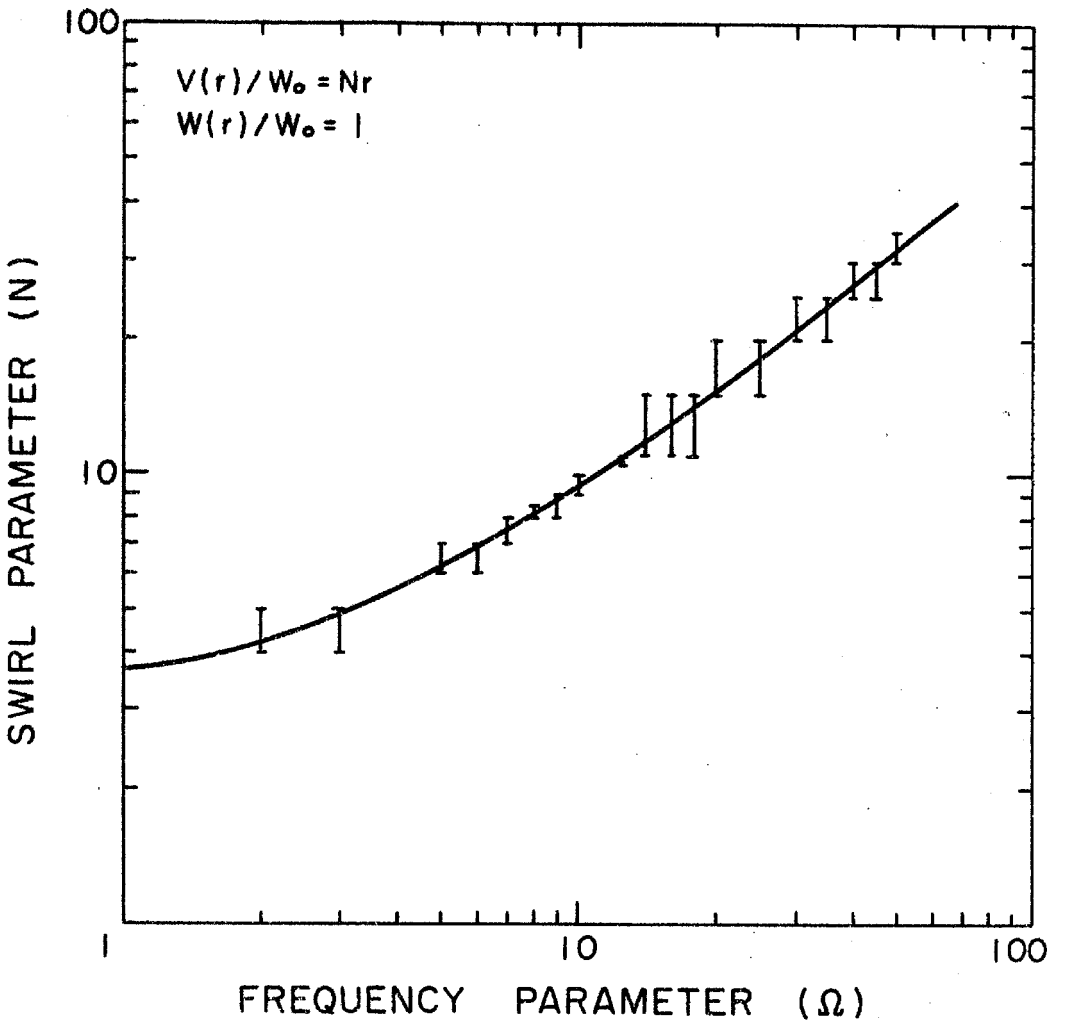

Fig. E.3 Critical value of the swirl intensity plotted as a function of frequency for the mean flow of uniform axial velocity and rigid body rotation.

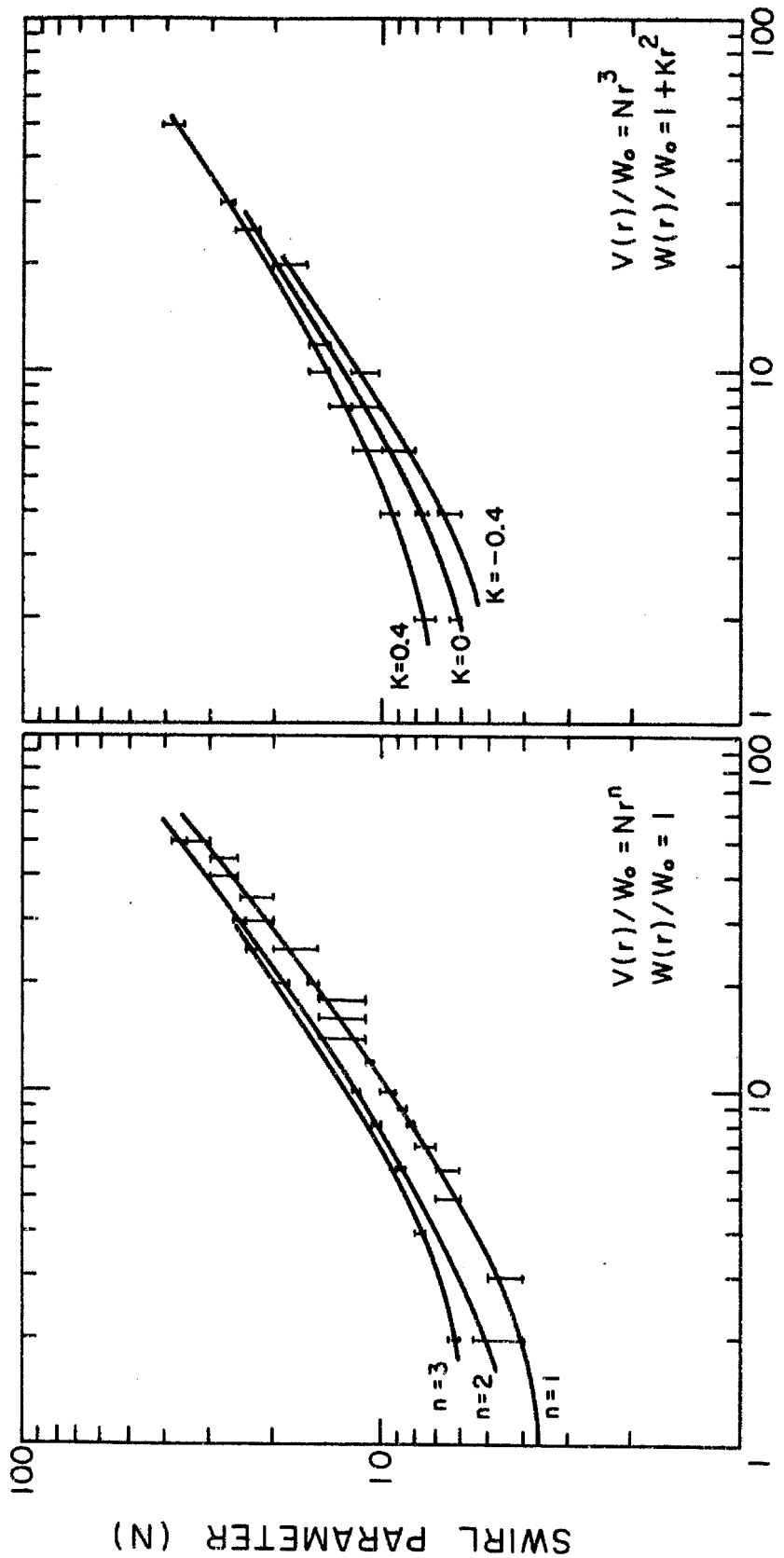

Fig. E.4 Critical value of swirl intensity plotted against frequency for: (a) different curvatures in the swirl velocity profile and (b) non-uniformity in the axial velocity profile.

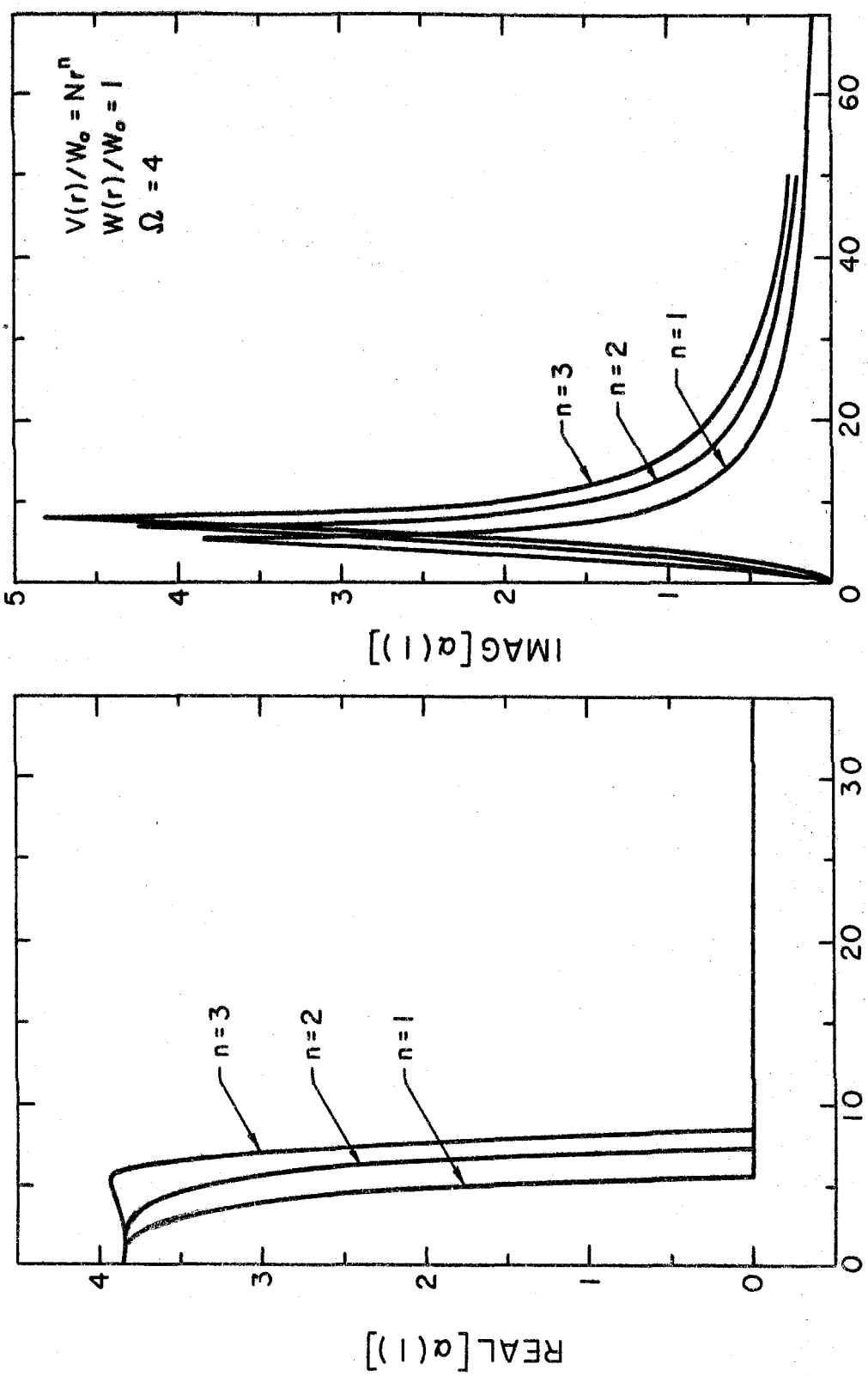

Fig. E.5 Real and imaginary parts of eigenvalue, $\alpha(1)$, associated with a uniform axial velocity and different curvatures (i.e. n) of the swirl velocity profile plotted against the strength of the swirl velocity for a frequency of 4.

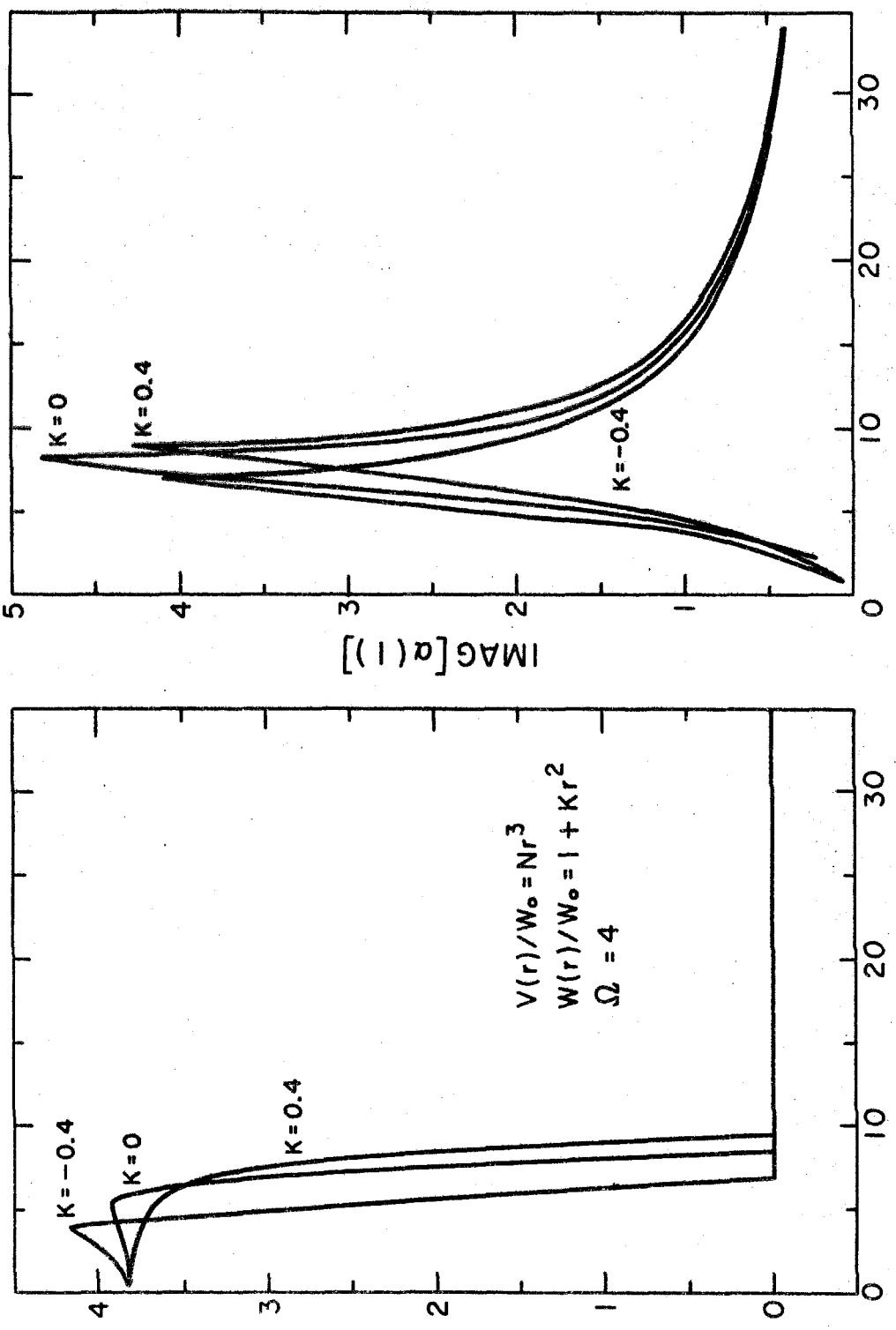

Fig. E.6 Real and imaginary parts of eignvalue, $\alpha(1)$, associated with a cubic swirl velocity profile and different axial velocity profiles plotted against the strength of the swirl velocity for a frequency of 4.

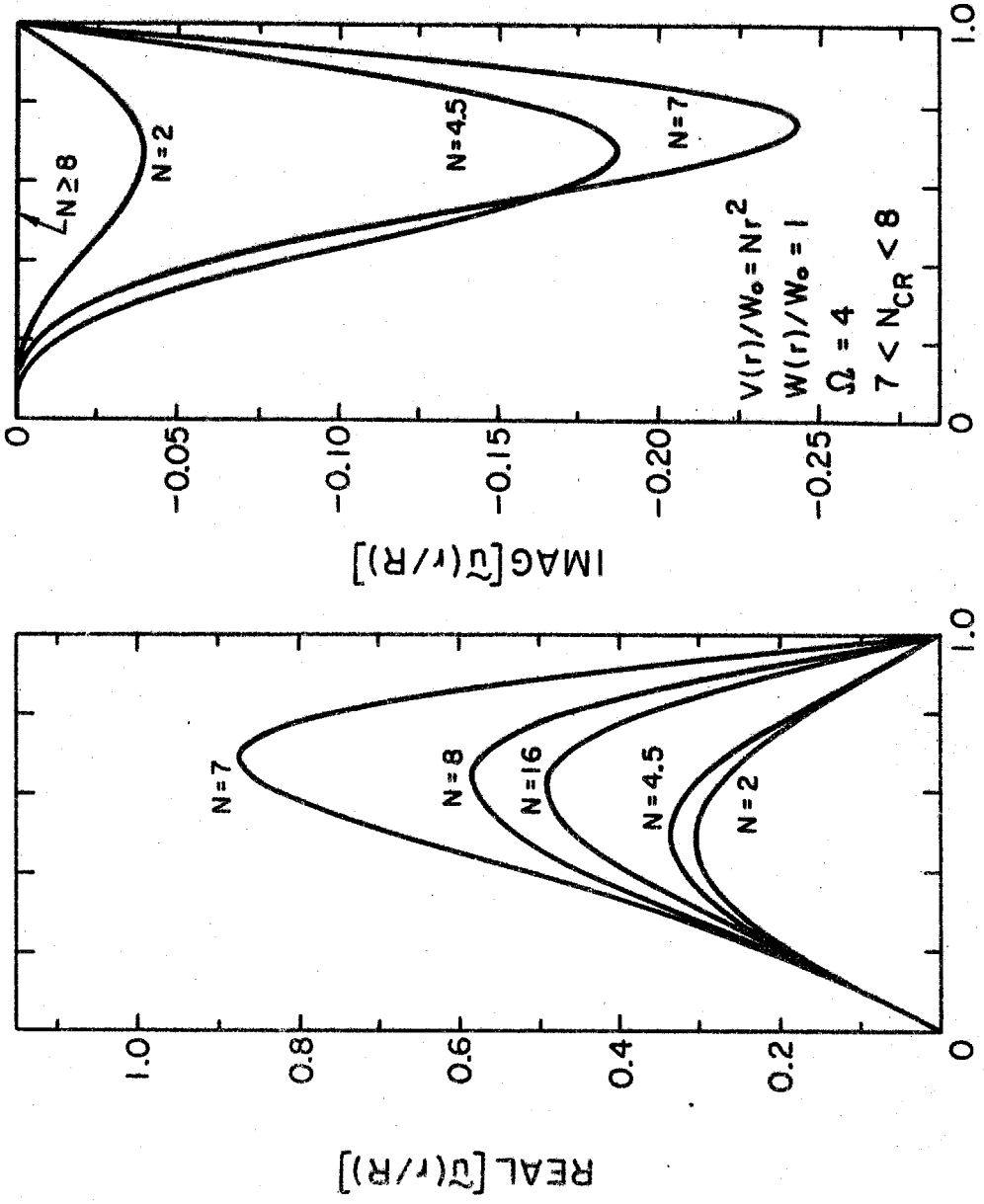

Fig. E.7 Radial distribution of both the real and imaginary parts of the perturbation radial velocity associated with a uniform axial velocity and a quadratic swirl velocity plotted for several swirl velocity amplitudes.

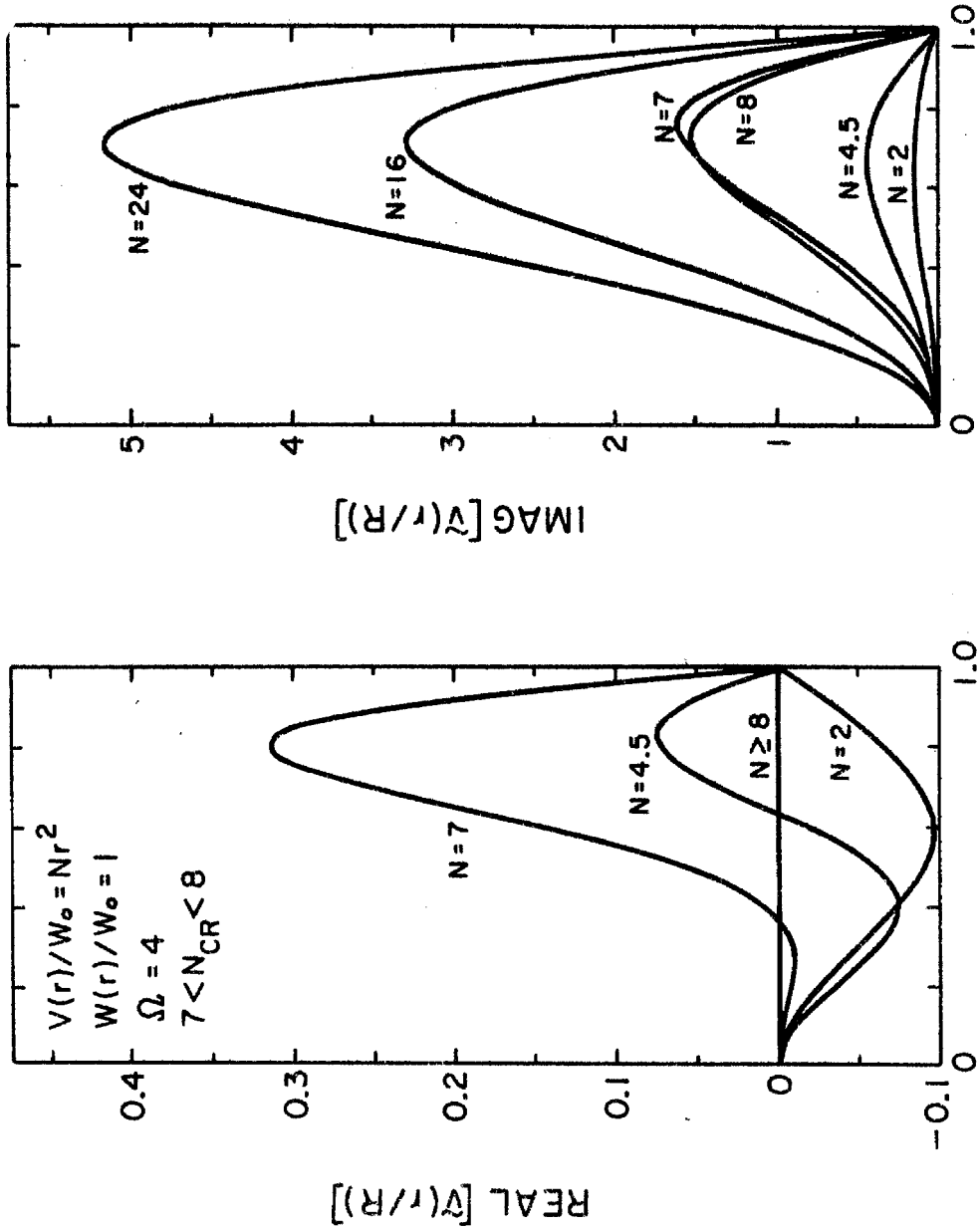

Fig. E.8 Radial distribution of both the real and imaginary parts of the perturbation swirl velocity associated with a uniform axial velocity, a quadratic swirl velocity and a frequency of 4 plotted for several amplitudes of the mean swirl velocity.

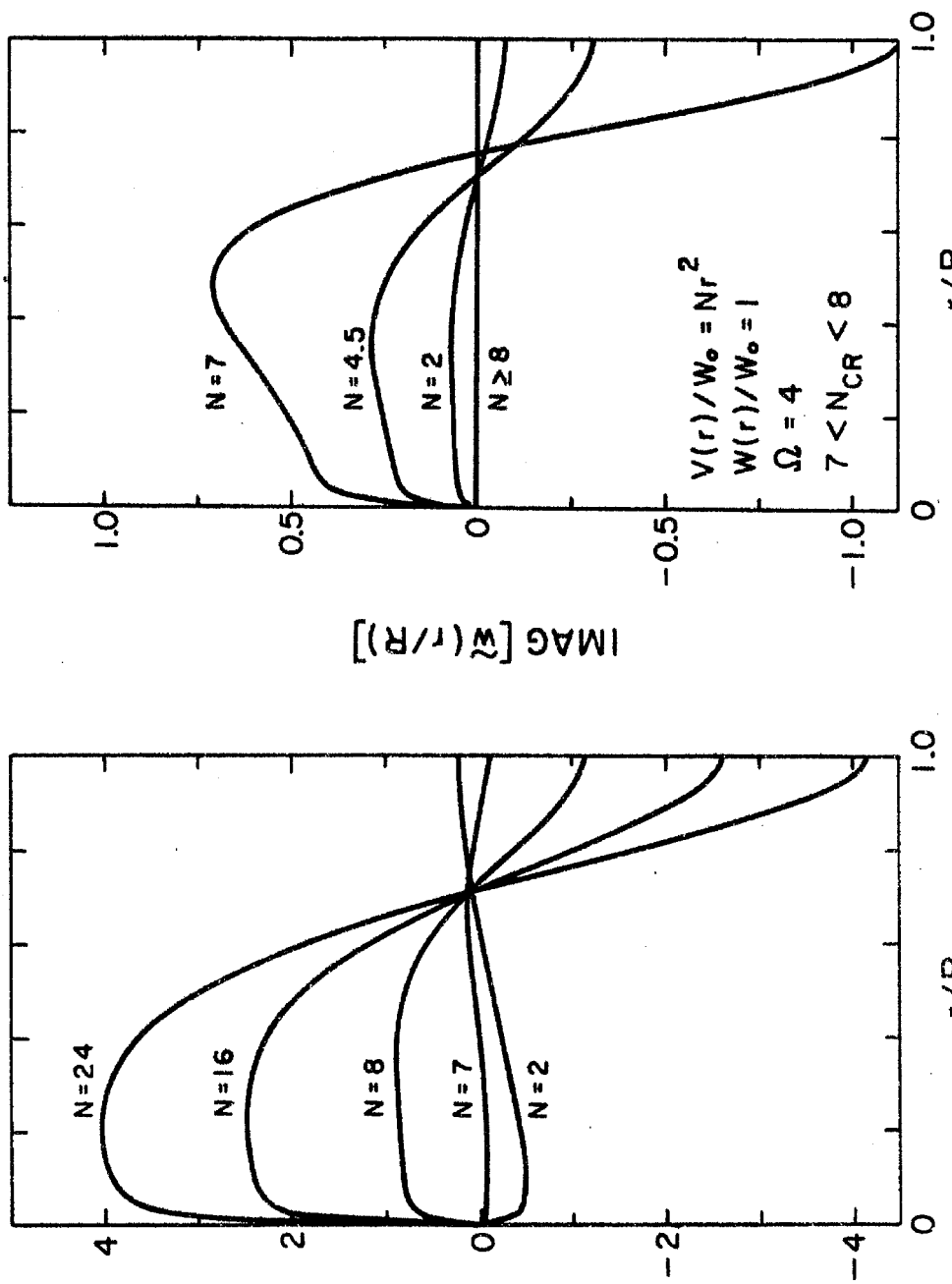

Fig. E.9 Radial distribution of both the real and imaginary parts of the perturbation axial velocity associated with a uniform axial velocity, a quadratic swirl velocity and a frequency of 4 plotted for several amplitudes of the mean swirl velocity.

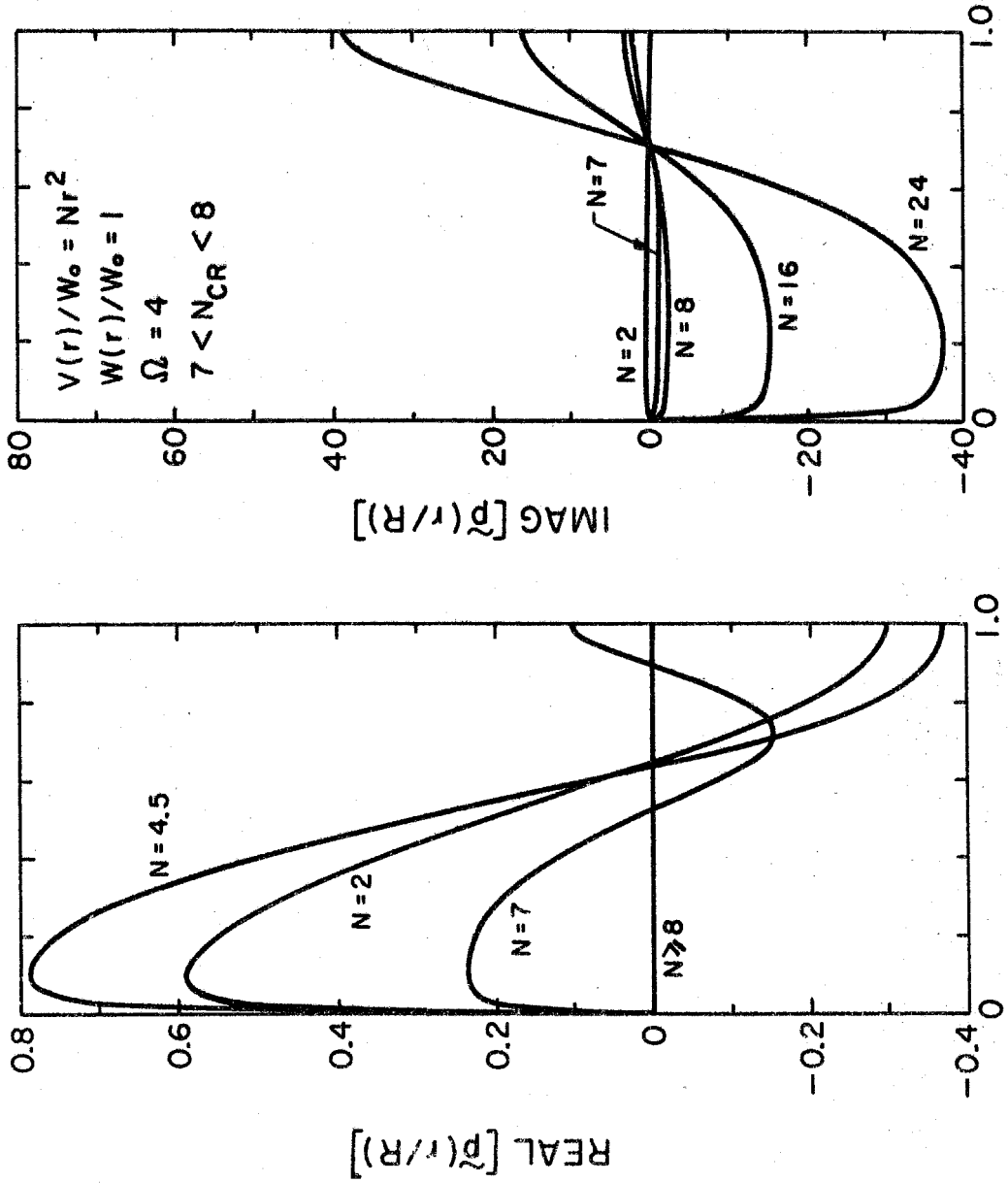

Fig. E. 10 Radial distribution of both the real and imaginary parts of the perturbation pressure field associated with a uniform axial velocity, a quadratic swirl velocity and a frequency of 4 plotted for several amplitudes of the mean swirl velocity.

APPENDIX F

TRANSFER FUNCTION MODEL

The idea upon which this model is based is the observation that the activity of the inducer depends upon the cavitation present within the inducer. It has been observed that the cavitation occurs primarily in the tip clearance or backflow ahead of the inducer. It seems reasonable to assume that most of the pump dynamics included in the transfer function occur in the inlet flow field. This contention is further supported by the correspondence between the inlet pressure fluctuations and the downstream pressure fluctuations. The above approximation neglects the inertance associated with the inducer. The transfer function, [Y], of the inducer cannot be used immediately. The dynamics of the downstream section of the system, which consists of a diffuser, the downstream smoothing chamber and a nozzle, must be removed from the transfer function. A lumped parameter model consisting of a resistance, $\Re$, inertance, $\mathscr{L}$, and compliance, C, was used to describe the dynamics of these components. This model is illustrated in Fig. F.1. The reduced transfer function of the inducer, [X], is defined by the following relation.

$$\begin{bmatrix} Y_{11} & Y_{12} \\ Y_{21} & Y_{22} \end{bmatrix} = \begin{bmatrix} 1 & -(\Re + j\Omega\mathscr{L}) \\ -j\Omega C & 1+j\Omega C(\Re + j\Omega\mathscr{L}) \end{bmatrix} \begin{bmatrix} X_{11} & X_{12} \\ X_{21} & X_{22} \end{bmatrix} \qquad (F.1)$$

In terms of the far upstream fluctuating pressure and mass flow rate measurements, $\tilde{p}_\infty$ and $\tilde{m}_\infty$, the pressure fluctuations at the inlet of the inducer, $\tilde{p}_1$, are given by

$$\tilde{p}_1 = X_{11}\tilde{p}_\infty + X_{12}\tilde{m}_\infty \qquad (F.2)$$

where

$$X_{11} = [1+j\Omega C(\mathcal{R}+j\Omega\mathcal{L})]\, Y_{11} + (\mathcal{R}+j\Omega\mathcal{L})\, Y_{21}$$

$$X_{12} = [1+j\Omega C(\mathcal{R}+j\Omega\mathcal{L})]\, Y_{12} + (\mathcal{R}+j\Omega\mathcal{L})\, Y_{22} \quad .$$

Alternately, the measurements of the inlet pressure fluctuations can be used to generate the two elements, X_{11} and X_{12}, of the reduced transfer function. Unfortunately, both X_{11} and X_{12} cannot be obtained simultaneously since two linearly independent sets of velocity and pressure measurements are needed. It is necessary to assume the value of either X_{11} or X_{12} in order to determine the other quantity.

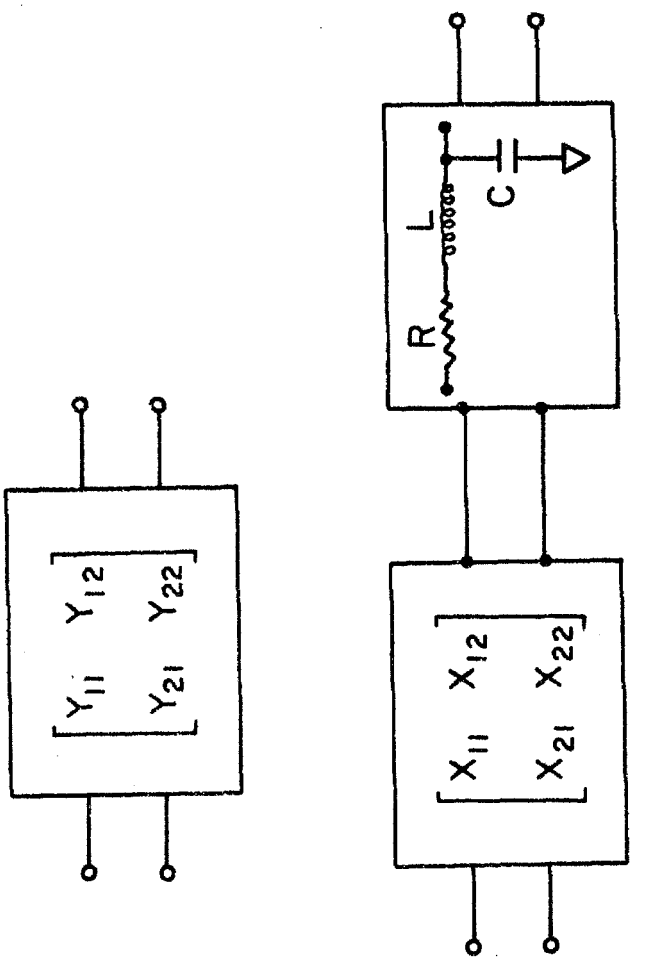

Fig. F.1 Schematic of the transfer function model.

APPENDIX G
JUSTIFICATION OF LARGE COMPLIANCE ASSUMPTION

A direct verification concerning the relative magnitude of the air bladder compliance with regard to Eq. (4.3.7) was provided by a specially designed experiment. An operating condition for which IMP7 exhibited an auto-oscillation was selected. This steady state operating condition – $\varphi = 0.055$ and $\sigma = 0.019$ – was then maintained while the volume of the air bladder, and hence its compliance, were varied. The results of this experiment are presented in Figs. G.1 and G.2. The frequency of the auto-oscillation remained essentially constant as the air bladder volume was increased from a small fraction of a liter to 37.5 liters of air. Similarly, the amplitudes of the pressure and mass flow rate fluctuations both upstream and downstream of the pump remained constant. Therefore, large changes in the air bladder compliance do not appear to affect the stability of the hydraulic system. This suggests that the compliance of the air bladder is indeed large. Hence, if the proposed model of the DPTF is accepted, then the stability criterion expressed in Eq. (4.3.9) is the appropriate criterion.

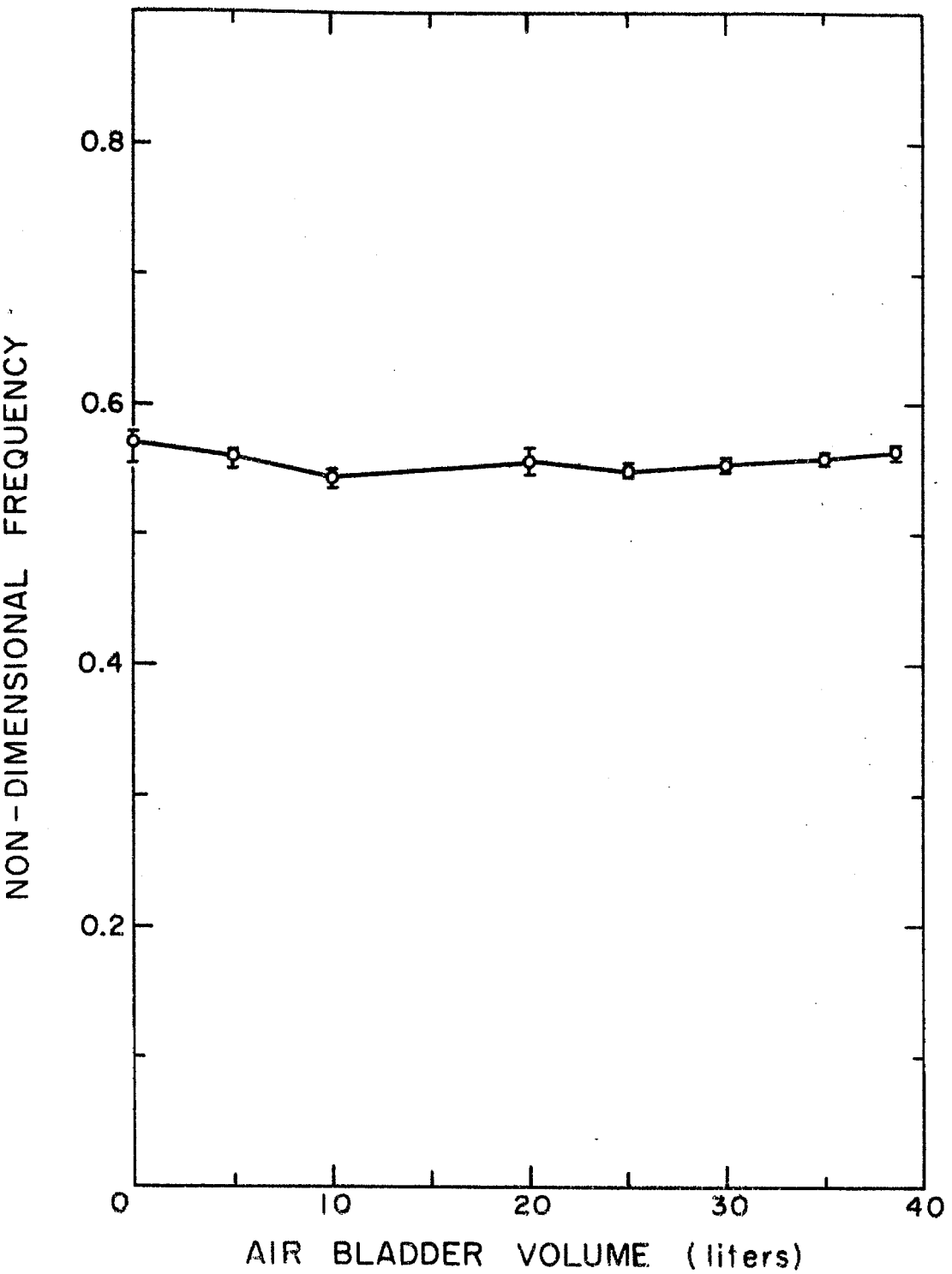

Fig. G.1 Variation of the frequency of auto-oscillation with bladder compliance.

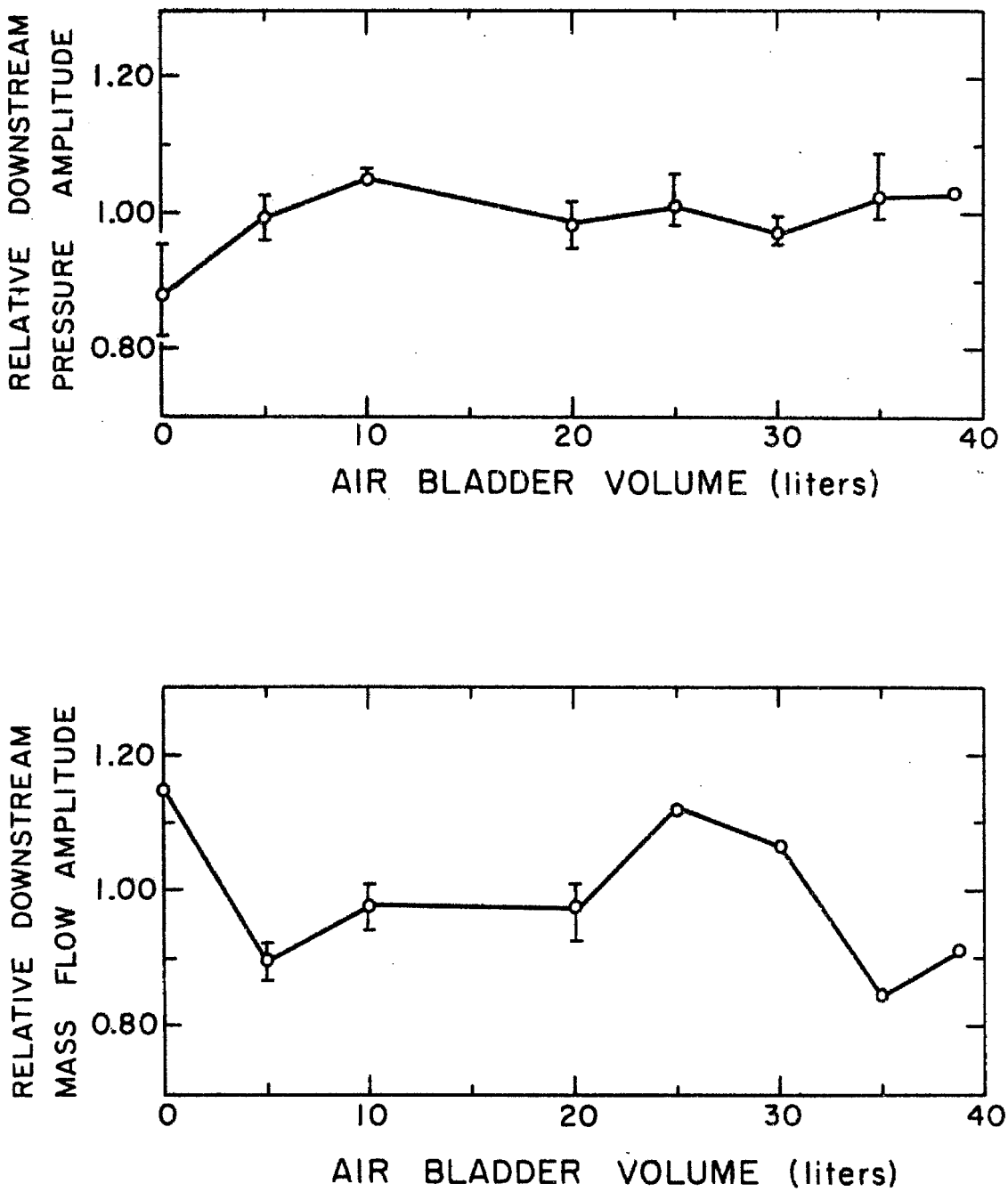

Fig. G.2 Variation of the amplitudes of the downstream pressure and mass flow rate fluctuations during auto-oscillation with air bladder compliance.